INFORMATION TO USERS

This manuscript has been reproduced from the microfilm master. UMI films the text directly from the original or copy submitted. Thus, some thesis and dissertation copies are in typewriter face, while others may be from any type of computer printer.

The quality of this reproduction is dependent upon the quality of the copy submitted. Broken or indistinct print, colored or poor quality illustrations and photographs, print bleedthrough, substandard margins, and improper alignment can adversely affect reproduction.

In the unlikely event that the author did not send UMI a complete manuscript and there are missing pages, these will be noted. Also, if unauthorized copyright material had to be removed, a note will indicate the deletion.

Oversize materials (e.g., maps, drawings, charts) are reproduced by sectioning the original, beginning at the upper left-hand corner and continuing from left to right in equal sections with small overlaps. Each original is also photographed in one exposure and is included in reduced form at the back of the book.

Photographs included in the original manuscript have been reproduced xerographically in this copy. Higher quality 6" x 9" black and white photographic prints are available for any photographs or illustrations appearing in this copy for an additional charge. Contact UMI directly to order.

UMI

A Bell & Howell Information Company
300 North Zeeb Road, Ann Arbor MI 48106-1346 USA
313/761-4700 800/521-0600

Modulation Potential Effects on the Quantum Magnetotransport in a Two-Dimensional Electron Gas

by

Tae-ik Park

A dissertation submitted to the Graduate Faculty in Physics in partial fulfillment of the requirements for the degree of Doctor of Philosophy, The City University of New York

1998

This manuscript has been read and accepted for the Graduate Faculty in Physics in satisfaction requirement for the degree of Doctor of Philosophy.

August 29 '97
Date

Professor Godfrey Gumbs
Chair of Examinig Committe

9/9/97
Date

Professor Louis S. Celenza
Executive Officer

Professor Ying-Chih Chen

Professor H. L. Cui

Professor Marten DenBoer

Supervisory Committee

THE CITY UNIVERSITY OF NEW YORK

Abstract

Modulation Potenial Effects

on the Quantum Magnetotransport

in a Two-Dimensional Electron Gas

by

Tae-ik Park

Advisor : Godfery Gumbs

The quantum magnetotransport (QMT) coefficients of a two-dimensional electron gas (2DEG) in a perpendicular magnetic field for the 2D square array of modulated anti-dot(AD) and quantum dot (QD)-limit potentials and 1D Quantum Wire (QW) are calculated in the low magnetic field region (< 0.3 T) using the Kubo method. The model potential is modulated by controlling the steepness and its strength. The effect on the band part of all QMT coefficients are studied. Our analysis is based on how the sub Landau Level states due to new magnetic Brillouin zone (MBZ) affect the QMT coefficients, how the cyclotron orbit and the scattering by the potential contribute to the QMT coefficients, and how the states near the Fermi level and below the Fermi level contribute to the QMT coefficients when the size and the strength of the modulated potential are changed.

The results for 2D modulation show that

(i) Oscillations associated with the filling of sub Landau levels occur in $\sigma_{xx}^{(0)}$ and $\sigma_{yx}^{(0)}$ for the low modulation case.

(ii) The effect of scattering by the AD potential is quite different from that by the dot potential

(iii) For a strong lateral superlattice AD potential, the longitudinal resistivity $\rho_{xx}^{(0)}$ has a double peak structure which depends on both the strength of the modulation potential as well as its slope.

(iv) For both the AD and QD potentials, $\rho_{xy}^{(0)}$ is quenched and is negative at low magnetic fields which depend on the size and the strength of the modulation.

(v) For the strong dot potential, there are Aharanov-Bohm oscillations in $\rho_{xx}^{(0)}$ and $\rho_{xy}^{(0)}$ and large plus-to-minus oscillations.

The double peak structure in $\rho_{xx}^{(0)}$ and the negative values and quenching of the Hall effect at low magnetic fields have been observed experimentally for AD in both the quasiclassical and quantum regimes.

In 1D modulation, all the QMT coefficients of a 2DEG in a perpendicular magnetic field for the Short Quantum Wire are calculated in the low magnetic field region (< 0.3 T) using the Kubo method. The Quantum Wire Channal is

modulated by controlling the steepness and its strength of the potential barrier. Our studies show a step-like feature in transverse conductivities due to the Landau Level (LL) crossing for the weak modulation and low-field giant peaks in the transverse resistivities for the strong potential. And also, quenched Hall resistivities at low magnetic fields are presented. In longitudinal resistivites, some threshold peaks are shown. Our interesting feature is the negative Hall resistivities which are guessed as the result of the boundary back-scattering in the short Quantum Wire.

Dedication

To my family

Acknowledgement

First of all. I would like to say "Thank you" to my Ph.D. thesis advisor .Professor Godfrey Gumbs from my deep heart. Without his endurance. consideration and kind guidence. this thesis could not be finished. Sometimes it was very difficut to progress my thesis. However. he always endured and kindly guided me and covered my faulty with his forgiveness. Nobody couldn't do this but him. I think. He helped me understand physics with his profound physical insight and he has always encouraged me with his creative intuition in progressing the thesis.

I greatly thank all the other members of my thesis advisory. Professor Ying-chih Chen of Hunter College. Professor H. L. Cui of Stevens Institue of Technology. and Professor Marten DenBoer of Hunter College for agreeing to serve my committee and for serving as examiners from 2nd exam to the defence. They gave me the considerate and valuable advice and guidance. With their help. I could wrtie this thesis.

And. I appreciate the consideration and support of all other professors in physics department at Hunter College. They kindly guided and gave me the opprotunity to work as adjunt faculty in physics department until thesis is finished. Also. I appreciate the kindness of all the staffs and colleagues in physics department.

Another appreciation is the support of Korean Government and Cheonbuk

National University(CNU). The CNU President and. all professors in physics department at CNU. especially professor Keebang Lee who was my M.S. thesis advisor and professor Hyungjae Lee who guided my major.They recommanded me to the Korean Government to take the exam for oversea study so that I could get 40.000 dollars for the beginning 3 years.

Finally. I would like to thank my family (my parents. my wife's family. my wife. and two sons) and all pastors of the churches that I attended: They prayed and entirely supported me from the beginning to the end so that I finish this thesis. Especially I appreciate my wife's effort. She endured and faced many difficulties to support me. I remember. at this point. my father who was dead 6 years ago. If my father were alive. then I would be more happy because I could show this thesis to him.

Contents

Abbreviations

1D	1 Dimension or 1 Dimensional
2D	2 Dimension or 2 Dimensional
2DEG	2 Dimensional Electron Gas
AD	Anti-dot
AW	Anti Wire
LL	Landau Level
MBE	Molecular Beam Epitaxy
MBZ	Magnetic Brillouin Zone
MOCVD	Metal-organic Chemical Vapor Deposition
MUC	Magnetic Unit Cell
QD	Quantum-dot
QMT	Quantum Magnetotransport
QW	Quantum Wire
SdH	Shuvnikov de Hass
TBA	Tight Binding Approximation

Physical Constants

c	Speed of light	$3.0 \times 10^8 m^2/sec$
e	Electron charge	$1.602 \times 10^{-19} C$
h	Planck constant	$6.626 \times 10^{-34} joule - sec$
$\hbar$	$h/2\pi$	$1.054 \times 10^{-34} joule - sec$
m_0	Electron rest mass	$9.109 \times 10^{-31} kg$
m^*	Effective electron mass	$0.067 m_0$ for GaAs/AlGaAs

QMT Coefficient Notations (MKS Units)

2D Case

$\sigma_{xx}^{(0)}$	Longitudinal Conductivities	in the unit of e^2/h
$\sigma_{yx}^{(0)}$	Hall Conductivities	in the unit of e^2/h
$\rho_{xx}^{(0)}$	Longitudinal Resistivities	in the unit of h/e^2
$\rho_{xy}^{(0)}$	Hall Resistivities	in the unit of h/e^2

1D Case

$\sigma_{xx}^{(0)}$	Transverse Conductivities	in the unit of e^2/h
$\sigma_{yx}^{(0)}$	Hall Conductivities	in the unit of e^2/h
$\sigma_{yy}^{(0)}$	Longitudinal conductivities	in the unit of e^2/h
$\rho_{xx}^{(0)}$	Transverse Resistivities	in the unit of h/e^2
$\rho_{xy}^{(0)}$	Hall Resistivities	in the unit of h/e^2
$\rho_{yy}^{(0)}$	Longitudinal Resistivities	in the unit of h/e^2

Here, the superscript (0) of QMT coefficient is used for the band part.

Notations and values used in this thesis

a	Lattice constant of modulation	$200nm$
A	Area of the sample	
B	Magnetic field intensity	$< 0.3T$ (cf Table 1)
G	Reciprocal lattice vector	$2\pi/a$
H_1	Height of the QW	
$H_n(x)$	nth order Hermite polynomial	
l	Mean free path	
l_H	Magnetic length	$\sqrt{\hbar/eB}$
L	Integers	$-N_y/2, \ldots, ((N_y/2)-1)$
L_1	Length of the QW	
m	Substates index by umklapp scattering	$0, \pm1, \pm2, \ldots$
n	Landau level index	$0, 1, 2, \ldots$
n_{2D}	Density of states in 2D	$1.25 \times 10^{13}/m^2$
N	Power of modulation	$1, 2, \ldots$
N_x	Number of unit cells in x direction	4, 6, 8, or 10
N_y	Number of unit cells in y direction	4, 6, 8, or 10
r_c	Cyclotron radius ($\sqrt{(n+1)(\hbar/eB)}$)	cf. Table 1
U_0	$m^*\overline{V}_0 a^2/(2^{1/2}\pi\hbar^2)$	$\pm1.235, \pm2, \pm3, \pm4, \pm10, \pm100$
u_x	Grid potential parameter in x direction	1 is used
u_y	Grid potential parameter in y direction	1 is used
V_0	Intensity of modulation	$0.156 \sim 12.7meVm^2$
$\overline{V}_0$	V_0/a^2	$0.156 \sim 12.7meV$
W_1	Width of the QW	
X_0	Guiding center of the orbit	$k_y {l_H}^2$
φ_0	Magnetic flux quantum	h/e
Φ	Ratio of magnetic flux	$Ba^2/\varphi_0 (0.3 \sim 4.0)$
ω_c	Cyclotron resonant freguence	eB/m^*

List of Figures

List of Tables

1 Introduction

Since 1970 when *Esaki* and *Tsu* proposed the fabrciation of an artificial periodic structure consisting of alternate layers of two dissimilar semiconductors with layer thickness of the order of nanometers which is called **superlattice**[1]. it has been possible to fabricate the superlattices and many other kinds of nanometer scale semiconductor structures. namely **nanostructures**. with the developement of sophisticated growth techniques such as molecular beam epitaxy (MBE) and metal- organic chemical vapor deposition (MOCVD) etc..[2] One of these nanostructures is the GaAs/$Al_xGa_{1-x}As$ heterostructure. AlGaAs is very similar in many ways to GaAs. but there is one important difference. The enegy band gap of AlGaAs is larger than that of GaAs. So. there are very abrupt discontinuities. known as **band offsets**. in their energy bands at the interface. If AlGaAs which is the material with the larger band gap is doped with shallow donors. then the Fermi level is shifted from the middle of the band gap of AlGaAs to the donor level. In order to maintain a constant Fermi level or chemical potential througout the two materials. electrons flow down from AlGaAs to GaAs. This electron transfer raises the Fermi level energy on the GaAs side due to the level filling but also raises the electrostatic potential of the AlGaAs side of the interface region because those electrons leave the numerous ionized donors in the AlGaAs side. This causes the band edges to bend at the interface between AlGaAs and GaAs, which is called **band bending**. Therefore, once the electrons have fallen

into the lower energy GaAs states they are unable to gain sufficient to move back up to the AlGaAs conduction band. The elctrons are confined in a narrow layer of the GaAs close to the interface with the AlGaAs as 2DEG. These 2DEG are physically separated from the ionized impurities in AlGaAs. hence they are freely move along a direction parallel to the interface.[4] This method is called **modulation doping** technique which was first proposed by *Störmer* et al.[3] Using this modulation doping technique. we can get a very high carrier mobility. ($10^6 cm^2/(V \cdot s)$ for GaAs).

If the magnetic field is perpendicularly applied to the plane of this homogeneus 2DEG. then electron has closed cyclotron orbit whose eigenvalues are expressed as Landau levels (LLs). Due to this LL filling. the longitudinal resistance (magnetoresistance) exhibits the Shubnikov-de Haas (SdH) oscillations and the Hall resistance exhibhits the quantum Hall effect (QHE) at quite high magnetic fields ($\omega_c \tau > 1$) and at quite low temperatures ($\hbar\omega_c > k_B T$). When observed at very high magnetic fields. at very low temperatures ($< 100mK$) and in very high-purity samples. the SdH effect and the QHE exhibit the very marked departure from the usual behaviour. smooth oscillations of the longitudinal magnetoresistance and the linear change of the Hall voltage with magnetic field. Zeros of the longitudinal resistance are observed, corresponding to the finite width for the well-defined plateaus of the Hall resistance. It has been known that this existence of a finite width for the QHE plateaus and for the zero longitudinal

resistance dips is due to the localized states. If there are no states between the successive conducting LLs. the Fermi level jumps from the last-occupied LL to the next higher-lying one. the Fermi level never lies in between conducting LLs as the magnetic field is swept and quasi-elastic scattering is always present. In this case. QHE plateaus has no finite width. So. to explain the finite width of the QHE plateaus. one has to invoke the existence of localized i.e.. non-current-carrying. states in the tails of the current-conducting LLs. These localized states are due to the disordered systems. e.g. randon distribution of defects. impurities. .... So. when varying the magnetic field or the number of charge carriers. the Fermi energy will either lie in delocalized. current-conducting states where quasi-elastic scatterings are possible. with $\rho_{xx} \neq 0$. or in localized states. in which case the lower-lying current-conducting charges will require a finite energy to be scattered into an empty conducting states. In such a case. $\rho_{xx} = 0$ at low temperatures and the Hall resistance ρ_{xy} retains a constant value until all of these localized states are filled. Remarkable is that these features exist over a wide range of sample parameters (electron density. mobility. temperature. ...) and are not dependent on the exact shape of the sample. Especially. this QHE has seen an enormous developement in the GaAs/$Al_xGa_{1-x}As$ heterostructures. The reason is that the effective mass is lighter ($\sim 0.067m_0$) than that of Si ($\sim 0.19m_0$), where m_0 is the free electron mass. Since $\omega_c = eB/m^*c$, this lighter electron mass increases the cycloton frequency for a given magnetic field, rendering the QHE obtainable at

lower magneticfields. Of course. the higher mobility of GaAs/$Al_xGa_{1-x}As$ heterostructures lead to the better resolved plateaus. At low magnetic fields. it leads to the *classical Drude model.* When no collisions are present. the Drude model shows that $\rho_{xx} = 0$ and $\rho_x \sim B$ which is called classical Hall effect.

In addition to this magnetic field. we can impose the modulation potential to the heterostructure with 2DEG. A source and a drain are added at opposite ends and a metal gate contact is contacted to the top of the AlGaAs layer. Then. the thin layer of GaAs at the interface forms the 2D channel for the electrons to travel the voltage gate region. By altering the gate voltage applied to the gate. the number of electrons in the channel can be varied. This technique is used as the switch on-off device in the ultra small microcomputer chips. And also. the capability of applying this controllable potential via a patterned gate with a grating constant of a few thousand angstroms to this high mobility two-dimensional electron gas (2DEG) at the interface of a GaAs/$Al_xGa_{1-x}As$ heterostructure has allowed experimentalists to study the magnetotransport properties over a wide range of modulation potentials [5. 6. 7. 8. 9. 10. 11. 12. 13. 14. 15. 16. 17. 18]. The modulation potential has been applied in two orthogonal directions or in only one direction.

2D modulation In the presence of a weak periodic one-dimensional (1D) modulation, the longitudinal magnetoresistance, like that for a homogeneous 2DEG,

exhibits the usual Shubnikov-de Haas (SdH) oscillations associated with the filling of successive Landau levels. In addition to the SdH oscillations, there also occurs a new kind of magnetoresistance oscillations (called Weiss oscillations) at magnetic fields below the SdH oscillations [5]. These oscillations are well understood and are attributed to the commensurability of the two relevant length scales, i.e. the period of the lattice and the cyclotron radius of the electrons at the Fermi energy [6, 19, 20, 21, 22]. In this case, the Landau level degeneracy is partially lifted by this 1D periodic potential. The Weiss oscillations have been attributed to the formation of a Hofstadter type energy spectrum [23, 24, 25, 26, 27, 28, 29, 30]. Historically, Hofstadter's butterfly was obtained in the limits of (1) a strong 2D periodic lattice potential confining the electrons and a weak magnetic field in the *tight-binding approximation* (TBA) [23] and (2) a weak 2D periodic perturbation of a Landau-quantized 2DEG [31].

The calculated resistivity as a function of the magnetic field for a 2DEG subjected to a weak 2D modulation has also been reported [10, 11]. In a 2D periodic potential, the magnetotransport properties also have some interesting features. By varying the strength of the modulation, one can achieve a transition from the weak density variations of the 2DEG to the extreme limit where regions are devoid of electrons, i.e. an array of antidots which may also be produced by etching [18, 32, 33]. The suppression of the commensurate Weiss oscillations, the pronounced double peak structure in the magnetoresistance, the presence

of orbits commensurate with the lattice as well as the occurrence of a negative and quenched Hall resistivity about $B = 0$ have been found in a square array of scatterers [18]. The negative Hall resistivity and its quenching [34] as well as the negative longitudinal resistivity [69] have also been observed in a quantum-wire junction. These are explained theoretically [36, 37] but there are no collimated and commensurate orbits as for an array of scatterers. So far, there have been several theoretical explanations for the negative and quenching of the Hall resistivity observed in the array of scatterers as well as their connection to the commensurate peaks in the longitudinal resistivity [38, 39, 40, 41, 42, 43, 44, 45, 46, 47]. In addition to this, the oscillations of the longitudinal resistivity for the strongly modulated potential, were reported [48]. According to Ref. [48], the longitudinal resistivity shows oscillations with a leading period of one flux quantum per unit cell which have their origin in the magnetic band structure. And also it is reported that they do weakly depend on temperature and electron density. Recently, magnetotransport results not only in the square lattice potential but also in rectangular AD superlattices were published [49, 50]. Also, in this case, all the features seen in a recent QMT experiment were reproduced [51]. The quantum oscillations are periodic in magnetic field B for a soft potential with large ADs and periodic in 1/B in the opposite case. In the QD and AD case, detailed results at low magnetic fields with controllable potential have not been reported so far [52].

In this thesis, we will show almost all features seen in experiments and go further to see how these features depend on the strength and the size of the modulations. we calculate the energy spectra and the band part of conductivites and find the corresponding longitudinal and Hall resistivity for AD and QD-like potentials over a wide range of modulation strengths and the steepness of the slope of the potential. There have already been calculations of the magnetoresistance of a 2DEG subject to a weak lateral 2D superlattice potential [20] and no results were presented when the potential is strong. In a series of papers. Gumbs and Huang [43. 44. 45. 46] calculated the magnetoresistance and Hall resistance in a perpendicular magnetic field for an array of ADs and QDs which were simulated by delta function potentials. In this thesis, we extend those calculations to a cosine-potential model which we could use to simulate both weak and strong modulation. large and small size of modulation for ADs and QDs. We exclude the effect due to impurities since our previous calculations [43. 44. 45. 46] reveal that the contribution to the magnetoresistance from impurities is not as large as the band part. In 2D modulation. we will show the oscillations associated with the filling of sub Landau levels in $\sigma_{xx}^{(0)}$ and $\sigma_{yx}^{(0)}$ for low modulation. And at low magnetic fields, the longitudinal resistivities have a double peak structure. It is shown how this double peak structure depends on the size of the scatterers and their strengths. We also exhibit the dependence of the negative and quenching of the Hall resistance on the modulation and the Aharonov-Bohm type oscillations

[36, 53]. We demonstrate Aharanov-Bohm oscillations and large plus-to-minus oscillations in $\rho_{xy}^{(0)}$ for the strong dot potential.

1D modulation With the success of physics systems and devices based on two dimensional(2D) heterostructures, the natural trend was to reduce the dimensionality of the modulation of the system to one dimension(1D), called QW or AntiWire(AW). In an ideal QW case, the low field conductance was shown to be quantized with the conductance equal to $\frac{e^2}{h}$ times the number of channels occupied.[58] However, in a real QW case, there are some respects deviated from ideality. One of those is that the real QW, as realized in a quantum point contact, is not infinitely long and does not have perfect translational sysmetry. This kind of deviation makes the differnet regimes of conductance. [59] The regimes depend on the the length scales of the sample:the length L_1 and width W_1 of the QW or constriction and the elastic mean free path l. In the case of $L_1 > W_1 >> l$, electrons are localized longitudinally and transversely on the length scale l. So, in this case, wire modes no longer have meaning. In other words, the electrons no longer see the one-dimensionality of the wire. Therefore, no states exist that extend from one end of the wire to the other. This regime is similar with the weakly localized 2D modulation case. However, if $l >> L_1$ and W_1, the situation becomes different. In this case, the electrons are affected by the boundaries of the wire. And the quantum states exist that extend from one end of the wire to the other. These occupied quantum channels carry the current from one end to the

other. The conductance is then determined by the quantum-mechanical transmission probabolity of the different states between the two ends. due to the chemical potential differnece. If the width W_1 of the QW is small compared with the Fermi wavelength or the cyclotron orbit size when the magnetic field is perpendicularly applied to the 2D sheet. then the quantum ballistic transport is concerned. The ballistic transport in QW has the different features from the classical behaviour. since the electrons have the wave-like nature. It means that the wires act as waveguides for the electrons so that the resistance of a wire loses its local meaning. In this regime. the boundary conditiones on the contacts become of extreme importance and a system of connected wires show a nonlocal behaviour. Therefore. a current flowing between two contacts might influence the voltage between two other contacts. even though classically no current should flow between the two voltage probes. Accordingly. this regime strongly depends on the sample geometry. One of these effects is the well-known quenching effect in the Hall regime at low magnetic field. Traditionally. this quenching effect was explained by the collimation of the electrons. In this case. the ratio of the longitudinal momentum to the transverse momentum increase and near zero magnetic field. these collimated electrons are preferentially trasmitted straight through the junction, and the Hall voltage is quenched.[60] Another Hall effect in the ballistic wire is negative Hall resistivity. The negative Hall resistivity in the ballistic wire is experimentally and theoretically measured in many papers.[60, 61, 62, 63, 37, 64, 68]

Shown in these papers is that the negative Hall resistivity depends on the sample geometry. In narrow ballistic wires with high-mobility. the predominant source of scattering is reflection of carriers off the confining potential. So. by changing the geometry of the intersection of the Hall probes. they showed quenched. enhanced. or even negative Hall resistances at the low magnetic field. And also Buttiker theoretically showed that the negative Hall resistances was the signature of the four-terminal resistance mearsurements.[37] Another source of the negative Hall resistances is shown in the four terminal magnetoresistance of a multichannel electron waveguide.[65] In this paper. submicron wire is fabricated in extremely high mobility GaAs/AlGaAs heterostructure and only a few transverse. one dimensional subbands or channels carry the current because the width of the QW is comparable to an electron wavelength. In this wire. the negative Hall resistances through the Hall probe at different locations are observed. All of these depend on the geometry of sample or measuring probe. In addtion to this. the length and termination of a piece of wire not conneted to a contact will change the behaviour of the rest of the structure.[58] the length L_1 and the width W_1 of the wire and the hight H_1 of the potential barrier are all crucial factors in ballistic Hall resistances. To our knowledge, there has not been yet published papers about the ballistic Hall effect due to this length or termination of a piece of wire. So, in this paper, we theoretically pursue the negative Hall resistances due to the termination of the piece of the QW, called short QW.

Outline of this thesis The outline of the rest of this thesis is as follows. In Sec. 2. we present the model for the square array of scatterers and the general theory for the calculation of the energy eigenvalues and eigenfunctions using the eigenfunctions of a homogeneous 2DEG as the basis states. Detailed numerical results are given for the eigenvalue spectra and the wave vector dispersion. for various values of the strength and steepness of the scattering potential. In Sec. 3. the general theory for the eigensystems with 1D modulation is derived. And then. with these eigensystems. we calculate all QMT coefficients using Kubo formular in Sec. 4. The numerical QMT results for the 2D modulation are discussed in Sec. 5. where the dependence of the double peak structures for the longitudinal resistivity $\rho_{xx}^{(0)}$ on the strength and the size of the scatterers in strong AD modulation and the quenched Hall effect in the AD and QD regime are discussed. After this. in Sec. 6. the numerical QMT results for the 1D modulation are discussed. In this section. steplike features due to the LL crossing in $\sigma_{xx}^{(0)}$. low-field giant peaks due to anisotropic momentum space in $\rho_{xx}^{(0)}$. quenched (at low magnetic fields). classical (for the low modulation case). and negative (for the short QW) Hall resistivities $\rho_{xy}^{(0)}$ which depend on the geomery of the sample. and threshold peaks in $\rho_{yy}^{(0)}$ which depend on the height of the QW barrier and the width of QW channel. are discussed. Finally, this thesis is ended up with the summary of the present work and conclusions in Sec. 7. The eigenstates for the δ and grid potenital used in this thesis are included in Appendix.

2 Model Hamiltonian and Energy Eigenstates for 2D Modulation

2.1 Model Hamiltonian and Theory for 2D Modulation

The single-particle Hamiltonian for a 2D square array of scatterers placed in the $x-y$ plane in a uniform perpendicular magnetic field $\mathbf{B} = B\hat{z}$ is, using mks units.

$$\mathcal{H}_0 = \frac{1}{2m^*}\left(-i\hbar\nabla + e\mathbf{A}(\mathbf{r})\right)^2 + U_L(\mathbf{r}) \ . \tag{1}$$

where m^* is the effective mass of an electron with charge $-e$. $\mathbf{r}$ is a 2D vector in the $x-y$ plane, and $\mathbf{A}(\mathbf{r}) = (0,\ Bx, 0)$ is the vector potential in the Landau gauge. In Eq. (1), the lattice potential $U_L(\mathbf{r})$ for the scatterers can be taken as having the following form [43, 44, 45, 46]

$$U_L(\mathbf{r}) = V_0 \sum_{i,j} \delta(\mathbf{r} - \mathbf{R}_{i,j}) \ . \tag{2}$$

The approximate form in Eq. (2) for simulating a lattice potential of strong scatterers should be good as long as the lattice potential is very steep and the lattice constant a is much larger than the diameter of the scatterers. Here, $\mathbf{R}_{i,j} = (ia,\ ja)$ is a lattice vector. The δ-function in Eq. (2) is two-dimensional.

Alternative forms of the 2D lattice potential have been used by other authors.

One of those is the *grid potential* defined in Eq. (3) for studying the effect of a weak modulation potential on the magnetotransport of a 2DEG [10, 20].

$$U_L(\mathbf{r}) = \overline{V}_0 \left[u_x \cos\left(\frac{2\pi x}{a}\right) + u_y \cos\left(\frac{2\pi y}{a}\right) \right] . \tag{3}$$

where u_x and u_y are dimensionless.

Since we are interested in studying the effects of scattering off the modulation potential for varying degrees of modulation, we introduce another lattice potential involving only *cross-products* of the cosine functions and having the same period in both the x and y directions.

$$U_L(\mathbf{r}) = \overline{V}_0 \left[\cos\left(\frac{2\pi x}{a}\right) \cos\left(\frac{2\pi y}{a}\right) \right]^{2N} . \tag{4}$$

where $\overline{V}_0 = V_0/a^2$ is taken as a positive (or negative) lattice potential amplitude for the quantum antidot (or dot) regime. a is a lattice constant of the artificially imposed positive (or negative) periodic modulation potential. N is the power of determining the size of the quantum antidot (or dot) potential. (Figure 1 and Figure 2) The reason for taking $2N$ as its power is to always get the positive (or negative) potential when $\overline{V}_0$ is taken as a positive (or negative) value. The value of N describes the steepness or degree of modulation of the potential. Equation (4) has been used to simulate antidots [38] when N is large ($N \sim 20$).

$$\overline{V}_0 \left[\cos\left(2\pi x/a\right)\cos\left(2\pi y/a\right)\right]^{2N}$$

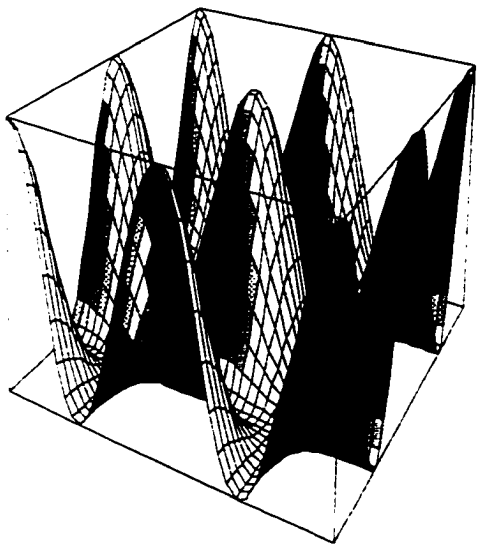

(a) $N = 1$

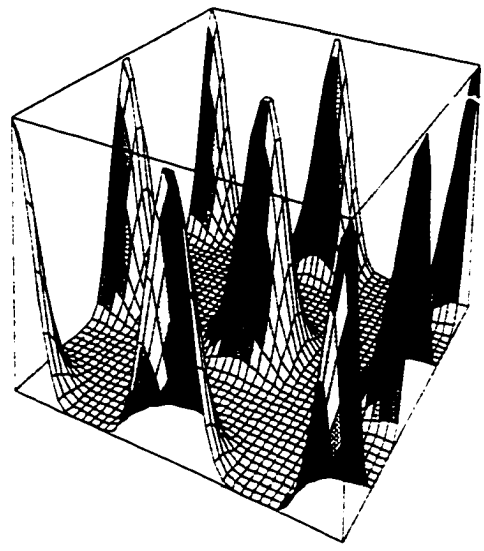

(b) $N = 3$

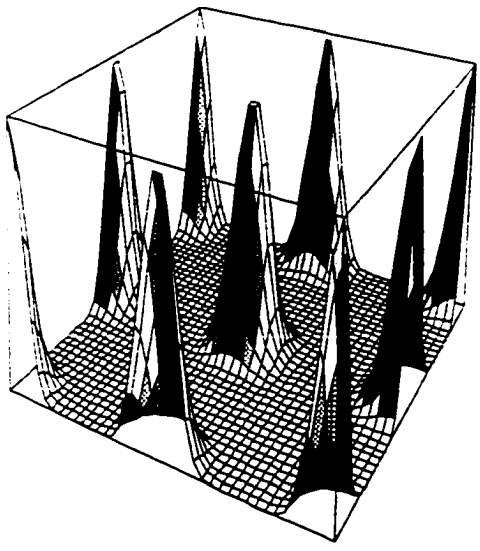

(c) $N = 5$

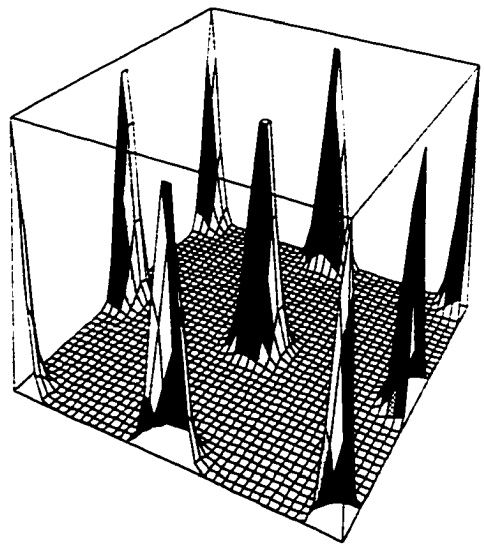

(d) $N = 10$

Figure 1: Anti-dot Potential Barriers with N

$$\overline{V}_0 \left[\cos\left(2\pi x/a\right)\cos\left(2\pi y/a\right)\right]^{2N}$$

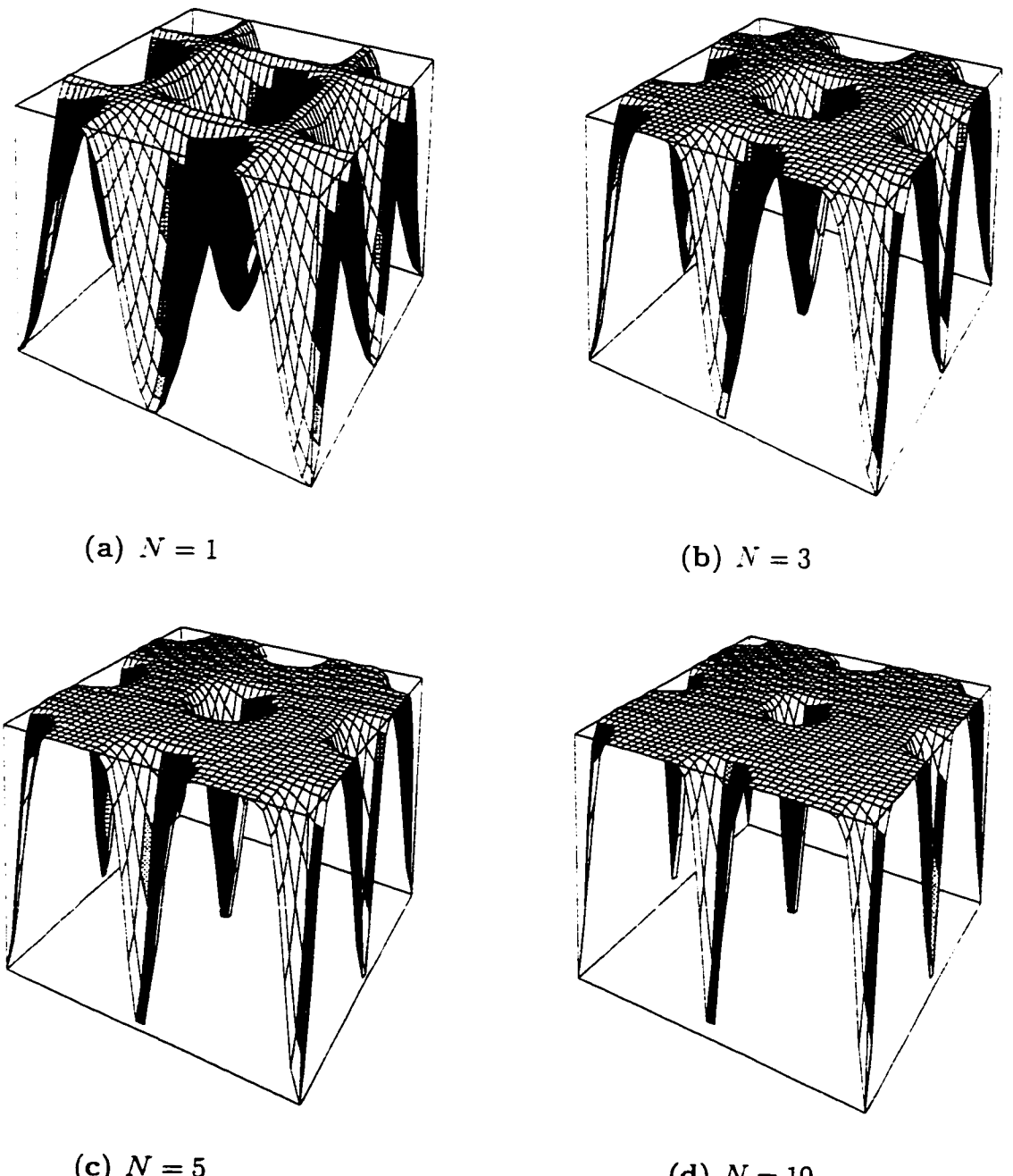

(a) $N = 1$

(b) $N = 3$

(c) $N = 5$

(d) $N = 10$

Figure 2: Quantum-dot Potential Wells with N

When N is sufficiently large, the sharp spikes with very small diameter at the lattice sites make it reasonable to approximate the lattice potential by the simple form in Eq. (2) which reduces the amount of computing required in the calculations. For our model, which includes the finite-size effects of the scatterers, the resulting calculations require considerably more computer time since the potential contribution to the matrix elements in Eq. (9) below involve integrals which cannot be done analytically. However, one of the reasons we are interested in this potential is that we can adjust both the strength of the potential with $\overline{V}_0$ as well as the steepness of the modulation potential by suitably choosing the $2N$ power. So, in our calculations, we choose this potential.

In the absence of impurities, the single-particle eigenfunctions are determined through

$$\psi_{j,X_0}(\mathbf{r}) = \sum_{n,m} C_{n,m}(j,\ X_0)\phi^{(0)}_{n,X_0+mGl_{\mathrm{H}}^2}(\mathbf{r})\ . \tag{5}$$

where

$$\phi^{(0)}_{n,X_0+mGl_{\mathrm{H}}^2}(\mathbf{r}) = \frac{\exp\left[-i(X_0+mGl_{\mathrm{H}}^2)y/l_{\mathrm{H}}^2\right]}{\sqrt{L_y}}$$

$$\times\sqrt{\frac{1}{\pi^{1/2}l_{\mathrm{H}}2^n n!}}\exp\left[-(x-X_0-mGl_{\mathrm{H}}^2)^2/2l_{\mathrm{H}}^2\right]$$

$$\times H_n\left(\frac{x-X_0-mGl_{\mathrm{H}}^2}{l_{\mathrm{H}}}\right)\ . \tag{6}$$

In Eqs. (5) and (6). $n = 0, 1, 2, \ldots$ is a Landau-level index. $m = 0, \pm 1, \pm 2, \ldots$ stands for the umklapp scattering effect and $H_n(x)$ is the nth order Hermite polynomial. Also, $G = 2\pi/a$ is a reciprocal lattice vector. $L_y = N_y a$ is the sample length in the y direction. $X_0 = k_y l_H^2$ is the guiding center. $l_H = \sqrt{\hbar/eB}$ is the magnetic length and k_y is a wave vector along the y direction. The expansion coefficients $C_{n,m}(j, X_0)$ in Eq. (5) are determined from the following matrix equation

$$\sum_{n,m} \left[\left(E_n^{(0)} - E_j(X_0) \right) \delta_{n,n'} \delta_{m,m'} + \frac{V_0}{a^2 \, l_H \pi^{1/2}} \sqrt{\frac{1}{2^{n-n'} n! n'!}} B_{n,n'}^{m,m'}(X_0) \right] \times C_{n,m}(j, X_0) = 0 \, . \tag{7}$$

as well as the orthonormality condition:

$$\sum_{n,m} C_{n,m}^{*}(j, X_0) C_{n',m'}(j', X_0') = \delta_{j,j'} \delta_{X_0, X_0'} \, .$$

From this calculation, we also obtain the secular equation which determines the energy eigenvalues $E_j(X_0)$

$$\mathrm{Det} \left[\left(E_n^{(0)} - E_j(X_0) \right) \delta_{n,n'} \delta_{m,m'} + \frac{V_0}{a^2 \, l_H \pi^{1/2}} \sqrt{\frac{1}{2^{n+n'} n! n'!}} B_{n,n'}^{m,m'}(X_0) \right] = 0 \, . \tag{8}$$

Here, $E_n^{(0)} = (n + 1/2)\hbar\omega_c$ is the energy for the nth Landau level with eigenfunction $\phi_{n,m}^{(0)}(\mathbf{r})$ in the absence of scatterers and the matrix element $B_{n,n'}^{m,m'}(X_0)$ appearing in Eqs. (7) and (8) is defined as follows and, for the potential in Eq. (4), we have

$$B^{mm'}_{n,n'}(X_0) \equiv \left\langle \phi^{(0)}_{n',X_0+m'Gl_H^2}(\mathbf{r})|U_L(\mathbf{r})|\phi^{(0)}_{n,X_0+mGl_H^2}(\mathbf{r})\right\rangle$$

$$= \frac{1}{L_y}\int_{-\infty}^{\infty} dy\ \exp\left[i(m-m')Gy\right]\cos^{2N}(2\pi y/a)$$

$$\times \int_{-\infty}^{\infty} dx\ \exp\left[-\frac{(x-X_0-mGl_H^2)^2+(x-X_0-m'Gl_H^2)^2}{2l_H^2}\right]$$

$$\times H_n\left(\frac{x-X_0-mGl_H^2}{l_H}\right) H_{n'}\left(\frac{x-X_0-m'Gl_H^2}{l_H}\right)\cos^{2N}(2\pi x/a)\ . \qquad (9)$$

It is straightforward to verify that the following periodic relations for the energy eigenvalues follow from Eq. (9): $E_j(X_0) = E_j(-X_0) = E_j(X_0+a) = E_j(X_0 + Gl_H^2)$. If $\Phi = p/q$, where p, q are positive integers and prime. Eq. (9) is unchanged under the simultaneous translations of both $m \to m+p$ and $m' \to m'+p$. As a consequence, $C_{n,m}(j, X_0)$ has the Bloch property and each Landau level will be split into p subbands. Meanwhile, each subband will have a q-fold degeneracy in the first Brillouin zone. This is a result of the commensurability between the magnetic zone $[-a/2l_H^2, +a/2l_H^2]$ and the lattice Brillouin zone $[-\pi/a, +\pi/a]$. Since the coefficient matrix in Eq. (7) is real and symmetric, this means that $C_{n,m}(j', X_0)$ must be real. The Fermi energy is determined from

$$n_{2D} = \frac{2N_y\Phi}{\mathcal{A}}\sum_j \int_{-Gl_H^2/2}^{Gl_H^2/2}\frac{dX_0}{a}\int_{-\infty}^{\infty} dE\ f_0(E-E_F)D_{j,X_0}(E)\ , \qquad (10)$$

where $\mathcal{A}$ is the sample area. By using $\hbar\omega_c$ as an energy scale, a as a length scale, and adopting periodic boundary conditions in the y direction so that $k_y = 2\pi L/a$

where $L = -N_y/2, \ldots, ((N_y/2) - 1)$ are integers, we obtain the dimensionless forms of the eigenfunctions in Eq. (5) as

$$\psi_{j,L}(\bar{\mathbf{r}}) = \sum_{n,m} C_{n,m}(j, L)\phi^{(0)}_{n,(L,N_y)-m}(\bar{\mathbf{r}}) \ .$$

with

$$\phi^{(0)}_{n,(L/N_y)-m}(\bar{\mathbf{r}}) = \frac{\exp\left[-2\pi i\left((L/N_y)+m\right)\bar{y}\right]}{\sqrt{N_y}}$$
$$\times\sqrt{\frac{2\pi^{1/2}\Phi}{2^n n!}}\exp\left[-\pi\Phi\left(\bar{x}-\frac{(L/N_y)+m}{\Phi}\right)^2\right]$$
$$\times H_n\left[\sqrt{2\pi\Phi}\left(\bar{x}-\frac{(L/N_y)+m}{\Phi}\right)\right] \ . \tag{11}$$

where the expansion coefficients are obtained from

$$\sum_{n,m}\left[\left(n+\frac{1}{2}-E_j(L)\right)\delta_{n,n'}\delta_{m,m'}+\frac{U_0}{\sqrt{\Phi}}\sqrt{\frac{1}{2^{n-n'}n!n'!}}B^{m,m'}_{n,n'}(L)\right]$$
$$\times C_{n,m}(j, L) = 0 \ . \tag{12}$$

and the matrix elements are given by

$$B^{mm'}_{n,n'}(L) = \frac{a}{N_y}\int_{-\infty}^{\infty} d\bar{y}\ e^{2\pi i(m-m')\bar{y}}\cos^{2N}(2\pi\bar{y})$$
$$\times\int_{-\infty}^{\infty} d\bar{x}\ \exp\left[-\pi\Phi\left(\left(\bar{x}-\frac{(L/N_y)+m}{\Phi}\right)^2+\left(\bar{x}-\frac{(L/N_y)+m'}{\Phi}\right)^2\right)\right]$$
$$\times H_n\left[\sqrt{2\pi\Phi}\left(\bar{x}-\frac{(L/N_y)+m}{\Phi}\right)\right]H_{n'}\left[\sqrt{2\pi\Phi}\left(\bar{x}-\frac{(L/N_y)+m'}{\Phi}\right)\right]$$
$$\times\cos^{2N}(2\pi\bar{x}) \ . \tag{13}$$

Here, $U_0 = m^* V_0/\sqrt{2}\pi\hbar^2$, N_x is the number of unit cells in the x direction, $\bar{x} = x/a$, $\bar{y} = y/a$. The zero determinant of the coefficient matrix in Eq. (12)

gives the energy eigenvalues $E_j(L)$. With these results, the eigenvalue spectra and wave-vector dispersion curves are presented.

2.2 Numerical Results and Discussion for Energy Eigenstates; 2D Modulation

For the homogeneous 2DEG in the perpendicular magnetic field to that plane, the energy eigenvalues are the well-known Landau levels (LLs). $\hbar\omega_c(n+\frac{1}{2})$ (from a harmonic-oscillator-like potential), where $\hbar$ is Planck's constant divided by 2π, ω_c is the cyclotron frequency given as eB/m^*, and $n = 0, 1, 2, \cdots$ is a LL index. When there is no modulation potential in the homogeneous 2DEG, the eingenvalues (LLs) are flat functions of the magnetic field in $E/\hbar\omega_c$ vs. $\Phi = Ba^2/\phi_0$ graph.where $\phi_0 = h/e$ is the flux quantum. (Figure 3)

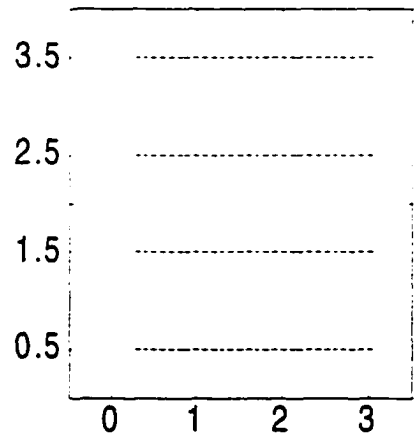

Figure 3: Energy Eigenvalues $E/\hbar\omega_c$ vs. $\Phi = Ba^2/\phi_0$ for no modulation.

This flatness is changed when a modulation potential is introduced to the homogeneous 2DEG. When a modulation potential, in our case taken as Eq. (4), is applied to the 2DEG layer, the LLs scaled by the cyclotron energy are not independent of B any more and are broadened due to the scattering of the imposed potential to make a band of LLs.

In this section, we present the numerical results for the eigenvalues and the dispersion curves for the array of quantum antidot and dot potential simulated by the Eq. (4).

2.2.1 Dependence of the Eigenvalues on N

Antidot regime with N Shown in Fig. 4 (a), (b), (c), and (d) is the results of the eigenvalues for the anti-dot potential (U_0 or $V_0 > 0$) with $N = 1, 3, 5,$ and 10, respectively. First, Fig. 4 (a), (b), (c), and (d) shows us how the LL energy spectra are affected by the magnetic field B (or Φ). In the whole Fig. 4 (a), (b), (c), and (d), the upward shift is more significant in low magnetic field region (small Φ) than in the high magnetic field region (large Φ). When $\Phi \ll 1$, the cyclotron orbit of the electron is very large so that its orbit includes many anti-dots. (Table 1 Actually, the classical radius r_c is given by $\sqrt{(n+1)(\hbar/eB)}$. In this large orbit regime, the probability of being scattered by the modulation potential is increased. For this reason, the energy levels at low magnetic fields are more shifted up than those at high magnetic fields.

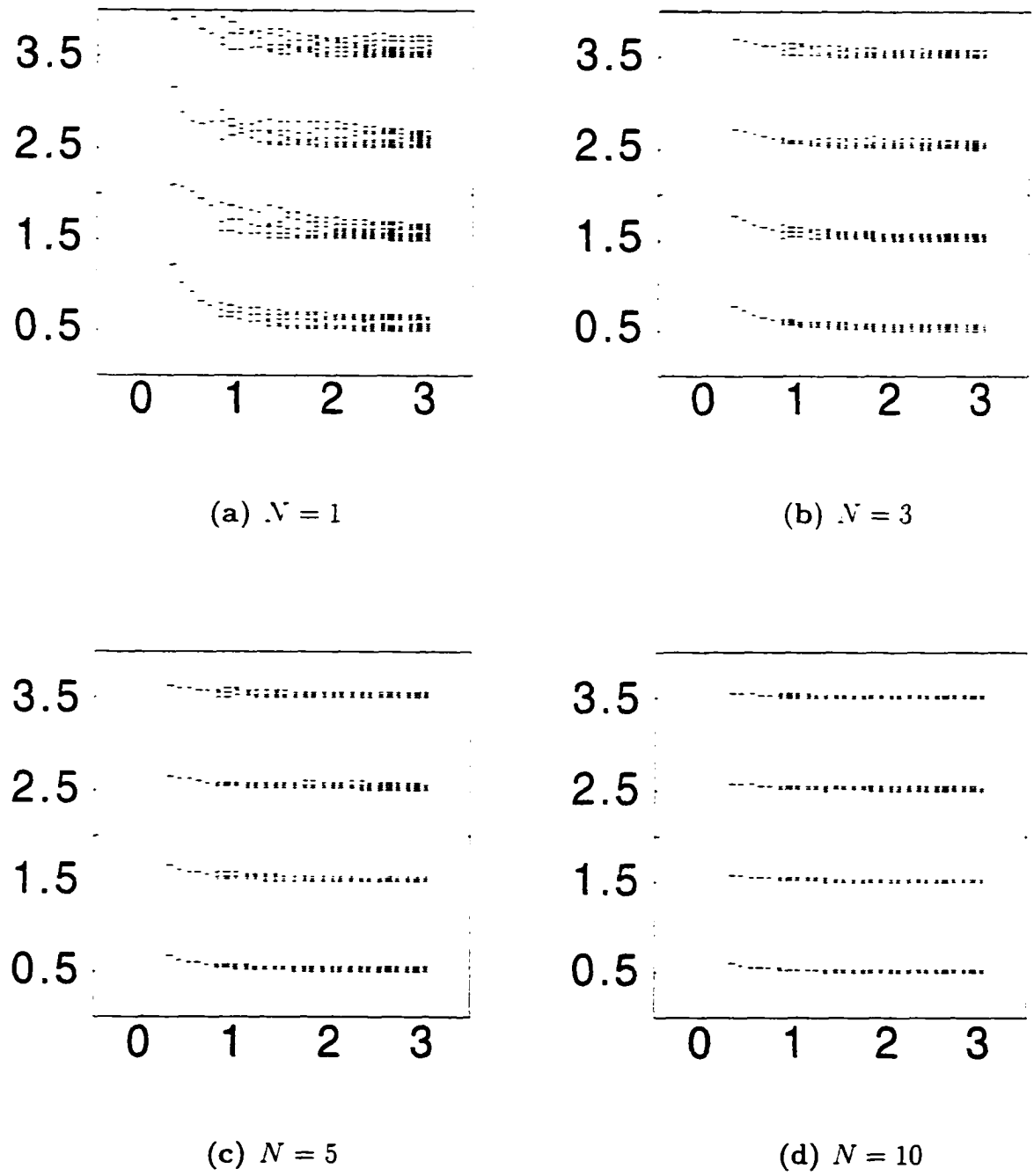

(a) $N = 1$ (b) $N = 3$

(c) $N = 5$ (d) $N = 10$

Figure 4: Energy Eigenvalues $E/\hbar\omega_c$ vs. $\Phi = Ba^2/\phi_0$ with N for anti-dot regime, where $N_x = N_y = 4, n = 3, U_0 = 1.235$ for $m^* = 0.067m_0$ (m_0 is the free electron mass) and $a = 200nm$.

Table 1: $\Phi vs. B$ and corresponding cyclotron radii $r_c(nm)$ for $200nm$

Φ	$B(T)$	$r_c(n=0)$	$r_c(n=1)$	$r_c(n=2)$	$r_c(n=3)$
0.1	0.0104	252	436	563	667
0.2	0.0207	179	310	400	474
0.3	0.0311	146	253	326	386
0.4	0.0414	126	218	282	333
0.5	0.0518	113	196	253	299
0.6	0.0621	103	178	230	273
0.7	0.0725	95	165	212	251
0.8	0.0828	89	154	199	235
0.9	0.0932	84	145	188	222
1.0	0.1035	80	139	179	212
1.1	0.1139	76	132	170	201
1.2	0.1242	73	126	163	193
1.3	0.1346	70	121	157	185
1.4	0.1449	68	118	152	180
1.5	0.1553	65	113	145	172
1.6	0.1656	63	109	141	167
1.7	0.1760	61	106	136	161
1.8	0.1863	60	104	134	159
1.9	0.1967	58	100	130	153
2.0	0.2070	56	97	125	148
2.1	0.2174	55	95	123	146
2.2	0.2277	54	94	121	143
2.3	0.2381	53	92	119	140
2.4	0.2484	52	90	116	138
2.5	0.2588	51	88	114	135
2.6	0.2692	50	87	111	132
2.7	0.2795	49	85	110	130
2.8	0.2899	48	83	107	127
2.9	0.3002	47	81	105	124
3.0	0.3106	46	80	103	122

where. $\Phi = Ba^2/\phi_0$ and $r_c = \sqrt{(n+1)(\hbar/eB)}$

When Φ is increased, the cyclotron orbit of the electron is reduced and thus the probability of being scattered by the modulation potential is decreased. So the shift from LLs at the high magnetic field becomes less than at the low magnetic field. Therfore, the shift of the eigenvalues from LLs is reduced as Φ is increased (i.e. the magnetic field B is increased). Secondly, what the Fig. 4 (a), (b), (c), and (d) shows us is how LLs are broadened for the different size of positive potentials given by Eq. (4). When N is increased, the size (or diameter) of the scatterers is decreased. (Fig. 1) If the size of the scatterers is decreased, the space between the scatterers becomes larger so that the probability of an electron being scattered by the potential is decreased and the electron can move more freely between the scatterers. For this reason, the shift from the LLs is reduced when N is increased. The third one shown in this Fig. 4 (a), (b), (c), and (d) is the fact that the band width of the modulation-broadened LLs oscillates with the magnetic field B or Φ. It can be thought that when the cyclotron radius is changed (in other words, gradually increased or decreased), the electron is periodically scattered by the periodic scatterers. Whenever the electron with the circular motion meets the scatterers, the band width of the broadened LLs becomes thick. When the electron motion is freely from the scatteres, the band wdth becomes thin. That is why the oscillation of the band width in the low magnetic field region is more than in the high magnetic field region. In our case, the cyclotron diameter is compatible with the spacing between scatterers when $\Phi = 1.3$. So, the oscillation

of the band width is larger in the region of $\Phi < 1.3$ than in the region of $\Phi > 1.3$. This kind of oscillation of the band width with Φ is more obviously appeared in grid potential modulation given by Eq. (3) (ref. Appendix B). (Fig. 5)

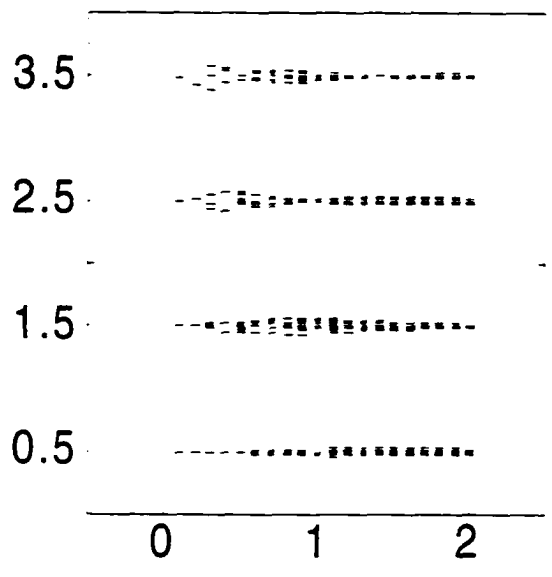

Figure 5: $E/\hbar\omega_c$ vs. $\Phi = Ba^2/\phi_0$ for the grid potential given by Eq. (3). Here, $N_x = N_y = 10, n = 8, U_0 = 1.235$ and $u_x = u_y = 1$.

In this Fig. 5, the eigenvalues are above or below each unperturbed LLs. The reason is that as shown in Eq. (3), the modulation potential is proportional to the bare cosine functions with no power which can have positive or negative values and thus the total Hamiltonian can have energies above or below each unperturbed LLs. These modulation-broadened each LLs have some oscillations as Φ increases. We used the different kind of periodic modulation grid potential to obtain the eigenvalues, but still we can observe the oscillatory behaviour of each

modulation-broadened LLs with Φ. From this fact, we can know that the electron is periodically scattered by the periodic modulation potential when the cyclotron radius is gradually reduced or increased. However, each broadened LLs have different phases. The second LL has the maximum band width around $\Phi = 1$ but the third one has it around $\Phi = 0.5$ and so on. Theses different phases come from the fact that the cyclotron radius depends on the LL index. As mentioned above, the cyclotron radius is proprtional to $\sqrt{n+1}$. So, the cyclotron radius is changed by the LL index n for fixed Φ. These different cyclotron radii of each broadened LLs for fixed Φ make the different scattering effects from the periodic modulation potential. Therefore, these differnet phases of each broadened LLs reflects that the cyclotron radius depends on the LL index. This kind of oscillatory phenonmenon for the band width of the modulation-broadened LLs agrees with the other paper's.[21]

Quantum-dot regime with N Shown in Fig. 6(a), (b), (c), and (d) are the eigenvalues for the dot potential (U_0 or $\overline{V}_0 < 0$) with $N = 1$, 3, 5, and 10, respectively. In this regime, all the eigenvalues are shifted *down* instead of *up* shown in the antidot regime. It can be shown from Eq. (1) and (4). Because $\overline{V}_0 < 0$, the total Hamiltonian would be less than the unperturbed LLs. As in the anti-dot regime, the shift-down is more in low magnetic field region (small Φ) than in the high magnetic field region (large Φ). It can be explained with similar reason as mentioned in the anti-dot regime.

Dependence of the Eigenvalues on N (QD regime)

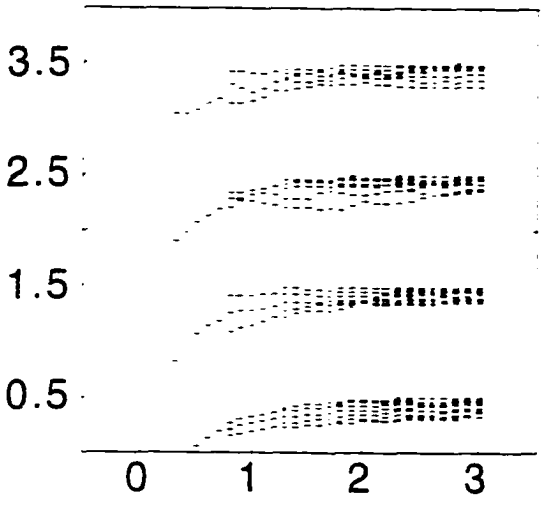

(a) $N = 1$

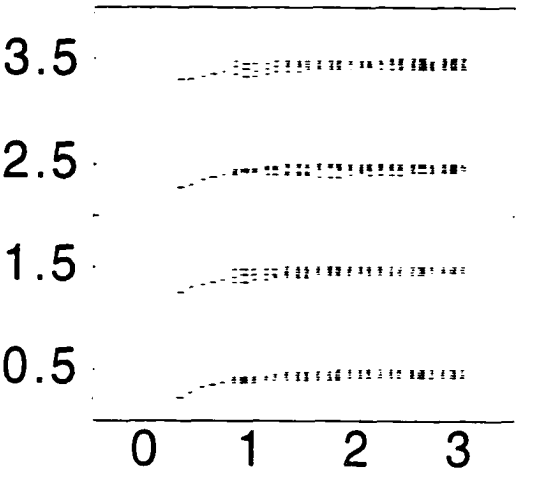

(b) $N = 3$

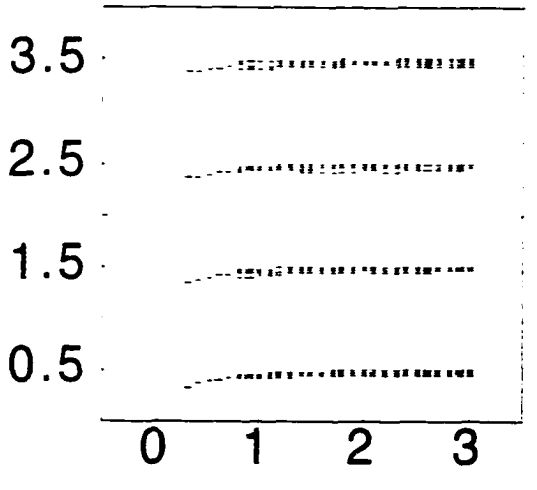

(c) $N = 5$

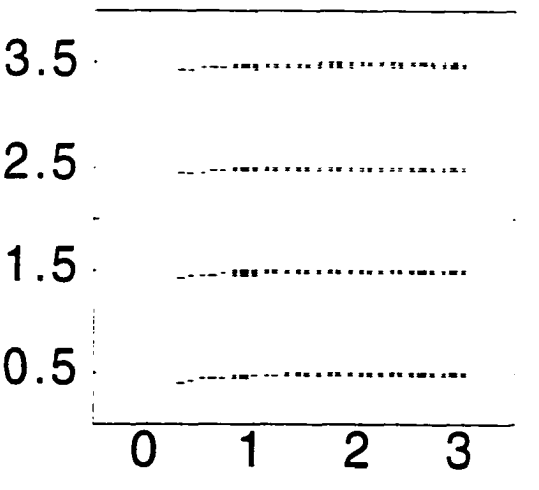

(d) $N = 10$

Figure 6: Energy Eigenvalues $E/\hbar\omega_c$ vs. $\Phi = Ba^2/\phi_0$ with N in quantum-dot regime, where $N_x = N_y = 4, n = 3, U_0 = -1.235$. Since $U_0 = m^*\overline{V}_0 a^2/(2^{1/2}\pi\hbar^2)$. $\overline{V}_0 = -0.156\ meV\ \mathring{A}^2$ for $m^* = 0.067m_0$ and $a = 200nm$.

At low magnetic fields. the cyclotron radius of the electron is relatively large and so the electron can have more possibility to be trapped in the negative potential before the orbit of the electron is closed by the magnetic field since it includes more negative potential wells. For this reason. at low-magnetic fields. the energies are appreciably shifted down from the unperturbed LLs. On the other hand. as Φ increases. the shift is reduced and the constant band width is displayed. This is because the cyclotron radius is reduced when Φ increases and if the electron orbit is comparable with or less than the space between dots. the confinement of electrons between quantum dots increases and there are more possible states in the space between dots in which they are relatively unaffected by the negative potential. That is why the eigenvalues in the higher magnetic field regime are not much shifted down from the LLs. And also. owing to this reason. all the energy eigenstates with Φ at high magnetic fields have almost the same band width as the others. As in the anti-dot regime. the shift is reduced when N is increased. This is related to the size of the confining region. If N increases. the size of the potential decreases. and so the space between dots becomes relatively large. Thus the electrons have more probability of being in the space between the quantum dots and those electrons are relatively unaffected by the negative potential and thus the broadening of LLs at high magnetic fields is shrunken. Another size effect is shown in Fig. 6(a). Some states shifted down from the lowest LLs in the low magentic field region are negative and bounded

in the negative potential.

2.2.2 Dependence of the Eigenvalues on U_0

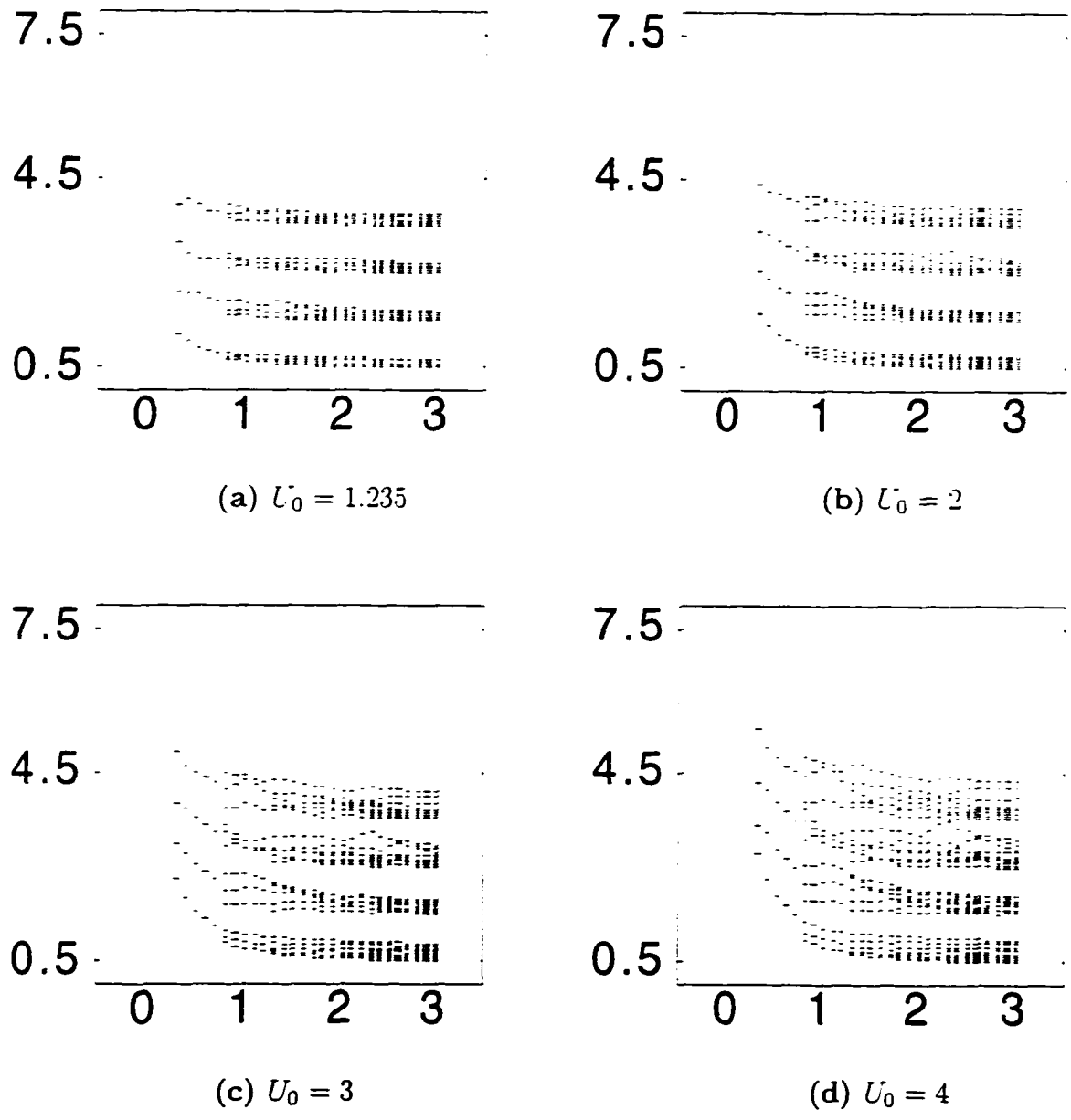

(a) $U_0 = 1.235$ (b) $U_0 = 2$

(c) $U_0 = 3$ (d) $U_0 = 4$

Figure 7: Energy Eigenvalues $E/\hbar\omega_c$ vs. $\Phi = Ba^2/\phi_0$ with U_0 for anti-dot regime, where $N_x = N_y = 4, n = 3$, and $N = 1$.

Antidot regime with U_0 Dependence of the eigenvalues on U_0 is shown in Fig. 7 (a), (b), (c), and (d). As in the previous section, we can also see that the upward shift is more significant in low magnetic field region (small Φ) than in the high magnetic field region (large Φ). But, in this section, we will see the dependence of the eigenvalues on the modulation potential strength U_0 instead of its size N. As expected, when U_0 increases, the LLs are more shifted up at low magnetic fields and more broadened at high magnetic fields. It can be mathematically understood in Eq. (4) in which the total Hamiltonian will be increased when the modulation potential strength U_0 is increased. So, each LL will be more shifted and more broadened by the modulation potential with stroger strength. It can be also physically understood: the stronger the potential is, the scattering effect is more. So, the band width of the braodened LL is increased when the potential strength U_0 is increased. In this low modulation case, all the eigenvalues are above each unperturbed LLs. When the potential strength is increased further, the LLs are more broadened and closely go to next LL and eventually overlap each other as can be seen in Fig. 8 (a). In this strong modulation case, the Landau orbits are mixed each other and this leads to substantial modification of the group velocities. If the strength of the scatterers is sufficiently strong, then the eigenvalues become less than 0.5 which is the lowest LL in the unit of $\hbar\omega_c$ and can even be negative as shown in Fig. 8 (b). In this extremely strong case, the electron starts to behave as if it is bounded among the extremely strong potential

walls.

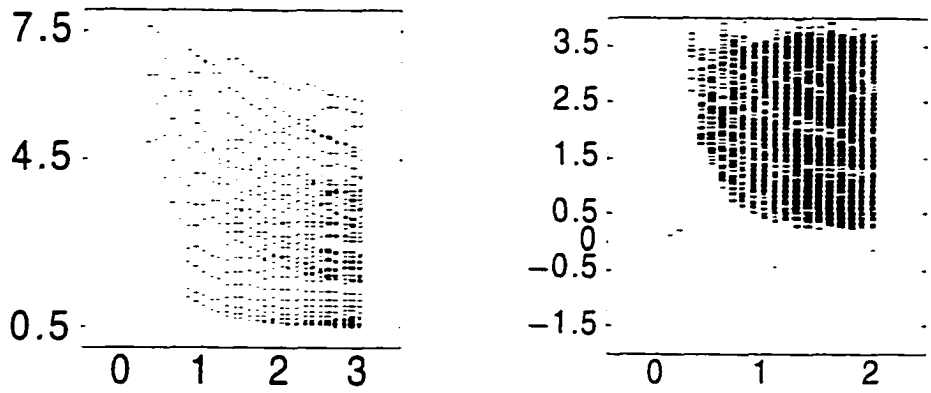

(a) $U_0 = 10$ (b) $U_0 = 5 \times 10^{14}$

Figure 8: $E/\hbar\omega_c$ vs. $\Phi = Ba^2/\phi_0$ for the very strong modulation potential, where (a) $N_x = N_y = 4$, $n = 3$, and $N = 1$ for Eq. (4) and (b) $N_x = N_y = 10$, $n = 3$ for Eq. (2).

Quantum-dot regime with $-U_0$ Fig. 9 (a), (b), (c), and (d) show how the eigenvalues depend on negative U_0. As in the anti-dot case, we can see that the shift is more down in low magnetic field region than in the high magnetic field region. And also, when U_0 is negatively increased, the LLs are more shifted down at low magnetic fields and more broadened at high magnetic fields with the same reason as in the anti-dot case. In Fig. 9 (a), only the electron in the lowest LL is first bounded at low magnetic fields. Then, the electron in the next lowest LL starts to be bounded at low magnetic fields when the potential strength U_0 is negatively increased as seen in Fig. 9 (c). In this case, the reason of the electron being bounded is that it has large orbit at low magnetic fields and so it has more probability of being bounded by the negative potential.

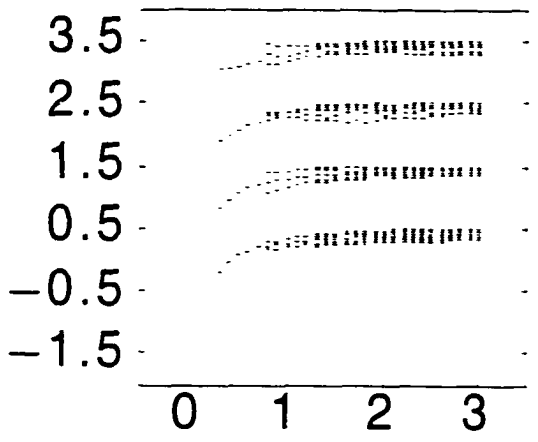

(a) $U_0 = -1.235$

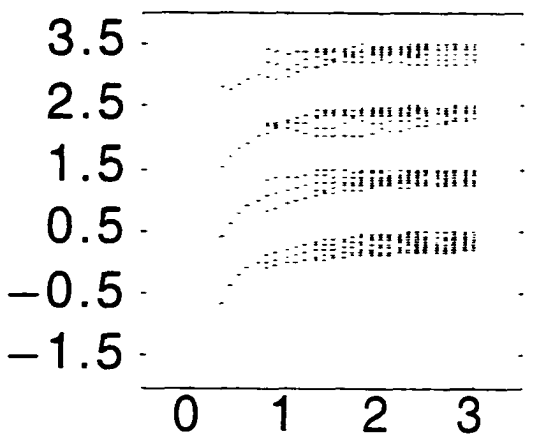

(b) $U_0 = -2$

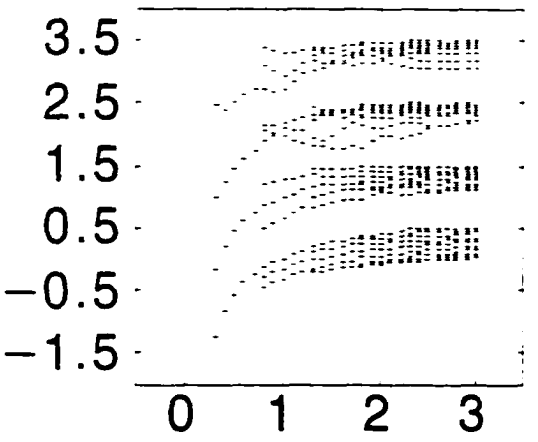

(c) $U_0 = -3$

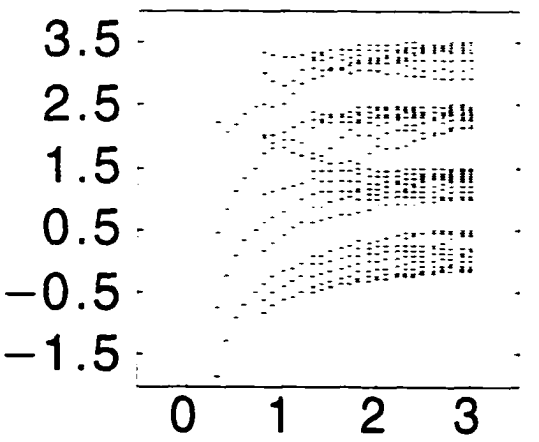

(d) $U_0 = -4$

Figure 9: Energy Eigenvalues $E/\hbar\omega_c$ vs. $\Phi = Ba^2/\phi_0$ with $-U_0$ for quantum-dot regime, where $N_x = N_y = 4, n = 3$, and $N = 1$.

However. there are two kinds of phenomena in being bounded. One possible phenomenon .as previously mentioned. occurrs when the electron with the large orbit so as to have more probability of being bounded meets with the negative potential. This phenomenon is seen at low magnetic fields in Fig. 9 (a). (b). (c). and (d). And the other possible one occurs when the electron has smaller orbit than the diameter of the quantum-dot potential. This electron with the small obit ether can be localized in the region between quantum dots or can be sunk into the dot if it is small enough. If this electron is confined inside the dot. then it will have the negative eigenvalues. We can see this phenomenon from Fig. 10.

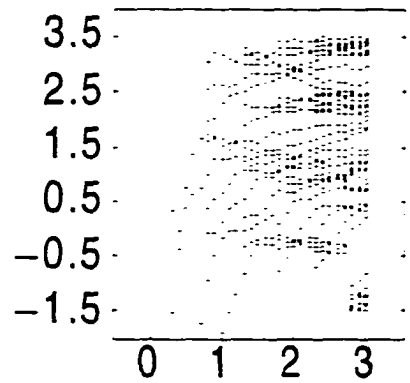

Figure 10: Energy Eigenvalues $E/\hbar\omega_c$ vs. $\Phi = Ba^2/\phi_0$ for the negatively strong modulation potential.Here, $N_x = N_y = 4, n = 3, U_0 = -10$, and $N = 1$.

Fig. 10, is the results for the negative and strong potential ($U_0 = -10$) with large diameter ($N = 1$). In this figure, the energy eigenvalues of the lowest LL at the high magnetic fields around $\Phi = 3.0$ (which generates the small orbit) are

negative. If the orbit is small enough. the negative potential is strong enough. and the diameter of the quantum dot is large enough. then the electron will be sunk into the quantum dot and its eigenvalues become negative. Therefore. this negative eigenvalues of the lowest LL around $\Phi = 3.0$ reflect that the electron with small orbit can be confined by the quantum dot. (Table 1)

2.2.3 Energy Dispersion Curves for Anti-dot

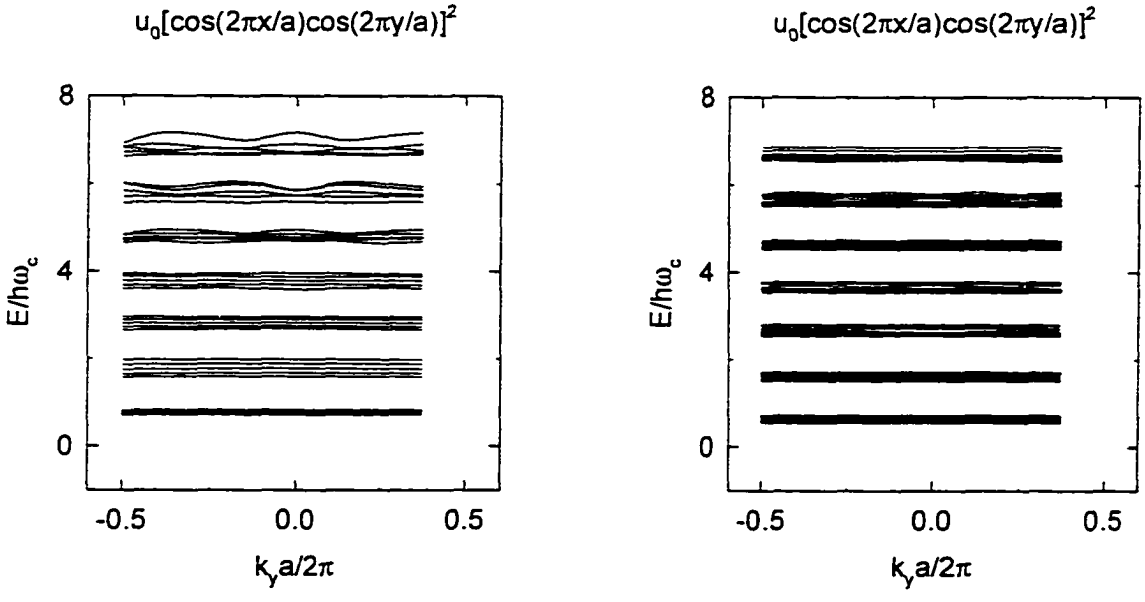

(a) $\Phi = 0.7$ (b) $\Phi = 1.5$

Figure 11: Plots of the Energy Dispersion $E/\hbar\omega_c$ as a function of the wave vector k_y for a chosen scattering potential given in Eq. (4) with $U_0 = 1.235$ and $N = 1$. Here, $U_0 = m^* V_0 a^2/(2^{1/2}\pi\hbar^2)$ and two values of the magnetic flux Φ are employed. For the array size, we chose $N_x = N_y = 8$.

Antidot regime Fig. 11 (a) and (b) present the wave-vector (ydirection) dispersion of the energy eigenvalues for the potential in Eq. (4) with $N = 1$, $U_0 =$

1.235 and for two magnetic fields corresponding to $\Phi = 7/10$. $3/2$. respectively. Our calculations show that each LL broadens into a band due to the scattering by the modulated potential but there is no overlap between different Landau bands for either $\Phi = 7/10$ or $\Phi = 3/2$ since this is the result for the weak modulation. However. the energy band width for $\Phi = 7/10$ are wider than for $\Phi = 3/2$. The reason for this is that the Landau orbit of an electron for $\Phi = 7/10$ is larger than for $\Phi = 3/2$ and thus the Landau orbit for $\Phi = 7/10$ has more probability of being scattered by the modulation potential. Another numerical result is that the Landau band width oscillates with LL index. This result is well seen in Fig. 11 (a). This effect is due to the fact that the cyclotron radius is proportional to $\sqrt{2n+1}$. When n is increased. the cyclotron radius increases. Whenever the cyclotron radius is matched with the lattice constant of the periodic potential. the LL of the electron is more broadened by the potential. So. the electron with the radius changed by the LL index is periodically scattered with the period of modulation potential. If this radius is large (low magnetic field region. small Φ). then it experiences several modulation period and if it is small (high magnetic field region. large Φ). then it is relatively difficult to experience the modulation period. That is why the energy band width for $\Phi = 7/10$ more oscillates than that for $\Phi = 3/2$. This result agrees with other papers on low modulation case. [6, 46]

Fig. 12 (a) and (b) present the wave vector (y direction) dispersion of the energy levels for a square array of δ potential given in Eq. (2). (cf. Appendix A)

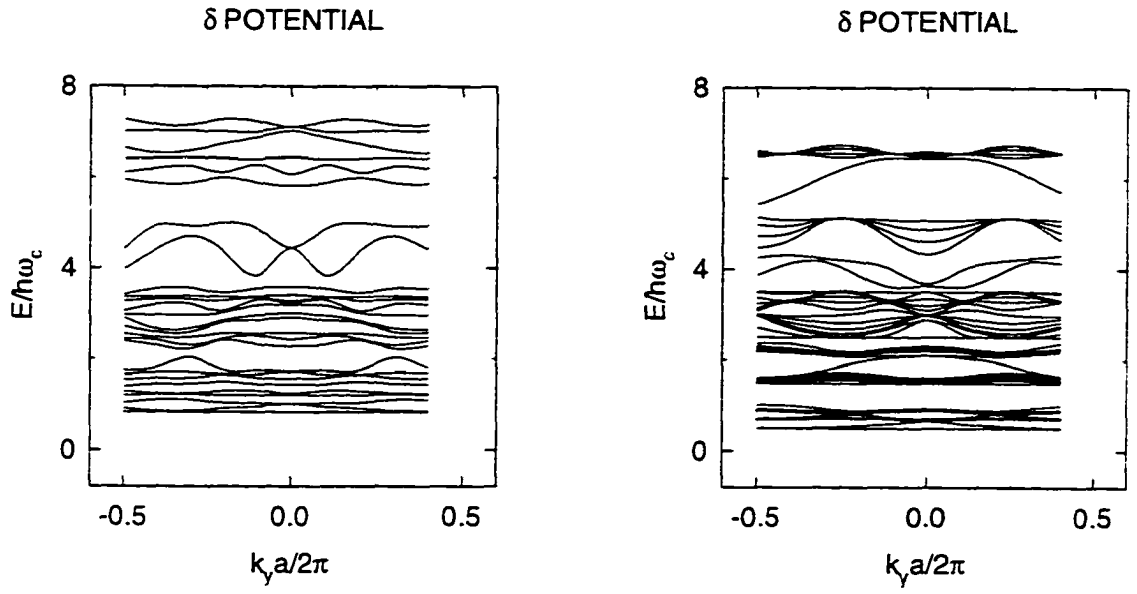

(a) $\Phi = 0.7$ (b) $\Phi = 1.5$

Figure 12: Plots of the Energy Dispersion $E/\hbar\omega_c$ as a function of the wave vector k_y for the δ potential given in Eq. (2) with $U_0 = 1.235$. For the array size, we chose $N_x = N_y = 10$.

In this anti-dot regime, there is almost mixing of the Landau orbits with different guiding centers by the modulated potential. And, as in Fig. 11 (a) and (b), the bandwidth of LL oscillates with LL index in either Fig. 12 (a) or (b)since the cyclotron radius is proportional to $\sqrt{2n+1}$. Observed in Fig. 12 (a) and (b) is the drifting velocity. The drift velocity in the y-direction is given $\hbar^{-1} dE_j(X_0)/dk_y$. So, the steeper slope means the strong dispersion which leads to large drifting velocity. In our case, the dispersion for $\Phi = 7/10$ is weaker than

for $\Phi = 3/2$ which means that the drift velocity of an electron for $\Phi = 7/10$ is less than that for an electron for $\Phi = 3/2$. This is because the radius of the Landau orbit for $\Phi = 7/10$ is larger than that for $\Phi = 3/2$ and thus the probability of scattering when $\Phi = 7/10$ is larger than that when $\Phi = 3/2$. This reflects that the electron is more affected by the scattering off the potential instead of the drift. For $\Phi = 3/2$ in Fig. 12 (b). it is clear that the LLs are split into $p = 3$ subbands and there are $q = 2$ periods in the first Brillouin zone. When the magnetic flux per unit cell of the lattice Ba^2 is a rational multiple of the flux quantum $\phi_0 = hc/e$. one can introduce a new unit cell called magnetic unit cell (MUC). This MUC is used for the invariance of the system with respect to the magnetic translations. If $\Phi = Ba^2/\phi_0 = p/q$ with integers p and q. the MUC can be spanned by the new basis vectors $\mathbf{b}_x = (qa.0)$ and $\mathbf{b}_y = (0.a)$. So. each MUC carries p flux quanta. The equivalent construction in k space is the magnetic Brillouin zone (MBZ) which contains all $\mathbf{k}$ vectors with $\mid k_x \mid \leq \pi/qa$ and $\mid k_y \mid \leq \pi/a$. This effective enlargement of the period of the potential in the x-direction induces additional band gaps. Therfore, the Landau bands split into p subbands. In our case, since $\Phi = 3/2$, each MUC (which contains two regular lattice points in x-direction and one in y-direction) carries 3 flux quanta. Therefore, we can observe the fact that LLs are split into $p = 3$ subbands and there are $q = 2$ periods in the first Brillouin zone.[28, 54]

2.2.4 Energy Dispersion Curves for Quantum-dot

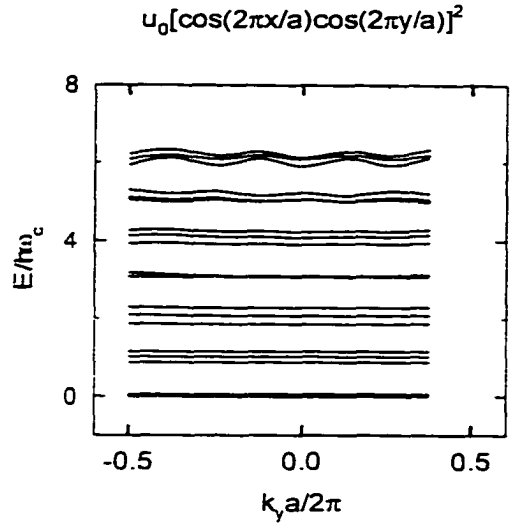

(a) $\Phi = 0.5$

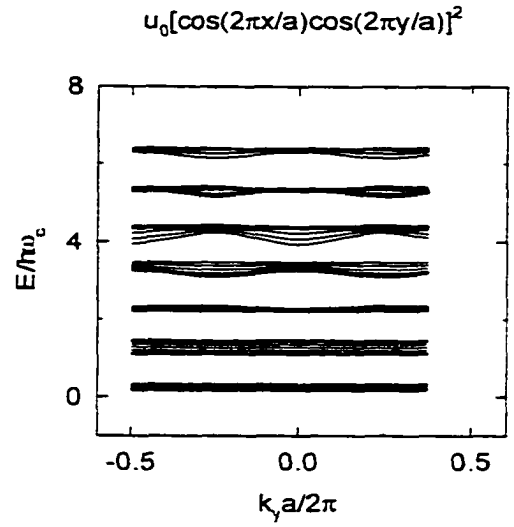

(b) $\Phi = 1.0$

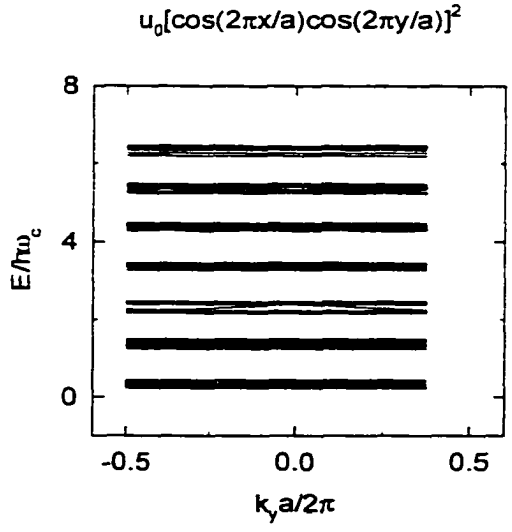

(c) $\Phi = 1.5$

Figure 13: Plots of the Energy Dispersion $E/\hbar\omega_c$ as a function of the wave vector k_y for a chosen scattering potential given in Eq. (4) with $U_0 = -1.235$ and $N = 1$. Here, $U_0 = m^* V_0 a^2/(2^{1/2}\pi\hbar^2)$. For the array size, we chose $N_x = N_y = 8$.

Quantum-dot regime Shown in Fig. 13 (a). (b). and (c) are the dispersion curves within the first Brillouin zone for the potential with $N = 1$. $U_0 = -1.235$ and $\Phi = 0.5$. 1.0.and 1.5 respectively. It is shown that the bandwidth of each LL oscillates with the LL index as in the case of the antidot potential. This feature is more obvious for low magnetic fields ($\Phi = 0.5$). This one agrees with the result for the anti-dot case and is explained with the same reason as in the anti-dot case. Next shown in Fig. 13 (a). (b). and (c) is about the dispersion. In our numerical calculations. because $M = (N_x\Phi - 1)/2$ and in each Landau band. we have N_y Bloch states in the first magnetic Brillouin zone. there are $N_x.N_y\Phi$ states in each Landau band. In other words. there are $M = (N_x\Phi - 1)/2$ states per each N_y Bloch state of each Landau band. Since the Fermi energy is given by $N_F = N_x.N_y n_{2D}a^2/2$. the Fermi energy can be determined by simply counting the energy levels after ordering all the energy levels by magnitude. In our case. the Fermi energy is in the Landau band index $n = 5$ (for $\Phi = 0.5$). $n = 3$ (for $\Phi = 1.0$). and $n = 1$ (for $\Phi = 1.5$). Fig. 13 shows that only the electronic states near the LL $n = 5$ (a). $n = 3$ (b). $n = 1$ (c) have dispersion and all the others have flat bands. All these flat bands come from the fact that they are bound by the negative potential or quantum dot and their wavefuntions in adjacent dots do not overlap. Therefore. the electronic states near the Fermi level have the relatively large contribution. (Table 2)

Table 2: Comparison of LL with Fermi level for Φ in 2D QD modulation

Φ	m	$2m+1$	no. of states	Fermi Level
$0.4 \sim 0.6$	1	3	21	$n = 5$
$0.7 \sim 0.8$	2	5	35	$n = 3$
$0.9 \sim 1.1$	3	7	49	$n = 2$
$1.2 \sim 1.3$	4	9	63	$n = 1$
$1.4 \sim 1.6$	5	11	77	$n = 1$
$1.7 \sim 1.8$	6	13	91	$n = 1$

where. $\Phi = Ba^2/\phi_0$. $m = Intof(N_x\Phi - 1)/2$. No. of states$= (n+1)(2m+1)$. Fermi level $N_F = N_x N_y n_{2D} a^2/2 = 16$ when $N_x = N_y = 8$. $n = 6$. and $n_{2D}a^2 = 0.5$.

3 Energy Eigenstates for the 1D Modulaion (QW)

The single-particle Hamiltonian for a 1D array of QW in 2DEG placed in the $x-y$ plane in a uniform perpendicular magnetic field $\mathbf{B} = B\hat{z}$ is. using mks units.

$$\mathcal{H}_0 = \frac{1}{2m^*}\left[-i\hbar\nabla + e\mathbf{A}(\mathbf{r})\right]^2 + U_{\rm L}(\mathbf{r}) \ . \tag{14}$$

where m^* is the effective mass of an electron with charge $-e$. $\mathbf{r}$ is a 2D vector in the $x-y$ plane. and $\mathbf{A}(\mathbf{r}) = (0.\ Bx.0)$ is the vector potential in the Landau gauge. In Eq. (14). the lattice potential $U_{\rm L}(\mathbf{r})$ for the x-directional and y-directional modulation can be taken as having the following form. respectively

$$U_{\rm L}(\mathbf{x}) = \bar{V}_0\left[\cos\left(\frac{2\pi x}{a}\right)\right]^{2N} . \tag{15}$$

. where $\bar{V}_0$ is taken as a positive potential barrier amplitude for the QW regime. a is a periodic distance between the artificially imposed one demensional positive periodic potential barriers, and N is the power of determining the width of the QW potential barrier. As shown in Figure 14, if N is large (or small), then the width of the potential barrier becomes smaller (larger) and the QW channel becomes wider (smaller). The reason for taking $2N$ as its power is to always get the positive potential barrier when $\bar{V}_0$ is taken as a positive value. This kind of modulation is suitable for the narrow ballistic QW.

$$\overline{V}_0 \left[\cos\left(2\pi x/a\right)\right]^{2N}$$

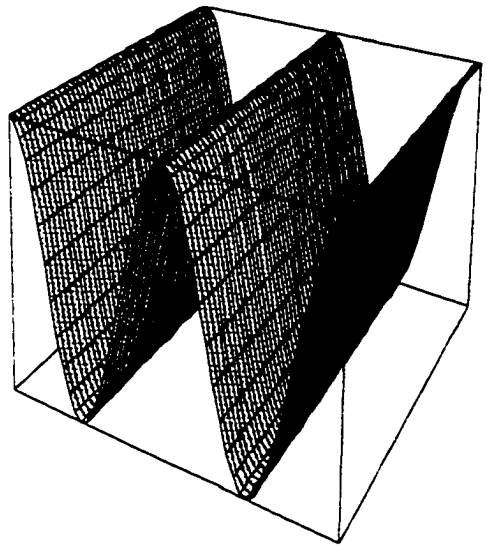

(a) $N = 1$

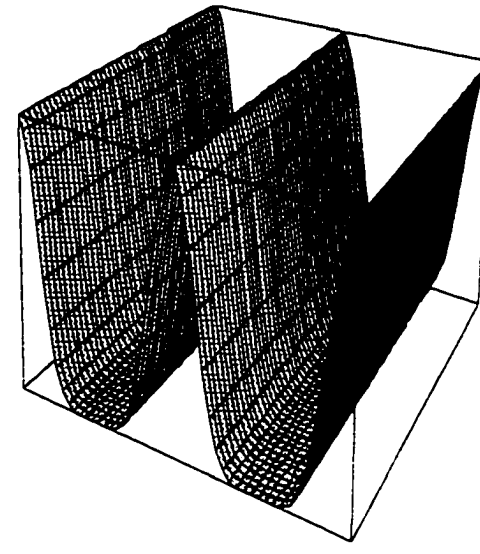

(b) $N = 3$

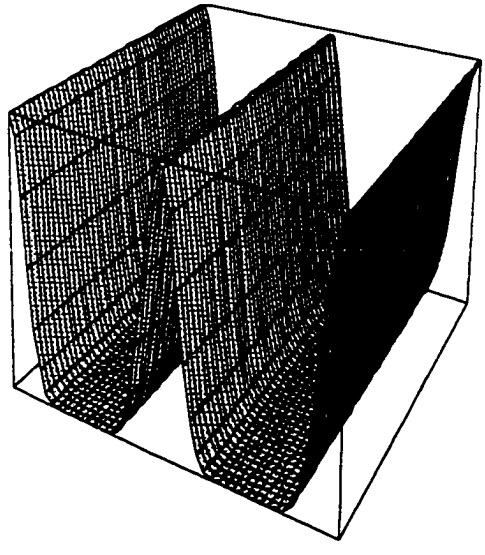

(c) $N = 5$

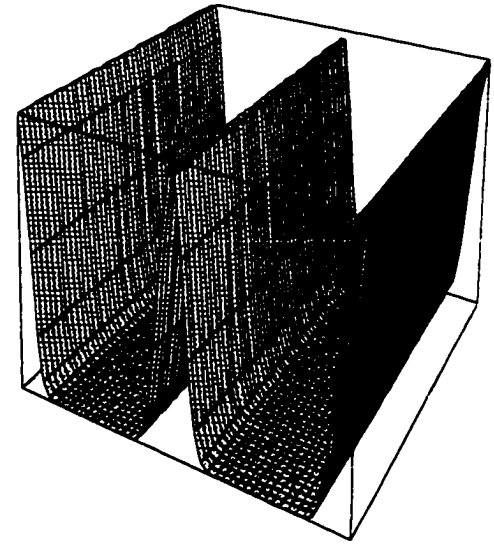

(d) $N = 10$

Figure 14: Quantum Wire Potential Barriers with N.

In the absence of impurities, the single-particle eigenfunctions are determined through

$$\psi_{j,X_0}(\mathbf{r}) = \sum_n C_n(j, X_0)\phi^{(0)}_{n,X_0}(\mathbf{r}) \ . \tag{16}$$

where

$$\phi^{(0)}_{n,X_0}(\mathbf{r}) = \frac{\exp\left[-i(X_0)y/l_H^2\right]}{\sqrt{L_y}}$$

$$\times \sqrt{\frac{1}{\pi^{1/2} l_H 2^n n!}} \exp\left[-(x - X_0)^2/2l_H^2\right] H_n\left(\frac{x - X_0}{l_H}\right) \ . \tag{17}$$

In Eqs. (16) and (17), $n = 0, 1, 2, \ldots$ is a Landau-level index and $H_n(x)$ is the nth order Hermite polynomial. Also, $L_y = N_y a$ is the sample length in the y direction. $X_0 = k_y l_H^2$ is the guiding center. $l_H = \sqrt{\hbar/eB}$ is the magnetic length and k_y is a wave vector along the y direction.

The expansion coefficients $C_n(j, X_0)$ in Eq. (16) are determined from the following matrix equation

$$\sum_n \left[\left(E_n^{(0)} - E_j(X_0)\right) \delta_{n,n'} + \frac{V_0}{a^2 \, l_H \pi^{1/2}} \sqrt{\frac{1}{2^{n+n'} n! n'!}} B_{n,n'}(X_0) \right] C_n(j, X_0) = 0 \ . \tag{18}$$

as well as the orthonormality condition:

$$\sum_n C_n^*(j, X_0) C_n(j', X_0') = \delta_{j,j'} \delta_{X_0, X_0'} \ .$$

From this calculation, we also obtain the secular equation which determines the energy eigenvalues $E_j(X_0)$

$$Det\left[\left(E_n^{(0)} - E_j(X_0)\right)\delta_{n,n'} + \frac{V_0}{a^2\, l_H \pi^{1/2}}\sqrt{\frac{1}{2^{n+n'} n! n'!}}\, B_{n,n'}(X_0)\right] = 0\ . \qquad (19)$$

Here, $E_n^{(0)} = (n + 1/2)\hbar\omega_c$ is the energy for the nth Landau level with eigenfunction $o_n^{(0)}(\mathbf{r})$ in the absence of scatterers and the matrix element $B_{n,n'}(X_0)$ appearing in Eqs. (18) and (19) is defined as follows and, for the potential in Eq. (15), we have

$$B_{n,n'}(X_0) \equiv \langle o^2_{n',X_0}{}^{(0)}(\mathbf{r})|U_L(\mathbf{x})|o^2_{n,X_0}{}^{(0)}(\mathbf{r})\rangle$$

$=$

$$\int_{-\infty}^{\infty} dx\ \exp\left[-\frac{(x - X_0)^2}{l_H^2}\right]$$
$$\times H_n\left(\frac{x - X_0}{l_H}\right) H_{n'}\left(\frac{x - X_0}{l_H}\right)\cos^{2N}(2\pi x/a)\ . \qquad (20)$$

By using $\hbar\omega_c$ as an energy scale, a as a length scale, and adopting periodic boundary conditions in the y direction so that $k_y = 2\pi L/a$ where $L = -N_y/2, \ldots, ((N_y/2) - 1)$ are integers, we obtain the dimensionless forms of the eigenfunctions in Eq. (16) as

$$\psi_{j,L}(\overline{\mathbf{r}}) = \sum_n C_n(j,\ L)\phi^{(0)}_{n,L/N_y}(\overline{\mathbf{r}})\ .$$

with

$$\phi^{(0)}_{n,L/N_y}(\overline{\mathbf{r}}) = \frac{\exp\left[-2\pi i\,(L/N_y)\,\overline{y}\right]}{\sqrt{N_y}}$$
$$\times\sqrt{\frac{2\pi^{1/2}\Phi}{2^n n!}}\exp\left[-\pi\Phi\left(\overline{x} - \frac{L/N_y}{\Phi}\right)^2\right] H_n\left[\sqrt{2\pi\Phi}\left(\overline{x} - \frac{L/N_y}{\Phi}\right)\right]\ , \qquad (21)$$

where the expansion coefficients are obtained from

$$\sum_n \left[\left(n + \frac{1}{2} - E_j(L) \right) \delta_{n,n'} + \frac{U_0}{\sqrt{\Phi}} \sqrt{\frac{1}{2^{n+n'} n! n'!}} B_{n,n'}(L) \right] C_n(j, L) = 0 \ . \quad (22)$$

and the matrix elements are given by

$$B_{n,n'}(L) = \int_{-\infty}^{\infty} d\bar{x} \ \exp\left[-\pi\Phi \left(\left(\bar{x} - \frac{L/N_y}{\Phi} \right)^2 + \left(\bar{x} - \frac{L/N_y}{\Phi} \right)^2 \right) \right]$$

$$\times H_n \left[\sqrt{2\pi\Phi} \left(\bar{x} - \frac{L/N_y}{\Phi} \right) \right] H_{n'} \left[\sqrt{2\pi\Phi} \left(\bar{x} - \frac{L/N_y}{\Phi} \right) \right] \cos^{2N}(2\pi\bar{x}) \ . \quad (23)$$

Here, $U_0 = m^* V_0 / \sqrt{2}\pi\hbar^2$. N_x is the number of unit cells in the x direction. $\bar{x} = x/a$. $\bar{y} = y/a$. The zero determinant of the coefficient matrix in Eq. (22) gives the energy eigenvalues $E_j(L)$. With these results, the eigenvalue spectra and wave-vector dispersion curves are presented.

4 Quantum Magnetotransport

4.1 General Theory for the Static, Nonlocal Conductivity

In quantum mechanics, the matrix elements of the current-density operator is given by

$$\mathbf{J}_{\beta,\alpha}(\mathbf{r}) = \frac{ie\hbar}{2m^*}\mathbf{W}_{\beta,\alpha}(\mathbf{r}) \ . \tag{24}$$

where

$$\mathbf{W}_{\beta,\alpha}(\mathbf{r}) = \psi^*_\beta(\mathbf{r})\ \overleftrightarrow{\mathbf{D}}_\mathbf{r}\ \psi_\alpha(\mathbf{r}) \equiv \psi^*_\beta(\mathbf{r})\mathbf{D}_\mathbf{r}\psi_\alpha(\mathbf{r}) - \psi_\alpha(\mathbf{r})\mathbf{D}^*_\mathbf{r}\psi^*_\beta(\mathbf{r}) \ . \tag{25}$$

Here, $\psi_\alpha(\mathbf{r})$ is an eigenfunction of the Hamiltonian in Eq. (1) and α, β are composite indices of the quantum numbers. In this notation, we have $\mathbf{D}_\mathbf{r} = (\nabla + ie\mathbf{A}(\mathbf{r})/\hbar)$. In the presence of an external perturbation, the Hamiltonian changes to $\mathcal{H} = \mathcal{H}_0 - eV(\mathbf{r}, t)$, where $V(\mathbf{r}, t) = V(\mathbf{r})\cos(\Omega t)\exp(-\eta|t|)$ with $\Omega \gg \eta = 0^-$, producing a longitudinal current. In linear response theory, the statistical current-density in the static ($\Omega = 0$) limit is calculated as [55]

$$\mathbf{J}_1(\mathbf{r}) = \frac{e^2\hbar^3}{4m^{*2}}\sum_{\alpha,\beta}\left[\frac{df_0(E_\alpha)}{dE}\delta(E_\beta - E_\alpha) + \frac{i}{\pi}\frac{f_0(E_\beta) - f_0(E_\alpha)}{E_\beta - E_\alpha}\mathcal{P}\left(\frac{1}{E_\beta - E_\alpha}\right)\right]$$
$$\times\left[\mathbf{W}_{\beta,\alpha}(\mathbf{r})\int d\mathbf{r}'\ \mathbf{W}_{\alpha,\beta}(\mathbf{r}')\bullet\mathbf{E}(\mathbf{r}')\right] \ . \tag{26}$$

In Eq. (26), $\mathbf{E}(\mathbf{r}) = -\nabla V(\mathbf{r})$ is an external perturbation electric field, $f_0(E - E_\mathrm{F}) = [1 + \exp[(E - E_\mathrm{F})/k_\mathrm{B}T]]^{-1}$ is the Fermi distribution function for a system

in equilibrium. E_α are the energy eigenvalues. E_F is the Fermi energy and $\mathcal{P}$ means that only the principal part is taken. Making use of the nonlocal form of Ohm's law

$$\mathbf{J}_1(\mathbf{r}) = \int_A d\mathbf{r}' \ \overleftrightarrow{\sigma}\ (\mathbf{r},\ \mathbf{r}') \bullet \mathbf{E}(\mathbf{r}') \ . \tag{27}$$

we obtain the electric-field response matrix

$$\sigma_{i,j}(\mathbf{r},\ \mathbf{r}') = \frac{\pi e^2\hbar^3}{4m^{*2}} \sum_{\alpha,\beta} \left[\frac{df_0(E_\alpha)}{dE}\delta(E_\beta - E_\alpha) + \frac{i}{\pi}\frac{f_0(E_\beta) - f_0(E_\alpha)}{E_\beta - E_\alpha}\mathcal{P}\left(\frac{1}{E_\beta - E_\alpha}\right)\right]$$

$$\times \left[\Pi^{i}_{\beta,\alpha}(\mathbf{r})\Pi^{j}_{\alpha,\beta}(\mathbf{r}')\right] \ . \tag{28}$$

which satisfies the Onsager relations [55]. The second term in Eq. (28) is zero when $B = 0$, but the time-reversal symmetry is broken when $B \neq 0$. From the definition of the single-particle Green's function and Eq. (25), we rewrite Eq. (28) as

$$\sigma_{i,j}(\mathbf{r},\ \mathbf{r}') = \frac{e^2\hbar^3}{8\pi m^{*2}} \int_{-\infty}^{\infty} dE \ \left[\left(-\frac{df_0(E)}{dE}\right) G^-_E(\mathbf{r},\ \mathbf{r}')\ \overrightarrow{D}^{*i}_{\mathbf{r}}\overrightarrow{D}^{j}_{\mathbf{r}'}\ G^-_E(\mathbf{r}',\ \mathbf{r})\right.$$

$$\left. -f_0(E)\left(\frac{dG^-_E(\mathbf{r},\ \mathbf{r}')}{dE}\ \overrightarrow{D}^{*i}_{\mathbf{r}}\overrightarrow{D}^{j}_{\mathbf{r}'}\ G^-_E(\mathbf{r}',\ \mathbf{r}) + G^-_E(\mathbf{r},\ \mathbf{r}')\ \overrightarrow{D}^{*i}_{\mathbf{r}}\overrightarrow{D}^{j}_{\mathbf{r}'}\ \frac{dG^-_E(\mathbf{r}',\ \mathbf{r})}{dE}\right)\right] \ , \tag{29}$$

where $G^\mp_E$ are the advanced $(+)$ and retarded $(-)$ Green's functions, respectively, defined by

$$G^\pm_E(\mathbf{r},\mathbf{r}') = \sum_\alpha \frac{\psi_\alpha(\mathbf{r})\psi^*_\alpha(\mathbf{r}')}{E - E_\alpha \pm i0^+} \ .$$

Here, $\psi_\alpha(\mathbf{r})$ is the electron wave function. The first term in Eq. (29) is evaluated near the Fermi surface, while the second term includes contributions from all occupied states. Since single-particle Green's functions are gauge-independent *i.e.* only the magnetic field $\mathbf{B}$ is involved. Eq. (29) is also gauge-independent.

4.2 Averaged Conductivity

By neglecting the small effects from the current and voltage leads connected to the array, we may take the external electric field as uniform over the whole array. This is justified since the size of a sample used in an experiment is very small compared with the scale over which the electric field varies. By averaging the response matrix in Eq. (29) over the whole array, we obtain the averaged static conductivity for this system as

$$\sigma_{i,j}(\Omega = 0) = -\frac{e^2\hbar^3}{8\pi m^{*2}\mathcal{A}} \int_{\mathcal{A}} d\mathbf{r} \int_{\mathcal{A}} d\mathbf{r}' \int_{-\infty}^{\infty} dE\ f_0(E)$$

$$\times \left[\frac{dG_E^-(\mathbf{r},\ \mathbf{r}')}{dE}\ \vec{D}_{\mathbf{r}}^{*i}\vec{D}_{\mathbf{r}'}^{j}\ \Delta G_E(\mathbf{r}',\ \mathbf{r}) - \Delta G_E(\mathbf{r},\ \mathbf{r}')\ \vec{D}_{\mathbf{r}}^{*i}\vec{D}_{\mathbf{r}'}^{j}\ \frac{dG_E^-(\mathbf{r}',\ \mathbf{r})}{dE} \right] . \quad (30)$$

where $\Delta G_E = G_E^- - G_E^-$. The result in Eq. (30) can also be obtained directly from Kubo's formula [56, 57]. We do our calculations in the zero temperature ($T = 0$) limit since we are not interested in effects arising at finite temperature. Furthermore, the experiments of Weiss, et al. [18] were carried out at very low temperature.

Using Eq. (30), we obtain analytic results for the QMT coefficients.

$$\sigma_{xx}^{(0)}(0) = \frac{2\pi e^2\hbar^3 N_y \Phi}{m^{*2}\mathcal{A}} \sum_{j,\,j'} \int_{-Gl_H^2/2}^{Gl_H^2/2} \frac{dX_0}{a} \left(F^{(2)}_{j,X_0;j',X_0}\right)^2$$

$$\times \int_{-\infty}^{\infty} dE\; D_{j,X_0}(E) D_{j',X_0}(E) \left[-\frac{df_0(E)}{dE}\right] . \qquad (31)$$

$$\sigma_{xy}^{(0)}(0) = -\frac{4e^2\hbar^3 N_y \Phi}{m^{*2}\mathcal{A}} \sum_{j,\,j'}{}' \int_{-Gl_H^2/2}^{Gl_H^2/2} \frac{dX_0}{a} \frac{1}{[E_j(X_0) - E_{j'}(X_0)]^2}$$

$$\times \left[\frac{1}{l_H^2} F^{(1)}_{j,X_0;j',X_0} F^{(2)}_{j',X_0;j,X_0} + F^{(3)}_{j,X_0;j',X_0} F^{(2)}_{j',X_0;j,X_0}\right] \int_{-\infty}^{\infty} dE\; D_{j,X_0}(E) f_0(E) . \qquad (32)$$

In Eq. (32), there is a correction to the result $n_{2D}e/B$ in the absence of scatterers, where n_{2D} is the electron density. Furthermore, the band part Hall conductivity satisfies $\sigma_{yx}^{(0)}(0) = -\sigma_{xy}^{(0)}(0)$. In Eq. (32), the summation with prime means that all terms with $E_j(X_0) = E_{j'}(X_0)$ must be excluded.

$$\sigma_{yy}^{(0)}(0) = \frac{2\pi e^2\hbar^3 N_y \Phi}{m^{*2}\mathcal{A}} \sum_{j,\,j'} \int_{-Gl_H^2/2}^{Gl_H^2/2} \frac{dX_0}{a}$$

$$\times \left[\frac{1}{L_H^4}\left(F^{(2)}_{j,X_0;j',X_0}\right)^2 + \frac{2}{L_H^2} F^{(1)}_{j,X_0;j',X_0} F^{(3)}_{j,X_0;j',X_0} + \left(F^{(3)}_{j,X_0;j',X_0}\right)^2\right]$$

$$\times \int_{-\infty}^{\infty} dE\; D_{j,X_0}(E) D_{j',X_0}(E) \left[-\frac{df_0(E)}{dE}\right] . \qquad (33)$$

Furthermore, in Eq. (31) - (33), we have defined

$$D_{j,X_0}(E) = \delta\left[E - E_j(X_0)\right] , \qquad (34)$$

as the partial density-of-states as well as the following structure factors

2D modulation

$$F^{(1)}_{j,X_0;j',X_0} = F^{(1)}_{j',X_0;j,X_0} = \int_{\mathcal{A}} d\mathbf{r}\ \psi^*_{j,X_0}(\mathbf{r}) x \psi_{j',X_0}(\mathbf{r})$$

$$= \frac{l_{\mathrm{H}}}{\sqrt{2}} \sum_{n,m} C_{n,m}(j,\ X_0) \left[\sqrt{n+1} C_{n-1,m}(j',\ X_0) + \sqrt{n} C_{n-1,m}(j',\ X_0) \right] . \qquad (35)$$

$$F^{(2)}_{j,X_0;j',X_0} = -F^{(2)}_{j',X_0;j,X_0} = \int_{\mathcal{A}} d\mathbf{r}\ \psi^*_{j,X_0}(\mathbf{r}) \frac{\partial}{\partial x} \psi_{j',X_0}(\mathbf{r})$$

$$= \frac{1}{\sqrt{2} l_{\mathrm{H}}} \sum_{n,m} C_{n,m}(j,\ X_0) \left[\sqrt{n+1} C_{n-1,m}(j',\ X_0) - \sqrt{n} C_{n-1,m}(j',\ X_0) \right] . \qquad (36)$$

$$F^{(3)}_{j,X_0;j',X_0} = F^{(3)}_{j',X_0;j,X_0} = -i \int_{\mathcal{A}} d\mathbf{r}\ \psi^*_{j,X_0}(\mathbf{r}) \frac{\partial}{\partial y} \psi_{j',X_0}(\mathbf{r})$$

$$= -G \sum_{n,m} m C_{n,m}(j,\ X_0) C_{n,m}(j',\ X_0) - \frac{X_0}{l_{\mathrm{H}}^2} \delta_{j,j'} . \qquad (37)$$

1D modulation

$$F^{(1)}_{j,X_0;j',X_0} = F^{(1)}_{j',X_0;j,X_0} = \int_{\mathcal{A}} d\mathbf{r}\ \psi^*_{j,X_0}(\mathbf{r}) x \psi_{j',X_0}(\mathbf{r})$$

$$= \frac{l_{\mathrm{H}}}{\sqrt{2}} \sum_{n} C_{n}(j,\ X_0) \left[\sqrt{n+1} C_{n-1}(j',\ X_0) + \sqrt{n} C_{n-1}(j',\ X_0) \right] . \qquad (38)$$

$$F^{(2)}_{j,X_0;j',X_0} = -F^{(2)}_{j',X_0;j,X_0} = \int_{\mathcal{A}} d\mathbf{r}\ \psi^*_{j,X_0}(\mathbf{r}) \frac{\partial}{\partial x} \psi_{j',X_0}(\mathbf{r})$$

$$= \frac{1}{\sqrt{2} l_{\mathrm{H}}} \sum_{n} C_{n}(j,\ X_0) \left[\sqrt{n+1} C_{n-1}(j',\ X_0) - \sqrt{n} C_{n-1}(j',\ X_0) \right] , \qquad (39)$$

$$F^{(3)}_{j,X_0;j',X_0} = F^{(3)}_{j',X_0;j,X_0} = -i \int_{\mathcal{A}} d\mathbf{r}\ \psi^*_{j,X_0}(\mathbf{r}) \frac{\partial}{\partial y} \psi_{j',X_0}(\mathbf{r})$$

$$= -\frac{X_0}{l_{\mathrm{H}}^2} \delta_{j,j'} . \qquad (40)$$

4.3 Dimensionless Forms of conductivity matrix elements

Based on Eqs. (11) - (13). we can drive the dimensionless forms of the matrix elements of the conductivity in Eqs. (31) - (32) in units of (e^2/h) at zero temperature.

$$\sigma_{xx}^{(0)}(0) = \frac{\pi}{N_x N_y \Phi} \sum_{j,\, j'} \sum_{L=-N_y/2}^{(N_y/2)-1} \left(F_{j,j'}^{(2)}(L)\right)^2 \Big|_{E_j(L)=E_{j'}(L)=E_F} \tag{41}$$

$$\sigma_{yx}^{(0)}(0) = -\frac{2}{N_x N_y \Phi} \sum_{j,\, j'}{}' \sum_{L=-N_y/2}^{(N_y/2)-1} \frac{1}{[E_j(L) - E_{j'}(L)]^2}$$

$$\times \left[F_{j,j'}^{(1)}(L) F_{j',j}^{(2)}(L) + 2\sqrt{\frac{\pi}{\Phi}} F_{j,j'}^{(3)}(L) F_{j',j}^{(2)}(L)\right]\Big|_{E_j(L) \le E_F} \tag{42}$$

In the absence of scatterers. Eq.(42) reduces to the well-known result $\sigma_{yx}^{(0)}(0) = n_{2D}e/B$.[21] where $2\sum_j \theta(E_F - E_j(L)) = N_x\Phi(2\pi L_H^2 n_{2D})$.

$$\sigma_{yy}^{(0)}(0) = \frac{\pi}{N_x N_y \Phi} \sum_{j,\, j'} \sum_{L=-N_y/2}^{(N_y/2)-1}$$

$$\times \left[\left|F_{j,j'}^{(1)}(L)\right|^2 + 4\sqrt{\frac{\pi}{\Phi}} F_{j,j'}^{(1)}(L) F_{j,j'}^{(3)}(L) + \frac{4\pi}{\Phi}\left|F_{j,j'}^{(3)}(L)\right|^2\right]\Big|_{E_j(L)=E_{j'}(L)=E_F} \tag{43}$$

Here, the partial density-of-states as well as the structure factors determining the group velocities are given by

$$D_{j,L}(E) = \frac{1}{\sqrt{2\pi}\gamma_0} \exp\left[-\frac{(E - E_j(L))^2}{2\gamma_0^2}\right] \tag{44}$$

2D modulation

$$F^{(1)}_{j,j'}(L) = \sum_{n,m} C_{n,m}(j,\ L) \times \left[\sqrt{n+1}C_{n-1,m}(j',\ L) + \sqrt{n}C_{n-1,m}(j',\ L)\right] \quad (45)$$

$$F^{(2)}_{j,j'}(L) = \sum_{n,m} C_{n,m}(j,\ L) \times \left[\sqrt{n+1}C_{n-1,m}(j',\ L) - \sqrt{n}C_{n-1,m}(j',\ L)\right] \quad (46)$$

$$F^{(3)}_{j,j'}(L) = -\sum_{n,m} mC_{n,m}(j,\ L)C_{n,m}(j',\ L) - \frac{L}{N_y}\delta_{j,j'} \quad (47)$$

$$n(\mathbf{r}) = \sum_{j,L} |\psi_{j,L}(\mathbf{r})|^2 \,|_{E_j(L)\le E_F} \,. \quad (48)$$

1D modulation

$$F^{(1)}_{j,j'}(L) = \sum_{n} C_n(j,\ L) \times \left[\sqrt{n+1}C_{n-1}(j',\ L) + \sqrt{n}C_{n-1}(j',\ L)\right] \quad (49)$$

$$F^{(2)}_{j,j'}(L) = \sum_{n} C_n(j,\ L) \times \left[\sqrt{n+1}C_{n-1}(j',\ L) - \sqrt{n}C_{n-1}(j',\ L)\right] \quad (50)$$

$$F^{(3)}_{j,j'}(L) = -\frac{L}{N_y}\delta_{j,j'} \quad (51)$$

$$n(\mathbf{r}) = \sum_{j,L} |\psi_{j,L}(\mathbf{r})|^2 \,|_{E_j(L)\le E_F} \,. \quad (52)$$

4.4 Resistivity Matrix Elements

From the inverse of the conductivity matrix in Eqs. (31) - (32), we generally obtain the elements of resistivity matrix

$$\rho_{xx}^{(0)}(0) = \frac{\sigma_{yy}^{(0)}(0)}{\sigma_{yy}^{(0)}(0)\sigma_{xx}^{(0)}(0) + [\sigma_{yx}^{(0)}(0)]^2} . \tag{53}$$

$$\rho_{xy}^{(0)}(0) = -\rho_{yx}^{(0)}(0) = \frac{\sigma_{yx}^{(0)}(0)}{\sigma_{yy}^{(0)}(0)\sigma_{xx}^{(0)}(0) + [\sigma_{yx}^{(0)}(0)]^2} . \tag{54}$$

$$\rho_{yy}^{(0)}(0) = \frac{\sigma_{xx}^{(0)}(0)}{\sigma_{yy}^{(0)}(0)\sigma_{xx}^{(0)}(0) + [\sigma_{yx}^{(0)}(0)]^2} . \tag{55}$$

5 Numerical Results of QMT Coefficients for 2D Modulation

In this section, we used the equations for the 2D modulation defined in section 4.3 to calculate QMT coefficients. Since x and y direction are symmetry each other.

$$\sigma_{xx}^{(0)} = \sigma_{yy}^{(0)} \tag{56}$$

$$\sigma_{yx}^{(0)} = -\sigma_{xy}^{(0)} \tag{57}$$

Accordingly, the resistivity coefficients become

$$\rho_{xx}^{(0)}(0) = \rho_{yy}^{(0)}(0) = \frac{\sigma_{xx}^{(0)}(0)}{[\sigma_{xx}^{(0)}(0)]^2 + [\sigma_{yx}^{(0)}(0)]^2} . \tag{58}$$

$$\rho_{xy}^{(0)}(0) = -\rho_{yx}^{(0)}(0) = \frac{\sigma_{yx}^{(0)}(0)}{[\sigma_{xx}^{(0)}(0)]^2 + [\sigma_{yx}^{(0)}(0)]^2} . \tag{59}$$

In our numerical calculations, we take $|m| \leq M$ and $0 \leq n \leq N_L$, where $M = (N_x\Phi - 1)/2$ and $N_L = 2\text{Int}\ (E_F/\hbar\omega_c)$. In each Landau band, we have N_y Bloch states in the first Brillouin zone. Therefore, there are $N_xN_y\Phi$ states in each Landau band. After we order all the energy levels by magnitude, the Fermi energy can be determined by simply counting the energy levels, *i.e.* the N_Fth

level is the Fermi energy, where $N_F = N_x N_y n_{2D} a^2/2$. From the eigenfunctions in Eq. (11), we can calculate the electron density distribution within the modulated 2DEG at $T = 0$ K.

5.1 Longitudinal Conductivities

5.1.1 Dependence of the Longitudinal Conductivities on N

Anti-dot regime Fig. 15 (a), (b), and (c) show our numerical results for the longitudinal conductivities $\left(\sigma_{xx}^{(0)}\right)$ for the antidot scatterers with various size when N is varied. Fig. 15 (a) is the results for the low modulation case ($U_0 = 1.235$). Shown in this figure is that all intensitieis are not appreciably changed by the different scatterer size (N). From the Eq.(31) and (41), we can see that the longitudinal conductivities $\left(\sigma_{xx}^{(0)}\right)$ are contributed by the electron states near the Fermi level. In this low modulation regime, the Fermi level energy ($\sim 0.259meV$) is higher than the strength of the sctterers ($0.156meV$).(Table 3)

Table 3: Comparison of U_0 with $\overline{V}_0$ for $a = 200nm$ in 2D modulation

U_0	$\overline{V}_0(meV)$
1.235	0.156
2	0.253
3	0.380
4	0.506
10	1.265
100	12.65

where, $\overline{V}_0 = (2^{1/2}\pi\hbar^2)U_0/m^*a^2$.

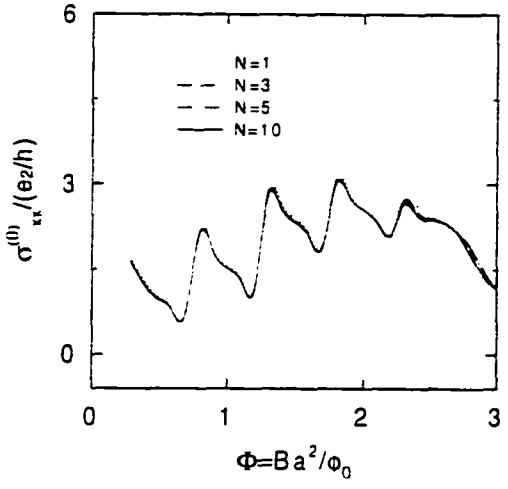

(a) $U_0 = 1.235$

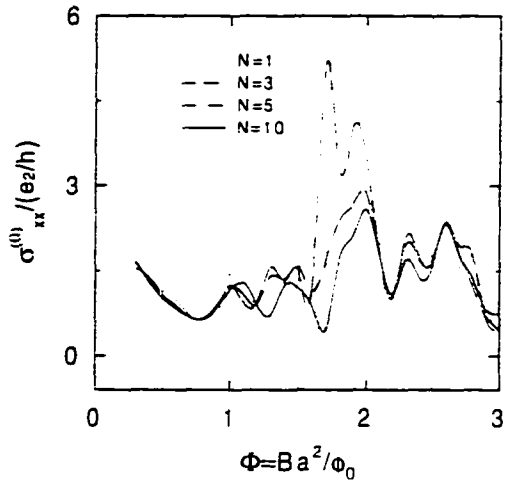

(b) $U_0 = 10$

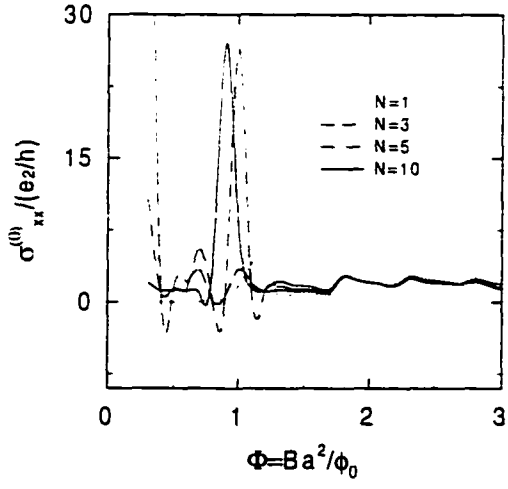

(c) $U_0 = 100$

Figure 15: Longitudinal conductivities $\sigma^{(0)}_{xx}/(e^2/h)$ vs. $\Phi = Ba^2/\phi_0$ for the various size of the scatterers. $N_x = N_y = 4$, $n = 3$, $n_{2D}a^2 = 0.5$, and $a = 200nm$.

So. the electron states near the Fermi level can't see the change of the scatterer size. That is why all intensitieis are not appreciably changed by the different scatterer size (N). Shown in this figure (a). secondly. is that there are several oscillations as Φ increases. These oscillations are related to the density of states for the LL subbands. As mentioned above. since the Fermi energy is given by $N_F = N_x N_y n_{2D} a^2/2$. the Fermi energy can be determined by counting the ordered eigenvalues. In this figure. the Fermi energy is in the $n = 3$ band for $0.3 \leq \Phi \leq 0.7$. $n = 1$ for $0.8 \leq \Phi \leq 1.2$. and $n = 0$ for $1.3 \leq \Phi \leq 3.0$.(Table 4)

Table 4: Comparison of LL with Fermi level for Φ in 2D AD modulation

Φ	m	$2m+1$	no. of states	Fermi Level
$0.3 \sim 0.7$	0	1	4	$n = 3$
$0.8 \sim 1.2$	1	3	12	$n = 1$
$1.3 \sim 1.7$	2	5	20	$n = 0$
$1.8 \sim 2.2$	3	7	28	$n = 0$
$2.3 \sim 2.7$	4	9	36	$n = 0$
$2.8 \sim 3.0$	5	11	44	$n = 0$

where. $\Phi = Ba^2/\phi_0$, $m = Intof(N_x\Phi - 1)/2$, No. of states= $(n+1)(2m+1)$. Fermi level $N_F = N_x N_y n_{2D} a^2/2 = 4$ when $N_x = N_y = 4$, $n = 3$, and $n_{2D}a^2 = 0.5$.

As Φ is increased, the occupied states are increased by $M = (N_x\Phi - 1)/2$. For certain values of Φ, M is not changed until it gets the next available integer. Consider the case when $N_x = N_y = 4$ and $\Phi = 0.3$. Here, $M = 0$ because M has

to be an integer. So, each LL per each N_y Bloch state has only one state since there are $2M+1$ states for each LL per each N_y Bloch state. Again, consider the case when $N_x = 4$ and $\Phi = 0.7$. Still $M = 0$ and each LL has only one state. So if $n = 3$, then there are only four states in this system because there is a total of $(n+1)(2M+1)$ states. When $N_y = 4$ (for the square lattice), the Fermi energy is in the fourth energy level for $n_{2D}a^2 = 0.5$. Since, for the range $0.3 \leq \Phi \leq 0.7$, there are four states, the Fermi level is in the $n = 3$ level. However, since the LL is given by $(n+1/2)\hbar\omega_c$, where $\omega_c = eB/m^*$, if Φ is increased in this range, the energy difference between LLs is increased. Accordingly, the density of states per unit energy is decreased. In addition to this, the fourth energy state for $\Phi = 0.7$ is higher than when $\Phi = 0.3$ because the energy difference between LLs for $\Phi = 0.7$ is larger than for $\Phi = 0.3$. If the energy is higher, then the orbit for the electron is larger, so this larger orbit is more likely scattered by the modulated potential. Therefore, for the range $0.3 \leq \Phi \leq 0.7$, the magnitude of the conductivities is reduced when Φ is increased in this range. Next, if $\Phi = 0.8$, then $M = 1$ and there are three states in each LL because there are $2M+1$ states in each LL per each N_y Bloch state. For the same size of the sample as above ($N_x = 4$, $N_y = 4$ and $n_{2D}a^2 = 0.5$), the Fermi energy is still in the fourth energy level but the energy states of the LLs are changed since each LL has three states. Consequently, for $\Phi > 0.8$, the Fermi level is located in the $n = 1$ state because each LL has three states, so the $n = 0$ and $n = 1$ states have three states, etc.,

respectively. Therefore, the fourth state is to be in the $n = 1$ state. As a result, the Fermi level is changed from $n = 3$ to $n = 1$. The orbit in the $n = 1$ state is smaller than for $n = 3$. This smaller orbit makes the larger intensity of $\sigma_{xx}^{(0)}$ at $\Phi = 0.8$, etc. With this manner, $\sigma_{xx}^{(0)}$ oscillates. Here, the Fermi energy is at the $n = 3$ level up to $\Phi = 0.7$, the $n = 1$ level up to $\Phi = 1.2$, and the $n = 0$ level up to $\Phi = 3.0$; N is increased by the period of $\Delta\Phi = 0.5$. Fig. 15 (a) shows that the $\sigma_{xx}^{(0)}$ peaks are at $\Phi = 0.8$, 1.3, 1.8, 2.3, respectively. The peak positions are exactly matched with $\Delta\Phi = 0.5$. Thus we conclude that these oscillations are related to the density of states. And, in this low modulation case, the effect due to the density of states is more dominant than the one due to the scattering. The third one observed in Fig. 15 (a) is the ocsillation amplitude. The oscillation amplitude is increased or decreased when N is increased. At low magnetic fields ($\Phi < 0.7$), the magnitude of $\sigma_{xx}^{(0)}$ is slightly decreased as N is increased. (Fig. 16 (a)) In the peak at $\Phi = 0.8$, the opposite effect occurs, that is, the peak of $\sigma_{xx}^{(0)}$ is slightly increased as N is increased. However in the other peak, the intensity of $\sigma_{xx}^{(0)}$ is slightly decreased again as N is increased. (Fig. 16 (b)) It is guessed that this is due to the competition of the orbit size and the scatterering effect. At low magnetic fields, the radius of a Landau orbit for an electron with energy near the Fermi level is relatively large. If its diameter is larger than the spacing between scatterers, then the orbit is not closed since an electron is more likely to be scattered.

Detailed Longitudinal Conductivities with N for the Anti-dot

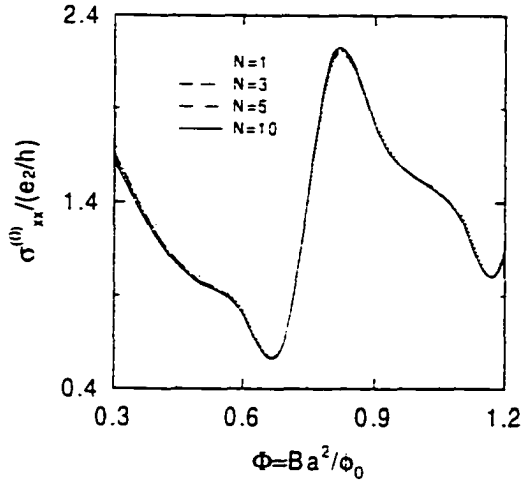

(a) at $\Phi = 0.8$

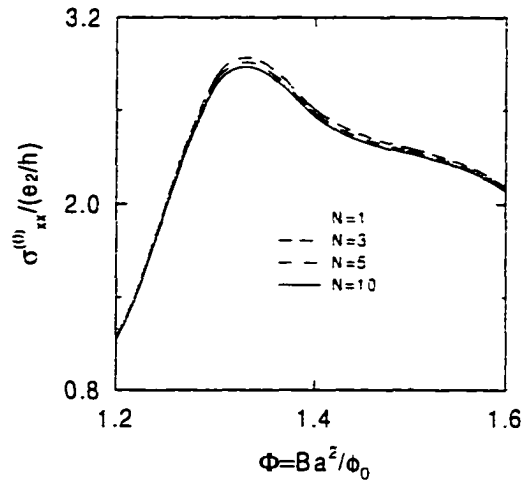

(b) at $\Phi = 1.3$

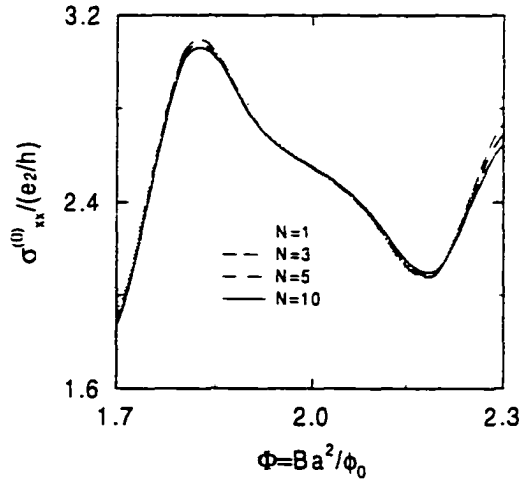

(c) at $\Phi = 1.8$

Figure 16: Detailed Longitudinal conductivities $\sigma^{(0)}_{xx}/(e^2/h)$ vs. $\Phi = Ba^2/\varphi_0$ for $U_0 = 1.235$. $N_x = N_y = 4$, $n = 3$, $n_{2D}a^2 = 0.5$, and $a = 200nm$.

When the magnetic field increases. the Landau orbit becomes smaller and is less likely scattered by the potential. So these electrons are more likely to contribute to $\sigma_{xx}^{(0)}$. On the other hand. the smaller orbits make a smaller contribution to $\sigma_{xx}^{(0)}$. Therefore. the size of the orbit and the scatterering effect are competitive. Theses competitions make the different amplitudes when N is increased as shown in Fig. 16 (a) and (b). Fig. 15 (b) is the result for the intermediate modulation which is slightly larger than the Fermi level energy.($U_0 = 10$) In this regime. we can still observe the oscillations due to the density of states when N is increased. Because the electron can have more space between the scatterers and it behaves as if it is in the normal 2DEG. When $N = 1$. the intensities are appreciably changed. Because the size of the scatterer is larger than the others and it makes the big scattering. This big scattering can make the forward or backward scattering. In our case. at around $\Phi = 2$. there is the enhanced forward scattering. So. the intensity is much bigger than th eothers. This enhanced forward scattering is reduced when N is increased. Anyway. the intensities are appreciably changed when the scattere size is changed because the electronic states near the Fermi level can experience the change of the scatterer size. However. this oscillatory behaviour is completely disappeared in the strong modulation case. Fig. 15 (c) shows the result for the strong modulation case.($U_0 = 100$) At low magnetic fields, in this figure, the oscillatory behaviour due to the density of states is completely replaced by the resonant peaks due to the scattering effect

with the scatterers. It reflects that the scattering effect due to the large orbit at the low magnetic fields in the strong modulation case is dominat rather than the ocillatory behaviour due to the density of states. On the other hand, at high magnetic fields, the oscillatory behaviour is still observed. Because, at high magnetice fields, the electron orbit is small and the scattering effect is reduced. Therfore we can know, in this strong modulation case, that the scattering effect by the scatterers is more dominat than the one due to the density of states.

Quantum-dot regime Fig. 17 (a), (b), and (c) are the numerical results for the quantum dot regime with the various size of the dots when N is varied. The scattering mechanism is basically different from the one for the anti-dot case. In quantum dot case, the main interaction with the dot is the one captured by the dot, instead of scattering off the scatteres in the anti-dot case. Nevertheless, in the low modulation case ($U_0 = -1.235$), all the features are almost same as the ones observed in the anti-dot case. (Fig. 17 (a) and Fig. 15 (a)) In Fig. 17 (a), all the intensities are not sensitive for the change of the dot size because the Fermi level energy, in this low modulation case, can overcome the capturing strength of the dot. And the oscillatory behaviour due to the density of states is also observed with the same period of $\Delta\Phi = 0.5$ as in the anti-dot case. (Fig. 17 (b) shows the results for the intermediate dot modulation ($U_0 = -10$). In this modulation, the Fermi level energy is compatible with the capturing strength of the dot. The intensities start to be modified by the capturing effect of the dot.

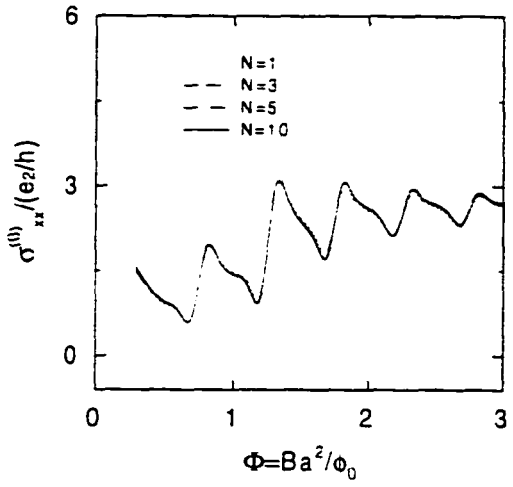

(a) $U_0 = -1.235$

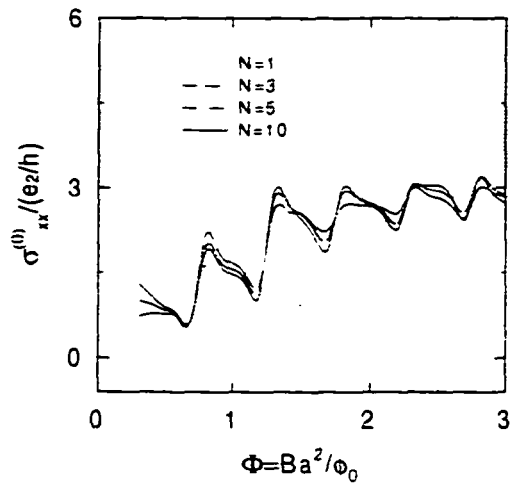

(b) $U_0 = -10$

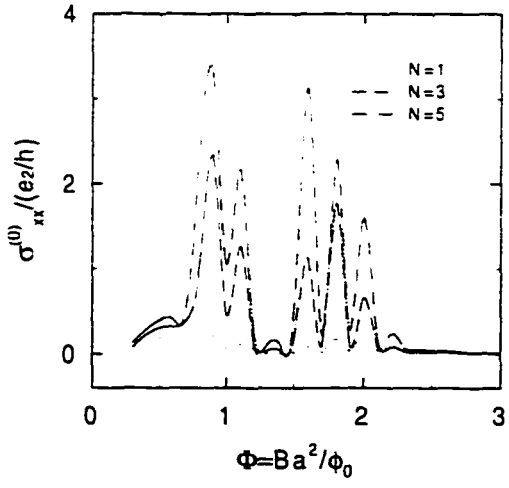

(c) $U_0 = -100$

Figure 17: Longitudinal conductivities $\sigma^{(0)}_{xx}/(e^2/h)$ vs. $\Phi = Ba^2/\phi_0$ for the various size of the dots. $N_x = N_y = 4$, $n = 3$, $n_{2D}a^2 = 0.5$, and $a = 200nm$.

When N is increased, the intensities of some parts are increased and the other parts are decreased due to the competiton between the size of the orbit and the capturing effect of the dot as in the anti-dot case. However, the oscillatory behaviour due to the density of states is still observed. When $n = 1$, the capturing effect by the dot is dominant and thus the oscillatory behaviour is appreciably modified. This oscillatory behaviour is disappeared in the strong dot-modulation. Fig. 17 (c) is the results for the strong modulation case ($U_0 = -100$). In this case, the oscillations with the period of $\Delta\Phi = 0.5$ is completely disappeared because the capturing strength($\sim 12.7meV$) of the dot potential is much larger than the Fermi level energy ($\sim 0.259meV$) and so, the capturing effect is much more dominant than the effect due to the density of states. In our case, when N is increased, the intensities are increased. This is because the electron has more free space between the dots. Another one is that, in the quantum dot regime, when the magnetic field becomes large enough, the Landau orbit of the electron becomes very small so that the orbit of the electron is smaller than the the size of the dot. In this case, the electron can be bound within the dots. Actually our numerical calculations show that the range of the cyclotron radii for large magnetic fields vary approximately from 50nm to 100nm.(Table 1 This range is about the experimental quantum dot size. So it is possible for the electron to be bound to the dot at high magnetic fields. This makes the amplitude of $\sigma_{xx}^{(0)}$ small.

5.1.2 Dependence of the Longitudinal Conductivities on U_0

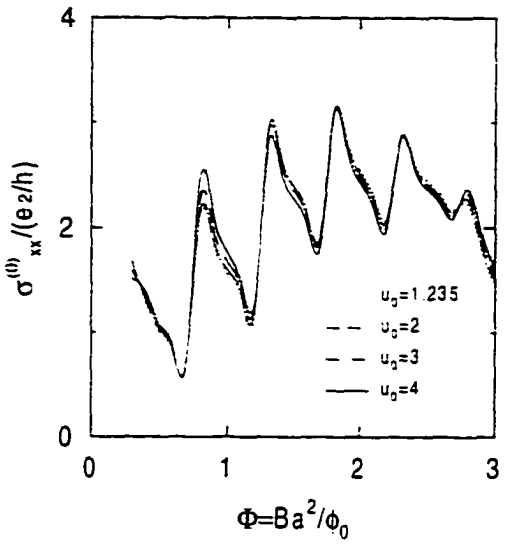

Figure 18: Longitudinal conductivities $\sigma^{(0)}_{xx}/(e^2/h)$ vs. $\Phi = Ba^2/\phi_0$ for the various strength of the scatterers. $N_x = N_y = 4$. $n = 3$. $n_{2D}a^2 = 0.5$. and $a = 200nm$.

Anti-dot regime Fig. 18 shows the longitudinal conductivities $\sigma^{(0)}_{xx}$ with U_0 for the AD regime. In our case. for $a = 200$ nm and $U_0 = 1.235.\ 2.\ 3.\ 4.\ 10.$ $V_0 =$ 0.156. 0.253. 0.380. 0.506. and 1.265 meV. respectively and the Fermi level energy is $\sim 0.259meV$. (Table 3) So, the strength of the scatterer is compatible with the Fermi level energy. Accordingly, the oscillatory behaviour is still observed as in Fig. 15 (a). But the intensities are appreciably changed with U_0. In general, if U_0 is increased, then the scattering by the scatterer is more and so the electrons have less contribution to $\sigma^{(0)}_{xx}$. These phenomena occur at high magnetic fields in Fig. 18. At low magnetic fields, this effect is reversed. At around $\Phi = 0.8$,

the intensities of $\sigma_{xx}^{(0)}$ are increased when U_0 is increased. This is due to the scattering by the electron with the large orbit at low magnetic fields. In this case, the forward scattering is enhanced by the scatterers. This phenomenon also appears in quantum-dot regime.

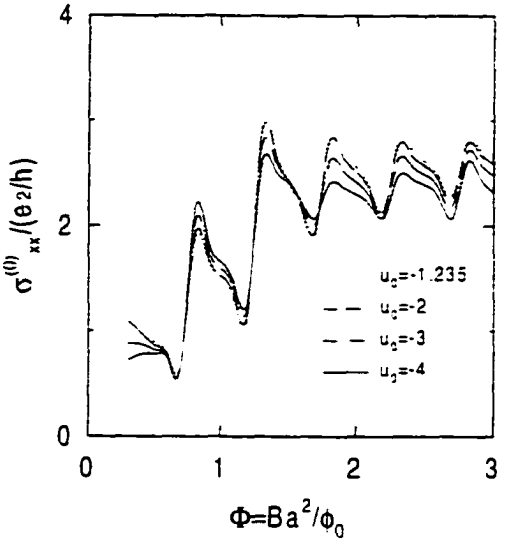

Figure 19: Longitudinal conductivities $\sigma_{xx}^{(0)}/(e^2/h)$ vs. $\Phi = Ba^2/\phi_0$ for the various strength of the dots. $N_x = N_y = 4$. $n = 3$, $n_{2D}a^2 = 0.5$, and $a = 200nm$.

Quantum-dot regime Fig. 19 shows the longitudinal conductivities $\sigma_{xx}^{(0)}$ with U_0 for the quantum-dot regime. The oscillatory behaviour is still observed as in Fig. 17 (a). As in the anti-dot case, the intensities are appreciably changed with U_0. If U_0 is negatively increased, then the capturing effect by the dot is increased and so the electrons have less contribution to $\sigma_{xx}^{(0)}$. This phenomenon is obviously observed at high magnetic fields in Fig. 19. However, at low magnetic

fields. this effect is reversed. At around $\Phi = 0.8$, the intensities of $\sigma_{xx}^{(0)}$ are increased when U_0 is negatively increased. This is due to the interation between the quantum-dot and the electron with the large orbit at low magnetic fields. As seen in the Fig. 9. the eigenvalues are negative below $\Phi = 0.8$. However. at around $\Phi = 0.8$. the orbit size is commensurate with the spacing between the dots and these negative eigenvalues are changed into positive eigenvalues. During this process. the electron is pushed by the dot and thus the forward scattering occurs. So. the intensities of $\sigma_{xx}^{(0)}$ are increased when U_0 is negatively increased. At very low magnetic fields (below $\Phi = 0.7$). the intensities are normally decreased when U_0 is negatively increased. This is beacuse the electron with very large orbit is bounded by the strong negative dot potential. In this case. the bounding effect by the dot is much dominant and the electron is more likely to be bounded when the dot potential is deeper. So. the intensities are decreased when U_0 is negatively increased. From this phenomenon. we can see that the bounding effect by the dot potenital is different from the scattering effect by the anti-dot scatterers.

5.2 Hall Conductivities

In this section. Hall conductivity $\sigma_{yx}^{(0)}$ will be discussed. As seen in the Eq.(32) and (42), it is all electronic eigenstates below the Fermi level energy that contribute to the Hall conductivity $\sigma_{yx}^{(0)}$. Therefore, the low-lying eigenstates can see the change of the scatterer or dot size even though they have Fermi level energy

to overcome the strength of the modulation. So. it is seen that the intensities are appreciably changed for all cases. We will consider the effect how the Hall conductivity $\sigma_{yx}^{(0)}$ depends on N and U_0.

5.2.1 Dependence of the Hall Conductivities on N

Anti-dot regime Fig. 20 (a). (b). and (c) show the Hall conductivities $\sigma_{yx}^{(0)}$ with N for the anti-dot regime. Fig. 20 (a) is the result for the low modulation case ($U_0 = 1.235$). First feature shown in this figure is that when N increases. the intensity of $\sigma_{yx}^{(0)}$ is increased. In this low modulation regime. the Fermi level energy ($\sim 0.259meV$) is higher than the strength of the scttcrers ($0.156meV$). However. as mentioned above. since the Hall conductivities $\sigma_{yx}^{(0)}$ are contributed by the all eigenstates below the Fermi level energy. the low-lying states can see the change of the scatterer size. And when N is increased. the spacing between the scatterers is increased. So. the intensities of $\sigma_{yx}^{(0)}$ are increased. The second feature is that the ocsillatory behaviour due to the DOS is still observed. This is because the Fermi level energy ($\sim 0.259meV$) is higher than the strength of the scttcrers ($0.156meV$). The third feature is that in the low magnetic field region. $\sigma_{yx}^{(0)}$ is suppressed. Since all eigenstates below the Fermi level energy contribute to the $\sigma_{yx}^{(0)}$. not only the states near the Fermi level energy but also the low-lying states below the Fermi level energy are to be considerded.

Hall Conductivities as a Function of N for the Anti-dot

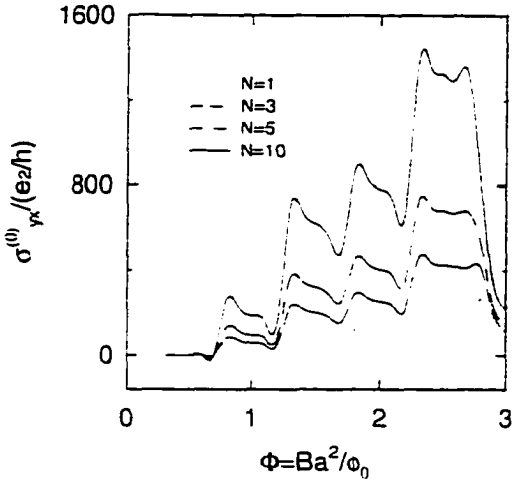

(a) $U_0 = 1.235$

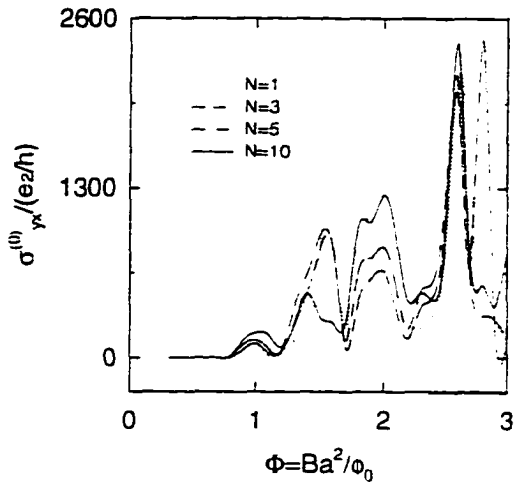

(b) $U_0 = 10$

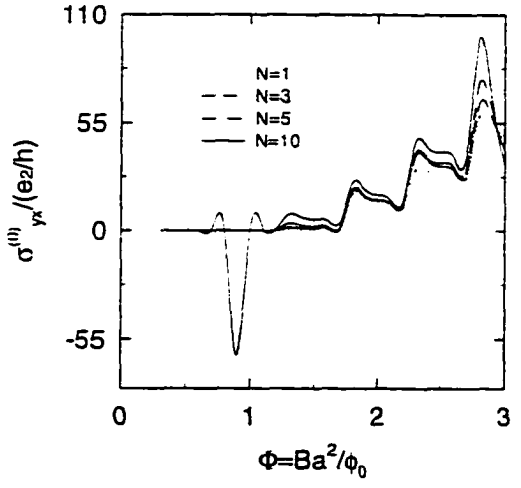

(c) $U_0 = 100$

Figure 20: Hall conductivities $\sigma_{yx}^{(0)}/(e^2/h)$ vs. $\Phi = Ba^2/\phi_0$ for the various size of the scatterers. $N_x = N_y = 4$, $n = 3$, $n_{2D}a^2 = 0.5$, and $a = 200nm$.

The low-lying states have little probability to overcome the strength of the scatterer and it is more likely to be scattered from the scatteres. And also, since, at low magnetic fields, the orbit is large, they are affected by the scattering centers. These scattered electrons have smaller probability of contributing to $\sigma_{yx}^{(0)}$. For this reason, at low magnetic fields, $\sigma_{yx}^{(0)}$ is suppressed. Fig. 20 (b) is the result for the intermediate modulation case ($U_0 = 10$). The trend that, when N increases, the intensity of $\sigma_{yx}^{(0)}$ is increased is partly preserved. However, in this regime, since the potenital barrier is high, the anormalous resonant scattering effects are shown. And also, the oscillatory behaviour and the suppression of the Hall conductivities $\sigma_{yx}^{(0)}$ at low magnetic fields are observed. Fig. 20 (c) is the result for the strong modulation case ($U_0 = 100$). As in the previous cases, when N increases, the intensity of $\sigma_{yx}^{(0)}$ is increased. And the oscillatory behaviour and the suppression of the Hall conductivities $\sigma_{yx}^{(0)}$ at low magnetic fields are observed. However, the striking feature in this regime is the negative Hall conductivities at around $\Phi = 0.8$. In this region, the orbital radii are commensurate with the spacing between scatters. So, the electrons with this commensurate orbit can make the backward scattering after scattered off the scatterers. Theses backward scattering effect makes the negative Hall conductivities and they make the negative Hall resitivities which will be shown later. (See Fig. 32) In this case, the net scattering force overcomes the Lorentz force, producing a negative Hall voltage. In our case, these negative Hall conductivities are negatively increased when U_0

is increased.

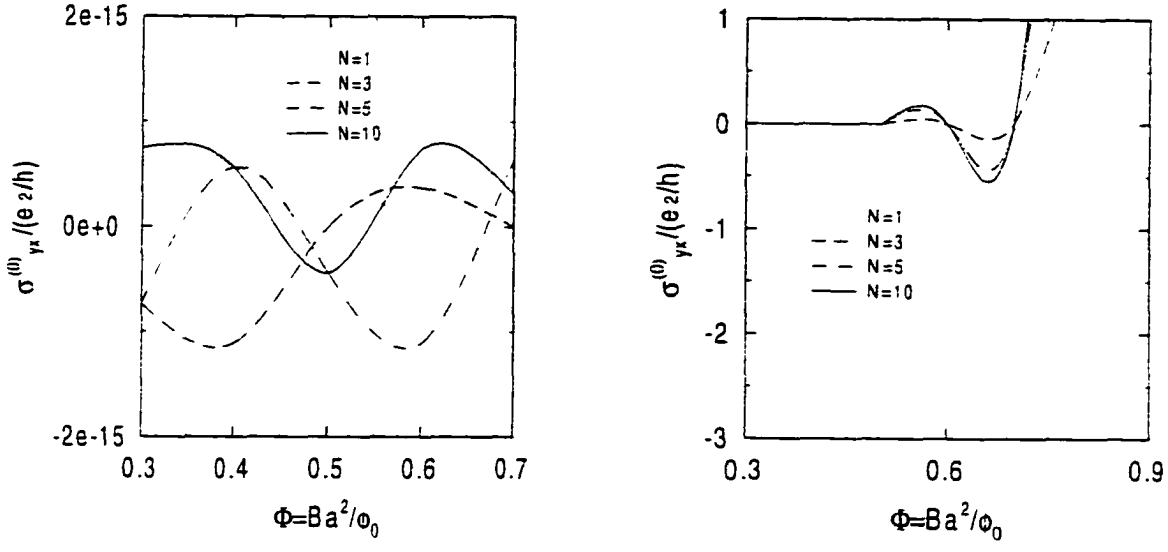

(a) $U_0 = 1.235$ (b) $U_0 = 10$

Figure 21: Negative Hall conductivities $\sigma^{(0)}_{yx}/(e^2/h)$ vs. $\Phi = Ba^2/\phi_0$ at low magnetic fields $N_x = N_y = 4$. $n = 3$, $n_{2D}a^2 = 0.5$, and $a = 200nm$.

When $U_0 = 1.235$ (Fig 21 (a)), the negative Hall conductivities are barely seen at low magnetic fields. The reason is that, in this low modulation case, the scattering effect is very weak because the potential barrier is not high. Accordingly, the backward scattering is also weak and the negative Hall conductivities are barely seen at low magnetic fields. However, when $U_0 = 10$ (Fig 21(b)), the situation is slightly different. The negative Hall conductivities are recognizably seen at around $\Phi = 0.8$ for $N = 1$ case. In this intermediate modulation case, the potential barrier is higher than the case when $U_0 = 1.235$. So, the scattering effects are more and the backward scattering can be more. In our case, the pos-

sible backward scattering occurred for large scattere size ($N = 1$). The strong modulation case. When $U_0 = 100$ (Fig 20(c)). the negative Hall conductivities are remarkable at aroud $\Phi = 0.8$ for the steeper potential ($N = 10$). Fom these facts. we can guess that these negative Hall conductivities come from the backward scattering by the scatterers.

Quantum-dot regime Fig. 22 (a). (b). and (c) show the numerical results of the Hall conductivities with N for the quantum-dot regime. Fig. 22 (a) is for the low modulation case ($U_0 = -1.235$). All the features are same as seen in Fig. 20 (a). When the dot size is reduced (N is increased). the intensities are increased because the elcetron can have more space between the dots . And the oscillatory behaviour due to the DOS is obviously observed since the depth of the dot is not deep. And also. the suppression of the intensities at low magnetic fields is observed as in the anti-dot case. (Fig. 20 (a)) When $U_0 = -10$ (Fig. 20 (b)). the oscillatory behaviour is still observed for $N = 3, 5$. and 10. But this oscillatory behaviour is disappeared for $N = 1$. instaead. there are appreciable negative Hall conductivities as in the anti-dot case. However. in this case. plus-to-minus oscillations which are not observed in anti-dot case are observed. These plus-to-minus oscillations are due to the Aharonov-Bohm oscillations. Due to the increase of U_0, the guiding centers are mixed and the electron orbits can be overlapped each other.

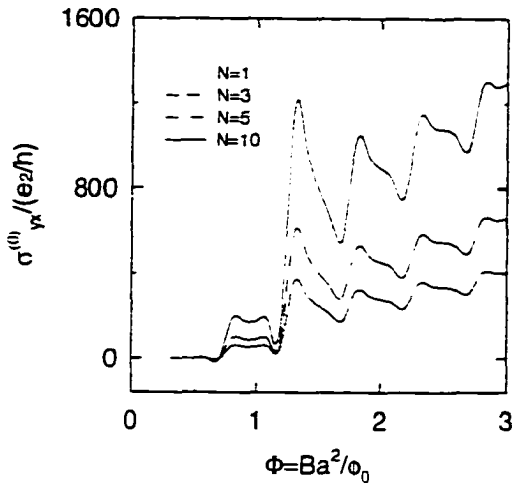

(a) $U_0 = -1.235$

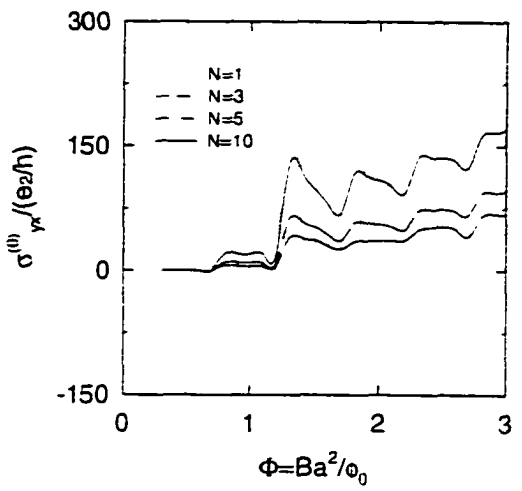

(b) $U_0 = -10$

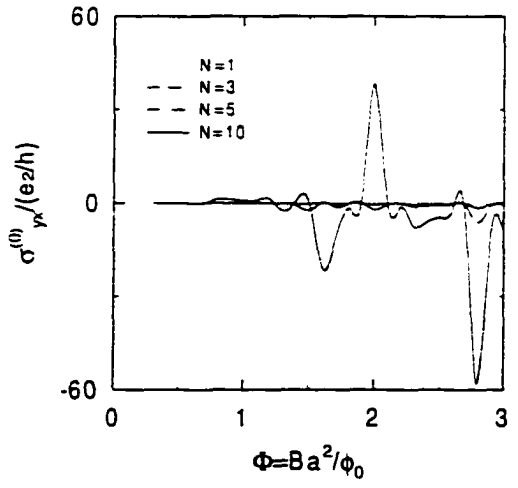

(c) $U_0 = -100$

Figure 22: Hall conductivities $\sigma^{(0)}_{yx}/(e^2/h)$ vs. $\Phi = Ba^2/\phi_0$ for the various size of the dots. $N_x = N_y = 4$, $n = 3$, $n_{2D}a^2 = 0.5$, and $a = 200nm$.

So. this overlap of the electron orbits due to the mixing of guiding centers causes more trapping by the quantum dot and eventually. the net scattering force overcomes the Lorentz force. producing a negative Hall conductivity. This generates the large plus-to-minus oscillations in $\rho_{xy}^{(0)}$. These plus-to-minus oscillations are also observed for the small size ($N = 10$) of the dot with $U_0 = -100$ (Fig. 22 (c)). But. in this small and deep dot case. the negative intensities are much more reduced than when $U_0 = -10$ because the electron is more likely to be bound within the dot instead of generating the backward scattering. Fig. 23 supports this bounding effect.

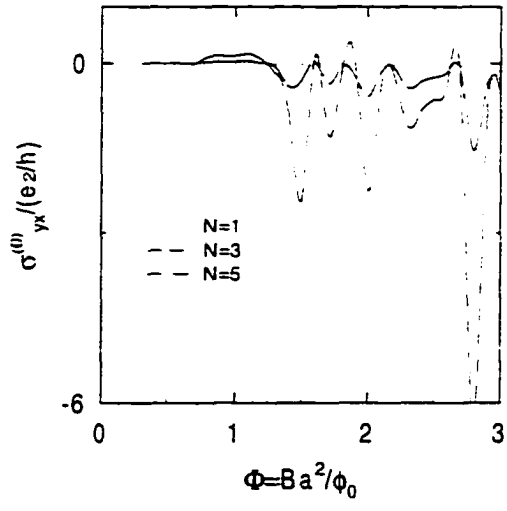

Figure 23: Hall conductivities $\sigma_{yx}^{(0)}/(e^2/h)$ vs. $\Phi = Ba^2/\phi_0$ for various size of the dots with $U_0 = -100$. $N_x = N_y = 4$, $n = 3$, $n_{2D}a^2 = 0.5$, and $a = 200nm$.

In Fig. 23, the negative intensities are appreciably reduced when N is decreased. This means that, for the larger size of the dot. the electron is more

likely to be bounded within the dot. The fact that the negative intensities are reduced when U_0 is increased. is contrast with the anti-dot case in which the backward scattering is enhanced and make the negative intensities large when U_0 is increased. From these facts. again. we know that the negative Hall conductivities are generated when the backward scattering is dominant.

5.2.2 Dependence of the Hall Conductivities on U_0

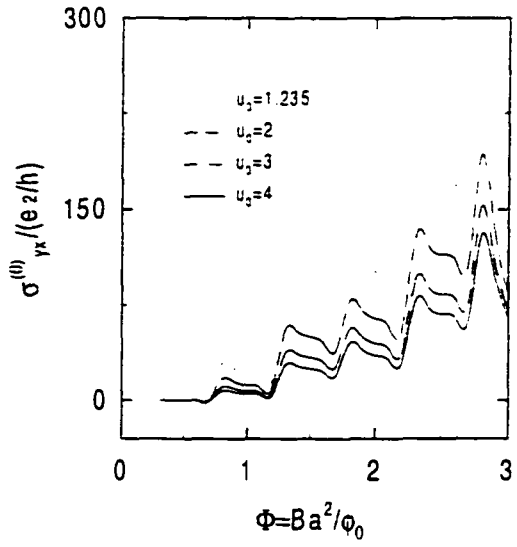

Figure 24: Hall conductivities $\sigma_{yx}^{(0)}/(e^2/h)$ vs. $\Phi = Ba^2/\varphi_0$ for various strengths of the scatterers with $N = 1$. $N_x = N_y = 4$, $n = 3$, $n_{2D}a^2 = 0.5$. and $a = 200nm$.

Anti-dot regime Fig. 24 shows the Hall conductivities $\left(\sigma_{yx}^{(0)}\right)$ for various strengths of U_0 for the positive scatterers. All the features are similar with the results for the $\left(\sigma_{yx}^{(0)}\right)$ for various sizes of N for the positive scatterers (ref.20) because the strength of the scatterer is not much higher than the Fermi level energy. So, we can see the oscillatory behaviour due to the DOS. And the suppression of the Hall conductivities is also shown at low magnetic fields. However, the intensities of the Hall conductivities are decreased when U_0 is increased as expected. Basically, when U_0 is increased, the scattering by the potential is increased and the conductivities are decreased. So the intensities are decreased when U_0 is increased.

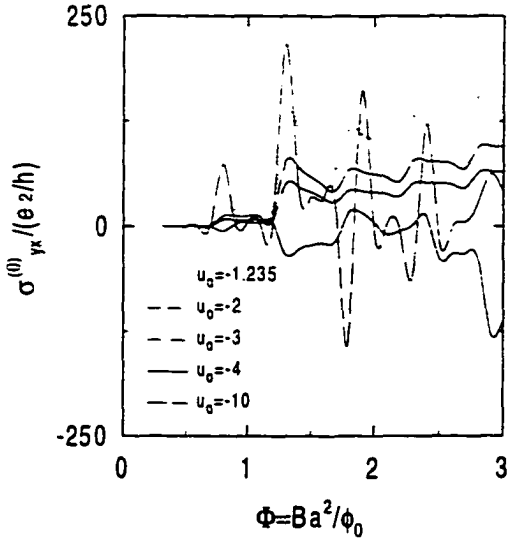

Figure 25: Hall conductivities $\sigma_{yx}^{(0)}/(e^2/h)$ vs. $\Phi = Ba^2/\phi_0$ for various depths of the dots with $N = 1$. $N_x = N_y = 4$, $n = 3$, $n_{2D}a^2 = 0.5$, and $a = 200nm$.

Quantum-dot regime For small U_0 $(-1.235, -2, -3)$. all the features are similar with the previous anti-dot case. We can see the oscillatory behaviour due to the DOS. And the suppression of the Hall conductivities is also shown at low magnetic fields. In addition to this. the intensities of the Hall conductivities are decreased when U_0 is negatively increased because the electron is more trapped by the dot potential. But this situation is quite different when $U_0 = -4$ and -10. When $U_0 = -4 or -10$. $\sigma_{yx}^{(0)}$ has negative valus(for $U_0 = -4$) or plus-to-minus oscillations (for $U_0 = -10$). With the same reason as in the quantum-dot case in section 5.2.1. when U_0 is negatively strong ($U_0 = -4 or -10$). the overlap of the electron orbits due to the mixing of guiding centers causes more trapping by the negative potential and eventually. the net scattering force overcomes the Lorentz force. producing a negative Hall conductivity. This generates the large plus-to-minus oscillations in $\rho_{xy}^{(0)}$. These negative values generate the negative Hall resistivities later.

5.3 Longitudinal Resistivities

In this section. we present the numerical results for the longitudinal resistivities $\left(\rho_{xx}^{(0)}\right)$ for two dimensional square array of antidot and dot potentials with various sizes and strengths according to the values of N and U_0. Because our model is the square array of anti-dot or dot modulation, x and y direction are symmetry. So the Longitudinal Resistivities are obtained from the Eq. (58)

5.3.1 Dependence of the Longitudinal Resistivities on N

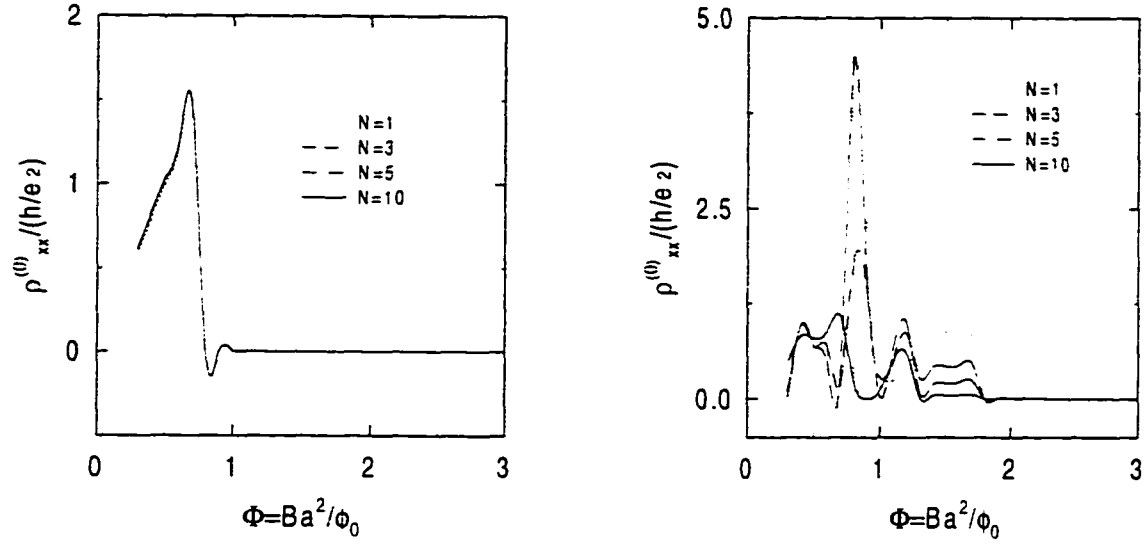

(a) $U_0 = 1.235$ **(b)** $U_0 = 100$

Figure 26: Longitudinal Resistivities $\rho^{(0)}_{xx}/(h/e^2)$ vs. $\Phi = Ba^2/\phi_0$ for various size of the scatterers : $N_x = N_y = 4$, $n = 3$, $n_{2D}a^2 = 0.5$, and $a = 200nm$.

Anti-dot regime Plotted in Fig. 26 (a) and (b) are the longitudinal resistivities $\left(\rho^{(0)}_{xx}\right)$ for the anti-dot regime ($U_0 > 0$) when N is varied. Fig. 26 (a) shows the longitudinal resistivities for the low modulation case. As in the previous case, all the curves are not sensitive for the variation of the scatterer size because the Fermi level is higher than the strength of the scatterers. However, one big peak is shown at low magnetic fields. This big peak is not changed appreciably as N is changed. According to the Eq.(58), the amplitude of $\rho^{(0)}_{xx}$ in the low magnetic field limit depends on $\sigma^{(0)}_{xx}$ since $\sigma^{(0)}_{yx}$ is suppressed at low magnetic fields as shown in Fig. 15 and Fig. 20. Therefore, we can see that $\rho^{(0)}_{xx}$ at low magnetic

fields is contributed by the electrons near the Fermi level energy because $\sigma_{xx}^{(0)}$ is contributed by those electrons. As we explained, the Fermi energy, which is ~ 0.259 meV, is higher than the the potential strength $U_0 = 1.235$ (or $V_0 = 0.156$ meV). Therefore, considering energies, the electrons with higher Fermi energy than the potential strength can probably go over the potential barrier. For this reason, those electrons with higher Fermi energy are not much affected by the variation of the scatterer size. However, it is guessed that this big peak comes from the ballistic scattering due to the sample boundary. At low magnetic fields, the cyclotron orbit is very large. In our case, its radius is around four times bigger than the modulation lattice period. So those large orbits of the electrons with the Fermi level energy which is higher than the starength of the scatterer can touch the sample boundary because our sample has $4x4$ square array of anti-dot. It behaves like the ballistic scattering. So, we increased the strength of the scatterers to reduce the sample boundary effect. It is shown in Fig. 26 (b). This is for $U_0 = 100$ (or $V_0 = 12.6$ meV). In this figure, the big giant peak is much reduced and another resonant peaks are shown. So, it is guessed that this big peak comes from the ballistic scattering due to the sample boundary. Another feature in Fig. 26 (a) is the scattering effect for the variation of the scatterer size. Even though the intensities are not very sensitive for the variation of the scatterer size because the Fermi level energy is higher than the strength of the scatterers, we can see a liitle change of the intensities. Fig. 27 (a) and (b) are

for the detailed Longitudinal Resistivities $\rho_{xx}^{(0)}/(h/e^2)$ at low and high magnetic fields. respectively.

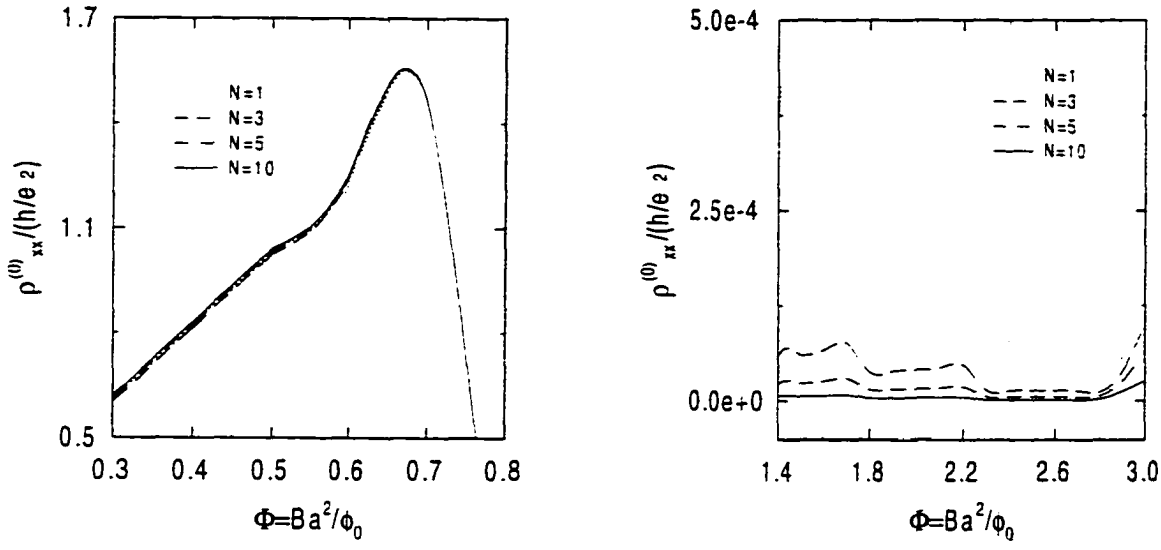

(a) at low Φ **(b) at large Φ**

Figure 27: Detailed Longitudinal Resistivities: $\rho_{xx}^{(0)}/(h/e^2)$ vs. $\Phi = Ba^2/\phi_0$ for $U_0 = 1.235$ $N_x = N_y = 4$. $n = 3$. $n_{2D}a^2 = 0.5$. and $a = 200nm$.

In Fig. 27 (a). when N is increased. the amplitudes are slightly increased. However. the opposite behavior to this occurs in all the other ranges of Φ. (Fig. 27 (b)). That is. when N is increased, the amplitudes are decreased. So. we can see that the effect due to scattering on an open orbit in the low magnetic field region, is different from that in the high magnetic field region. At low magnetic fields, the cyclotron orbit includes two to four scatterers. These large orbits are not closed as the electrons are scattered. These open orbits depend on the steepness of the potential barrier. In general, the steeper potenital makes the larger resistivities.

So their contributions to $\rho_{xx}^{(0)}$ make the amplitudes slightly larger when N is increased. Another analysis is that this reflects the forward scattering is enhanced by the scatteres when N is decreased in this region. So when N is decreased, the eletrons are pushed forward so that the conductivities are increased and thus the resistivities are increased. However, at high magnetic fields, $\rho_{xx}^{(0)}$ depends more on $\sigma_{yx}^{(0)}$ since the Hall conductivity has large amplitudes there. Also, the size of the orbit, in this range of magnetic fields, is just comparable with or smaller than the lattice size. So the electron motion depends more on the spacing between the scatterers than the steepness of the slope. As N increases, the slightly wider space between the scatterers is created and due to those wider spaces, the conductivities are increased and the resistivities are decreased as shown in Fig. 27 (b). This behavior similarly occurs for the quantum dot regime but a slightly different feature is obtained in the low magnetic field region.

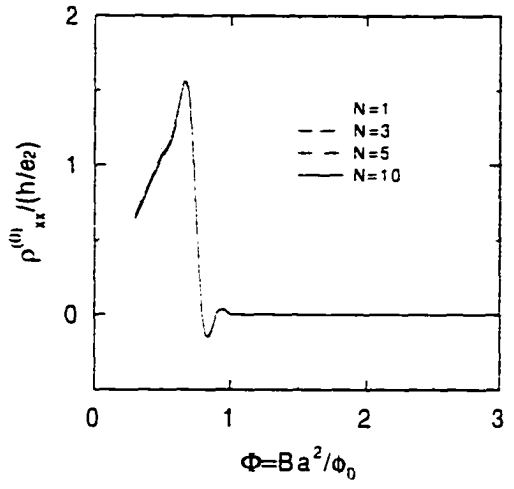

(a) $U_0 = -1.235$

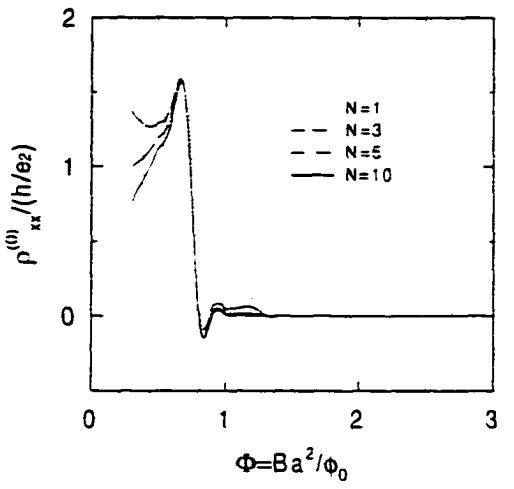

(b) $U_0 = -10$

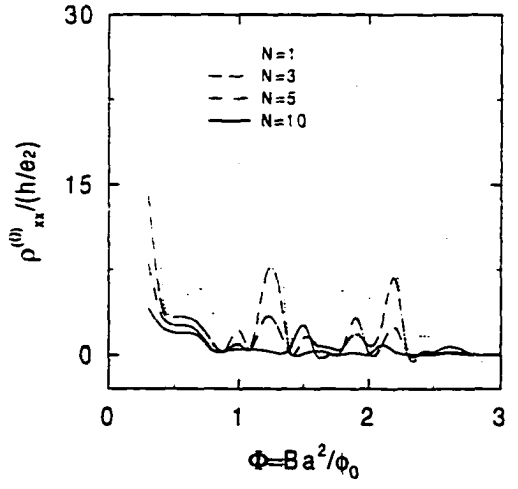

(c) $U_0 = -100$

Figure 28: Longitudinal resistivities $\rho^{(0)}_{xx}/(h/e^2)$ vs. $\Phi = Ba^2/\phi_0$ for the various size of the dots. $N_x = N_y = 4$, $n = 3$, $n_{2D}a^2 = 0.5$, and $a = 200nm$.

Quantum-dot regime Fig. 28 (a). (b). and (c) gives the numerial results of longitudinal resistivities for the Quantum-dot potential as N is varied. Fig. 28 (a) is for the low modulation case ($U_0 = -1.235$). All the features are same as in the anti-dot case because the Fermi level energy is higher than the strength of the dot. There is a big peak at low magnetic fields. guessed as the ballisitc scattering due to the sample boundary. And when N is changed. this peak is not appreciably changed. Also.at high magnetic fields. when N is increased. the intensities are decreased due to more free space between the dots.(Fig. 29 (b))

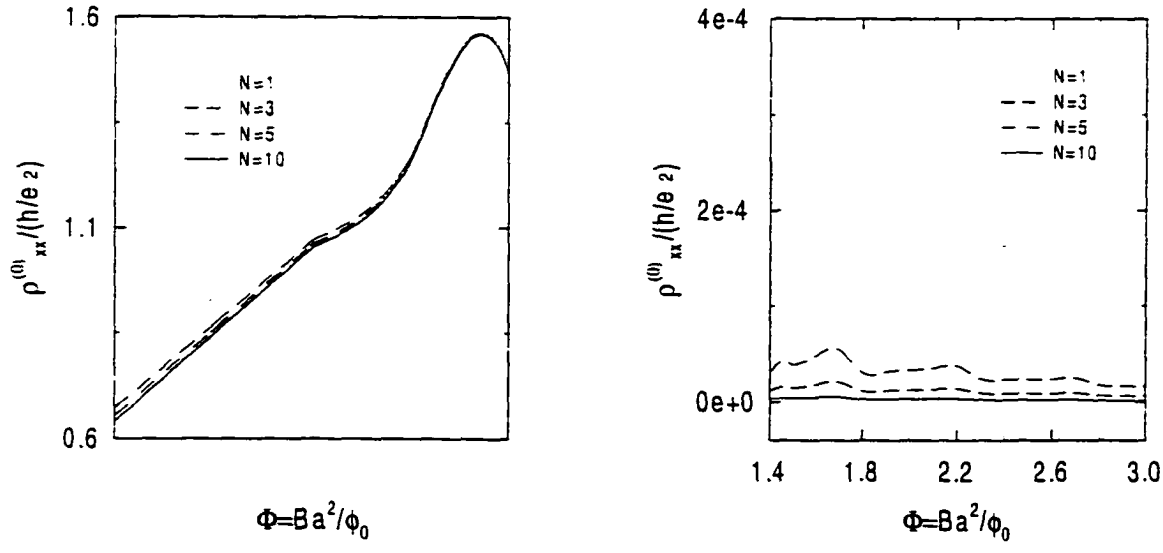

(a) at low Φ **(b) at large Φ**

Figure 29: Detailed Longitudinal Resistivities; $\rho^{(0)}_{xx}/(h/e^2)$ vs. $\Phi = Ba^2/\phi_0$ for $U_0 = 1.235$ $N_x = N_y = 4$, $n = 3$, $n_{2D}a^2 = 0.5$, and $a = 200nm$.

However, at low magnetic fields, the intensity change is slightly different from that in anti-dot case. Because when N is increased, the intensities are decreased

which is contrast with the anti-dot case.(Fig. 29 (a)) In this quantum dot case. the open orbit at low magnetic fields is captured by the dot. So. if the dot size is bigger. then the probability of being captured by the dot is increased. Therefore. the intensities of longitudinal resistivities are increased when N is decreased. Fig. 28 (b) supports this fact. Fig. 28 (b) is for the negatively stronger dot than Fig. 28 (a) case. In this figure. the intensities at low magnetic fields are drastically changed even though the ballistic scattering due to the sample boundary is still shown. When N is increased. the intensities are decreased. This means that if the dot size is shrinked. then the probability of electron's being captured is decreased and the resistivities are decreased. When $N = 1$ case. there is a big change in intensities at low magnetic fields. When $N = 1$. the dot size is biggest in our case and the capturing capability is largest. Therefore. at low magnetic fields. capturing effect is more dominant than the ballistic scattering due to the sample boundary in this stronger modulation. That is why there is a big change in intensities at low magnetic fields. At high magnetic fields. there are some resonant peaks due to the commensurate orbit with the spacing between the dots at around $\Phi = 2.1$ and $\Phi = 2.7$. These resonant peaks are very well shown in the strong modulation case. Fig. 28 (c) is for the strong dot. At low magnetic fields. there are low-field giant peaks which are reduced when N is increased as before. And the low field peak due to the sample boundary is a little bit shwon at around $\Phi = 0.7$. But it is almost disappeared because this case is strong modulation case.

So we can see that the boundary effect is screened by the capturing effect. In the whole range of Φ, there are many resonant peaks due to the commensurate orbit with the spacing between the dots. These resonant peaks are reduced when N is increased. This is contrst with the low modulation case Fig. 28 (a). From these facts, in this strong case, even at high magnetic fields, the capturing effect is more dominat than the contribution due to the free space.

5.3.2 Dependence of the Longitudinal Resistivities on U_0

Anti-dot regime Fig.30 (a) shows the longitudinal resistivities $\left(\rho_{xx}^{(0)}\right)$ for the anti-dot regime as U_0 is varied. As before, the low field giant peak due to the ballistic scattering by the sample boundary is still seen at around $\Phi = 0.7$ because, as mentioned above, the strength of the scatterer is not much higher than the Fermi level energy. At low magnetic fields, the amplitudes are significantly changed with U_0. When U_0 is increased from $U_0 = 1.235$ to 3, the amplitudes decrease and when $U_0 = 4$, the amplitudes are abruptly enhanced and when $U_0 = 10$, they go back to the lower amplitude than the ones when U_0 is increased from $U_0 = 1.235$ to 3. This reflects that when U_0 is increased, some scattering is in the forward direction and others are in the backward because they are randomly scattered. If the net scattering is forward, then it increases the conductivities and decreases the resistivities and vice versa, if it is backward. For this reason, the intensity for $U_0 = 4$ is due to the dominant backward scattering off the anti-dot

scatterers and all the others are dominant forward scattering. At $\Phi > 1$ regions. there are some resonant scattering effects due to the commensurate orbit of the electron with the space between the scatterers. When $U_0 = 10$. the resonant scattering occurs at around $\Phi = 1.1$ and when $U_0 = 4$. the resonant scattering occurs at around $\Phi = 2$ and $\Phi = 2.3$.

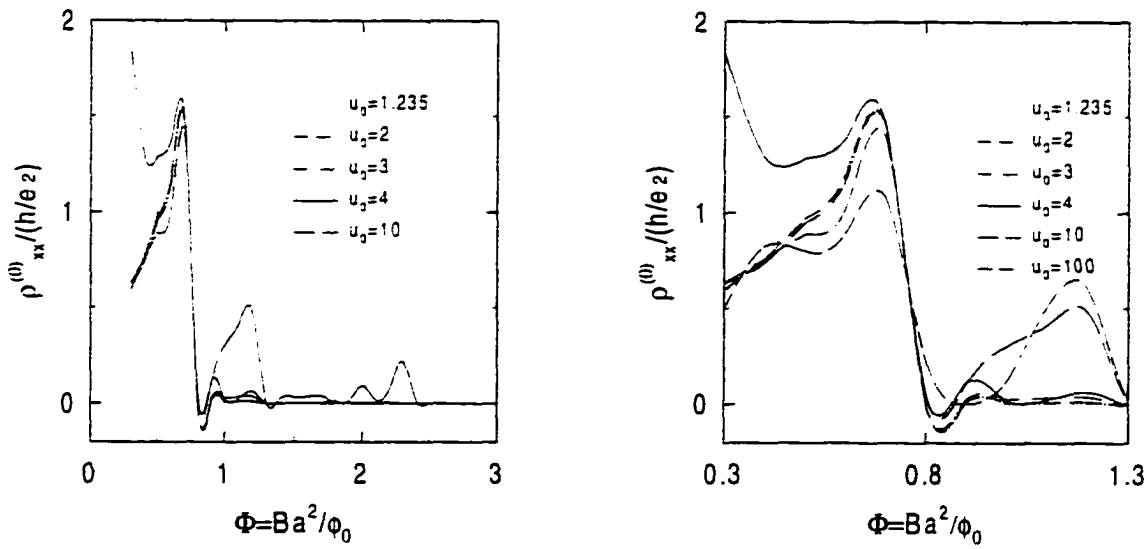

(a) (b)

Figure 30: (a) Longitudinal Resistivities $\rho^{(0)}_{xx}/(h/e^2)$ vs. $\Phi = Ba^2/\phi_0$ with U_0 for $N = 1$ (b) Detailed double peak structures with U_0 where $N = 1$ is used for $U_0 = 1.235 \sim 10$ and $N = 10$ is used for $U_0 = 100$: $N_x = N_y = 4$. $n = 3$, $n_{2D}a^2 = 0.5$. and $a = 200nm$.

The characteristic feature in this resonant scattering is the double peak structure shown in $U_0 = 10$ case. The first peak is not appreciably changed but the second peak is drastically changed when U_0 is increased, especially for $U_0 = 10$. The first peak is, as mentioned above, considered as a geometric effect such as

the ballistic scattering. On the other hand. the second peak is due to resonant scattering off the antidot potential since the amplitudes are gradually increased when U_0 is increased. These double peak structures are magnified in Fig. 30 (b) to discuss further. Fig. 30 (b) is the results for the double peak structures magnified from Fig. 30 (a) and Fig. 26 (b). Magnified from Fig. 30 (a) is for $N = 1$ and Magnified from Fig. 26 (b) is for $N = 10$ to show the double peak structures very well. Except $U_0 = 4$ case. the first peak is reduced when U_0 is increased. What this means is that the geometric effect is screened by the strong anti-dot potential. However. the second peak is gradually increased when U_0 is increased. So. this second peak is considered as the result of resonant scattering off the antidot potential. This double peak structure is also shown in the experiments for the strong modulation.[18]

Quantum-dot regime Fig. 31 shows Longitudinal Resistivities $\rho_{xx}^{(0)}$ for the various depths of the dots in the quantum-dot regime. At low magnetic fields. the intensities are gradually increased when U_0 is negatively increased. This is contrast with the anti-dot case.(Fig. 31) In anti-dot case, the forward scattering by the scatterers was dominant at low magnetic fields but, in this quantum-dot regime, this forward scattering is not occurred by the capturing effect of the dots. So. when U_0 is negatively increased, the captuing capability is increased and the resistivities are increased. At high magnetic fields, there are some resonant peaks due to the commensurate orbit with the space between dots as in the anti-dot

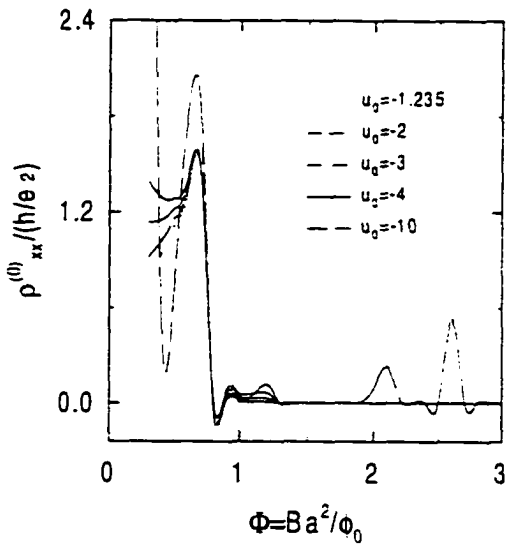

Figure 31: Longitudinal Resistivities $\rho_{xx}^{(0)}/(h/e^2)$ vs. $\Phi = Ba^2/\phi_0$ with negative U_0 for $N = 1$. $N_x = N_y = 4$, $n = 3$. $n_{2D}a^2 = 0.5$, and $a = 200nm$.

case.

5.4 Hall Resistivities

In this section, we present the numerical results for the Hall resistivities $\left(\rho_{xy}^{(0)}\right)$ for two dimensional square array of antidot and dot potentials with various sizes and strengths according to the values of N and U_0 as in section subsec:2drhoxx0. The Hall Resistivities are obtained from the Eq. (59) In contrast to the longitudinal resistivities, they more depend on the behavior of $\sigma_{yx}^{(0)}$ as seen in Eq. (59). Here, the quenchung and the negative Hall resistivities are discussed. These quenching and the negative Hall resistivities are found in the other experiments for the strong

modulation anti-dot.[18, 46] In this section, these effects are further analyzed by varying the size (N) and the strength (U_0) of the modulation.

5.4.1 Dependence of the Hall Resistivities on N

Anti-dot regime Fig. 32 (a), (b), and (c) are the numerical results for the Hall resistivities $\left(\rho_{xy}^{(0)}\right)$ with different N for the anti-dot regime. Fig. 32 (a) is for the low modulation case $U_0 = 1.235$. The oscillatory behavior due to the DOS, as expalined in section 5.1 and 5.1, is shown because the modulation is low. When the scatter size is decreased (i.e. N is increased), the Hall resistivities are decreased because the electron can have more space between the anti-dots to freely move. The characteristic feature is that the Hall resistivities are quenched at low magnetic fields. In our case, this quenched Hall resistivities at low magnetic fields are due to the suppression of $\left(\sigma_{yx}^{(0)}\right)$. (Fig. 20) The suppression of $\left(\sigma_{yx}^{(0)}\right)$ means that the collimated electrons which experience the forward scattering after scatterred by the potential can have the same energies as the Hall voltage and there are no net current in Hall voltage direction so that the Hall voltage is quenched. Therefore, the quenching effect, in our case, is considered as the result due to the resonant scattering of the collimated electrons scatterred by the scatterers. These quenching effect is shown in all three figures (a), (b), and (c). If these collimated electrons can have more energies to overcome the Hall voltage, then it can have even the negative Hall resistivites.

Hall Resistivities as a Function of N for the Anti-dot

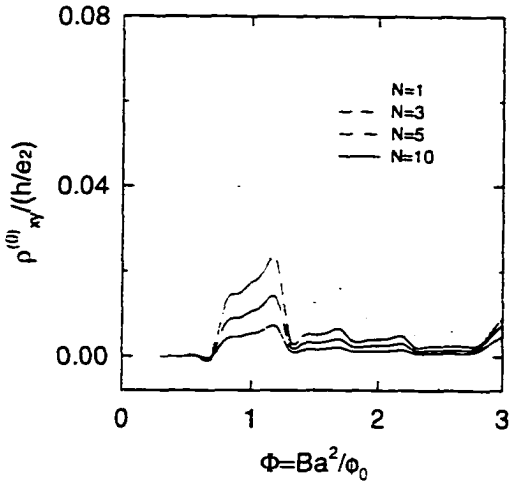

(a) $U_0 = 1.235$

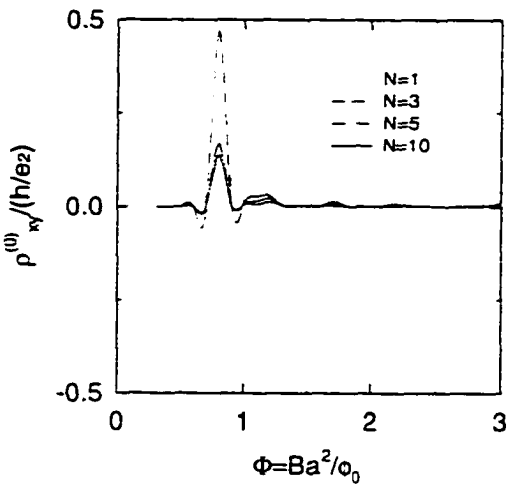

(b) $U_0 = 10$

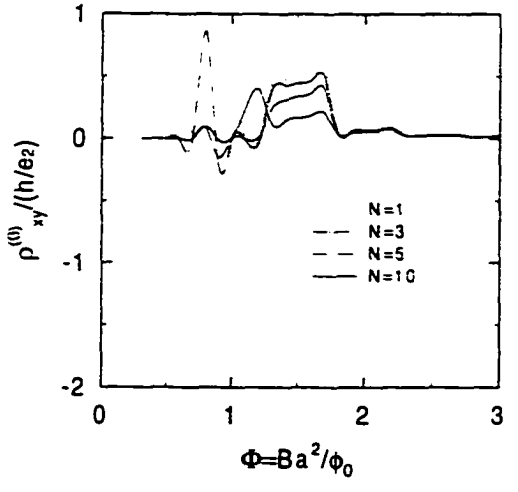

(c) $U_0 = 100$

Figure 32: Hall resistivities $\rho^{(0)}_{xy}/(h/e^2)$ vs. $\Phi = Ba^2/\phi_0$ for the various size of the anti-dots. $N_x = N_y = 4$, $n = 3$, $n_{2D}a^2 = 0.5$, and $a = 200nm$.

It is hard to see this negative Hall resistivity in Fig. 32 (a) because it is too small. But. it is seen very well in Fig. 32 (b). Fig. 32 (b) is for the Hall resistivities $\left(\rho_{xy}^{(0)}\right)$ of the intermediate modulation $U_0 = 10$ case of anti-dot with different N. It also shows the quenching effect at low magnetic fields due to the resonant scattering of the collimated electrons. Except for $N = 1$ case, the Hall resistivities are decreased when N is increased because the electrons can have more space between the anti-dots to freely move. However. in this figure. the striking feature is the negative Hall resisitvities at around $\Phi = 0.8$ in $N = 1$ case due to the resonant scattering of the collimated electrons which have more energies to overcome the Hall voltage. This negative Hall resistivites depend on the strength of the scatterers in our case.

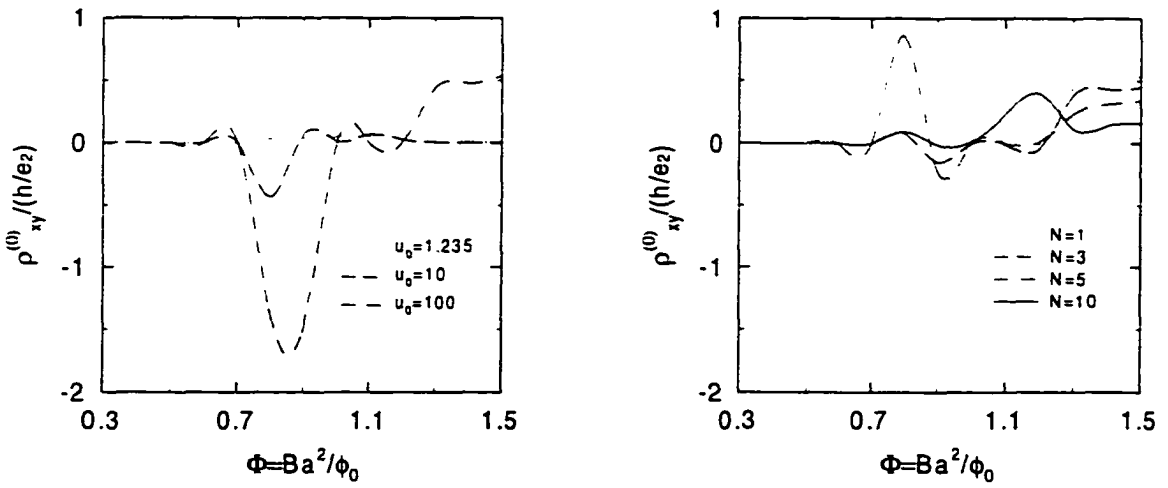

Figure 33: Negative Hall Resistivities $\rho_{xy}^{(0)}/(h/e^2)$ vs. $\Phi = Ba^2/\phi_0$ (a) with U_0 for $N = 1$ (b) with N for $U_0 = 100$; $N_x = N_y = 4$, $n = 3$, $n_{2D}a^2 = 0.5$, and $a = 200nm$.

Fig. 33 (a) shows this scatterer strength dependent negative Hall resistivities. Fig. 33 (a) is the magnified result of Fig. 32 (a), (b), and (c) for $N = 1$. When $U_0 = 1.235$, the negative Hall resistivity is too small to see the effect. But when U_0 is increased from 10 to 100, the negative Hall resistivities are increased and shifted toward the low magnetic fields due to the width of the cosine modulation. Because, when the amplitude of the cosine modulation is increased, the width is also increased as well as its amplitude. Anyway, If the strength of the scatterers is increased, then the forward scattering can be enhanced and it can have more probability of overcoming the Hall voltage so that the negative Hall resistivities are increased. So, we can see that the negative Hall resistivities are due to the resonant scattering off the barriers. In addition to this, this negative Hall resistivity also depends on the size of the scatterers. It is shown in Fig. 33 (b). In our case, when N is increased, the negative Hall resistivities are ,with the exception of $N = 5$ case, decreased because the electron have more space to move when N is increased. From these facts, we conclude that the negative Hall resistivities are due to the resonant scattering of the collimated electrons to be able to overcome the Hall voltage and depend on the scatterer sizes as well as their strengths.

Quantum-dot regime Fig. 34 (a), (b), and (c) are the numerical results for the Hall resistivities $\left(\rho_{xy}^{(0)}\right)$ with different N for the quantum-dot regime. Fig. 32 (a) is for the low modulation case $U_0 = -1.235$. All the features are similar with

the anti-dot case because the modulation is low. The oscillatory behavior due to the DOS is shown and when the scatter size is decreased (i.e. N is increased), the Hall resistivities are decreased because the electrons can have more space between the dots to freely move. And also, the Hall resistivities are quenched at low magnetic fields. But the negative Hall resistivities still are not seen because it is too small. Fig. 34 (b) is for the intermediate modulation case $U_0 = -10$. Similar features are shown as in the low modulation case $U_0 = -1.235$ except when $N = 1$. When $N = 1$, the negative Hall resistivities are begun. However, in contrast with the anti-dot case, the negative Hall resistivities are at high magnetic fields ($\Phi > 2$ for $U_0 = -10$). In the anti-dot case, they were at low magnetic fields ($\Phi < 1$). In anti-dot case, the probability of overcoming the Hall voltage is more at low magnetic fields than at high magnetic fiels because the scattering depend on the orbit size. But, the Quantum-dot case has some different situation. When Φ is increased, the orbit size is reduced and if its size is small enough so that it is trapped within the dots, the high field electron can be captured by the dots at high magnetic fields. Therefore, if this capturing capability is enough so as to overcome the Hall volatge, then the high field electron can make the negative Hall resistivities. That is why, in the quantum-dot case, the negative Hall resistivities are at high magnetic fields. This is supported by Fig. 34 (c). Fig. 34 (c) is for the strong modulation case $U_0 = -100$. This figure also shows the negative Hall resistivities at high magnetic fields (in this case, $\Phi > 1$) as before.

Hall Resistivities as a Function of N for the Quantum-dot

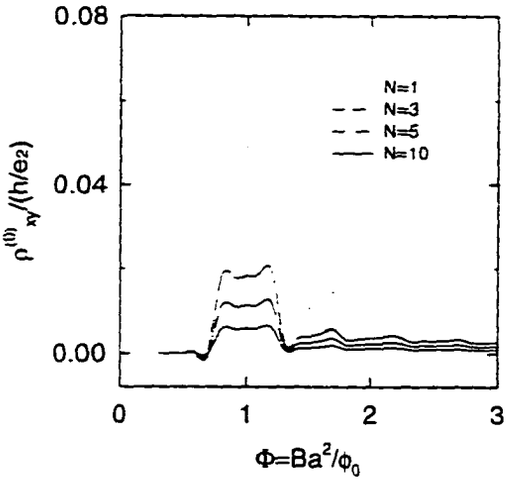

(a) $U_0 = -1.235$

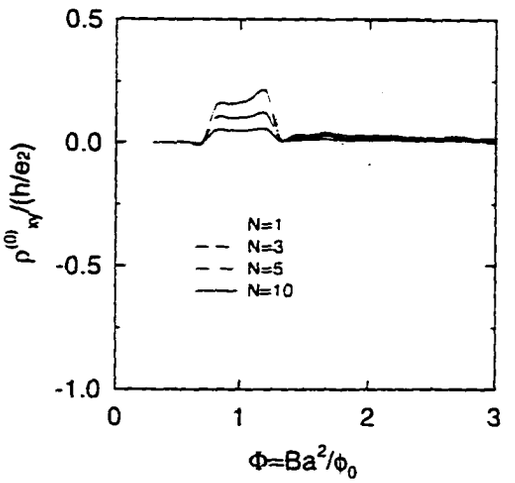

(b) $U_0 = -10$

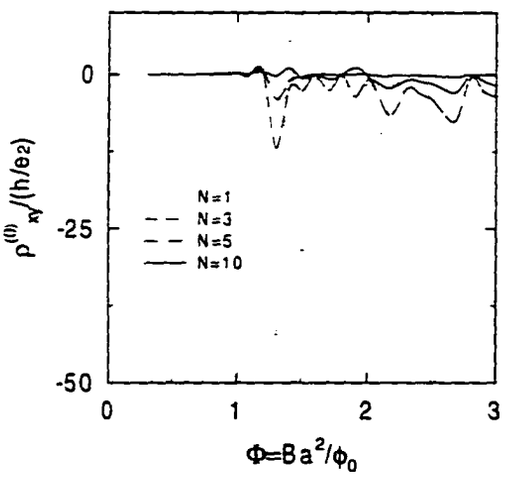

(c) $U_0 = -100$

Figure 34: Hall resistivities $\rho^{(0)}_{xy}/(h/e^2)$ vs. $\Phi = Ba^2/\phi_0$ for the various size of the dots. $N_x = N_y = 4$, $n = 3$, $n_{2D}a^2 = 0.5$, and $a = 200nm$.

However. in this figure. the negative Hall resistivities are oscillating with many periods. These oscillations are not due to the DOS. Because the oscillation period due to the DOS is $\Delta\Phi = 0.5$ but. in this strong modulation case. the period is $\Delta\Phi \sim 0.2$. So. we can see that these oscillations are not due to DOS. These oscillations are considered as the Aharonov-Bohm oscillations. For $\Phi = 0.7 \sim 2.0$. in our case. the LL mixing occurs or even the LLs at high magnetic fields are close to each other. Therefore. the wavefuntions are overlapped so that they lead to more tunneling between dots However. when $U_0 = -100$. the overlap due to guiding center mixing causes more trapping by the negative potential and eventually. the net force overcomes the Lorentz force. producing a negative Hall resistivity. The effect from magnetic breakdown when the electrons are trapped by strong dots. forces the electrons into either edge orbits (counterclockwise) or closed antidot-like orbits (clockwise). These two different paths make the Aharonov-Bohm oscillations. The oscillations shown in Fig. 34 (c) are considered as this kind of Aharonov-Bohm oscillations. The negative Hall resistivities with this ocsillation are gradually decreased when Φ is increased for $\Phi = 1 \sim 2$. This means that the resonant condition is reduced when the orbit size is reduced. For $\Phi > 2$. the negative Hall resisitivities are again increased. This reflects that the small size of the orbit can be captured by the strong dots. If these small size of orbits are captured by the strong dots so as to overcome the Hall voltage, then it makes the big negative Hall resistivities. That is why the negative Hall

resistivities are increased again for $\Phi > 2$. These Hall resistivites have the exact oscillation period even when the dot size is changed. In addition to this, When the dot size is reduced, the negative Hall resistivities are reduced as expected because the capturing capabilities are reduced. Of course, the quenching effect is observed at low magnetic fields.

5.4.2 Dependence of the Hall Resistivities on U_0

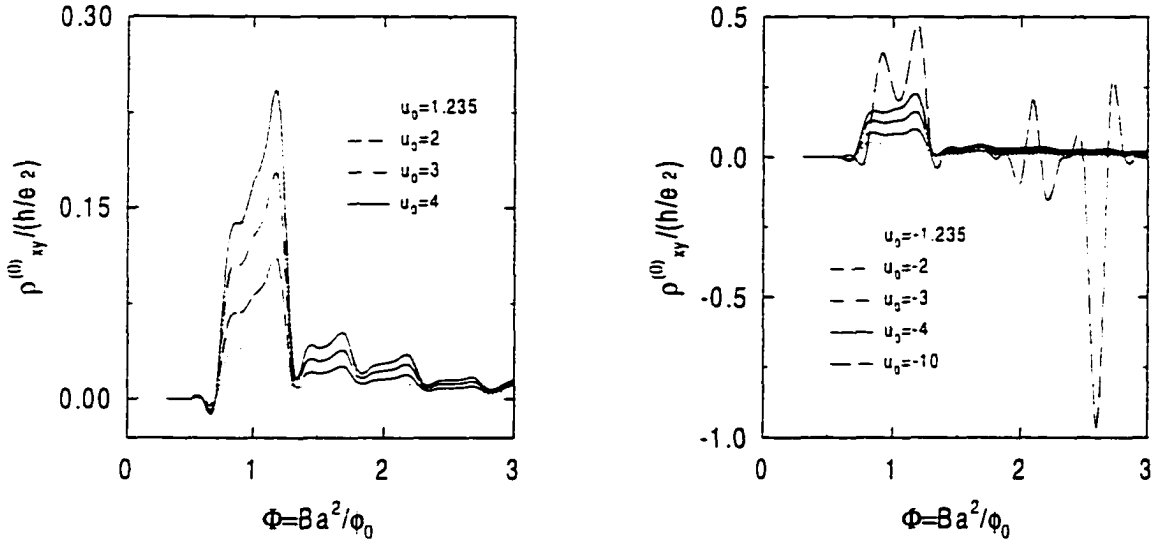

(a) Anti-dot **(b) Quantum-dot**

Figure 35: Hall Resistivities $\rho^{(0)}_{xy}/(h/e^2)$ vs. $\Phi = Ba^2/\phi_0$ (a) Anti-dot for $N = 1$ (b) Quantum-dot for $N = 1$; $N_x = N_y = 4$, $n = 3$, $n_{2D}a^2 = 0.5$, and $a = 200nm$.

Anti-dot regime Fig. 35(a) shows how the Hall resistivities are affected by the variation of U_0 for a anti-dot regime. When U_0 is increased, the electrons are more scattered by the scatterers. So the Hall resistivities are increased when U_0 is increased. All the other features are same as in section 5.4.1. At low magnetic fields, the Hall resistivities are quenched and the oscillatory behaviour due to the DOS are still observed.

Quantum-dot regime Fig. 35(b) shows how the Hall resistivities are affected by the variation of U_0 for a quantum-dot regime. When U_0 is negatively increased, electrons are apt to be confined within dots. So the Hall resistivities are increased with $|U_0|$. When $U_0 = -1.235$ through -4, the amplitudes are increased but not yet plus- to-minus oscillations. For $U_0 = -10$, they have large plus-to-minus oscillations. As in the quantum-dot case in section 5.4.1, these plus-to-minus oscillations are considered as the Aharonov-Bohm oscillations.

6 Numerical Results of QMT Coefficients for 1D Modulation

We now present numerical results for the band parts of all QMT coefficients in the x directional modulation on QW. We used the equations for the 1D modulation defined in section 4.3 to calculate QMT coefficients. Because only the x direction is modulated. x and y are not symmetry. Therefore, we compute all components: Transverse Conductivities (along the modulation direction) $\sigma_{xx}^{(0)}$. Hall Conductivities $\sigma_{yx}^{(0)}$. Longitudinal Conductivities (along the QW channel) $\sigma_{yy}^{(0)}$. Transverse Resistivities (along the modulation direction) $\rho_{xx}^{(0)}$. Hall Resistivities $\rho_{xy}^{(0)}$. and Longitudinal Resistivities (along the QW channel) $\rho_{yy}^{(0)}$. where

$$\rho_{xx}^{(0)}(0) = \frac{\sigma_{yy}^{(0)}(0)}{\sigma_{yy}^{(0)}(0)\sigma_{xx}^{(0)}(0) + [\sigma_{yx}^{(0)}(0)]^2} . \tag{60}$$

$$\rho_{xy}^{(0)}(0) = -\rho_{yx}^{(0)}(0) = \frac{\sigma_{yx}^{(0)}(0)}{\sigma_{yy}^{(0)}(0)\sigma_{xx}^{(0)}(0) + [\sigma_{yx}^{(0)}(0)]^2} , \tag{61}$$

$$\rho_{yy}^{(0)}(0) = \frac{\sigma_{xx}^{(0)}(0)}{\sigma_{yy}^{(0)}(0)\sigma_{xx}^{(0)}(0) + [\sigma_{yx}^{(0)}(0)]^2} , \tag{62}$$

6.1 Transverse Conductivities

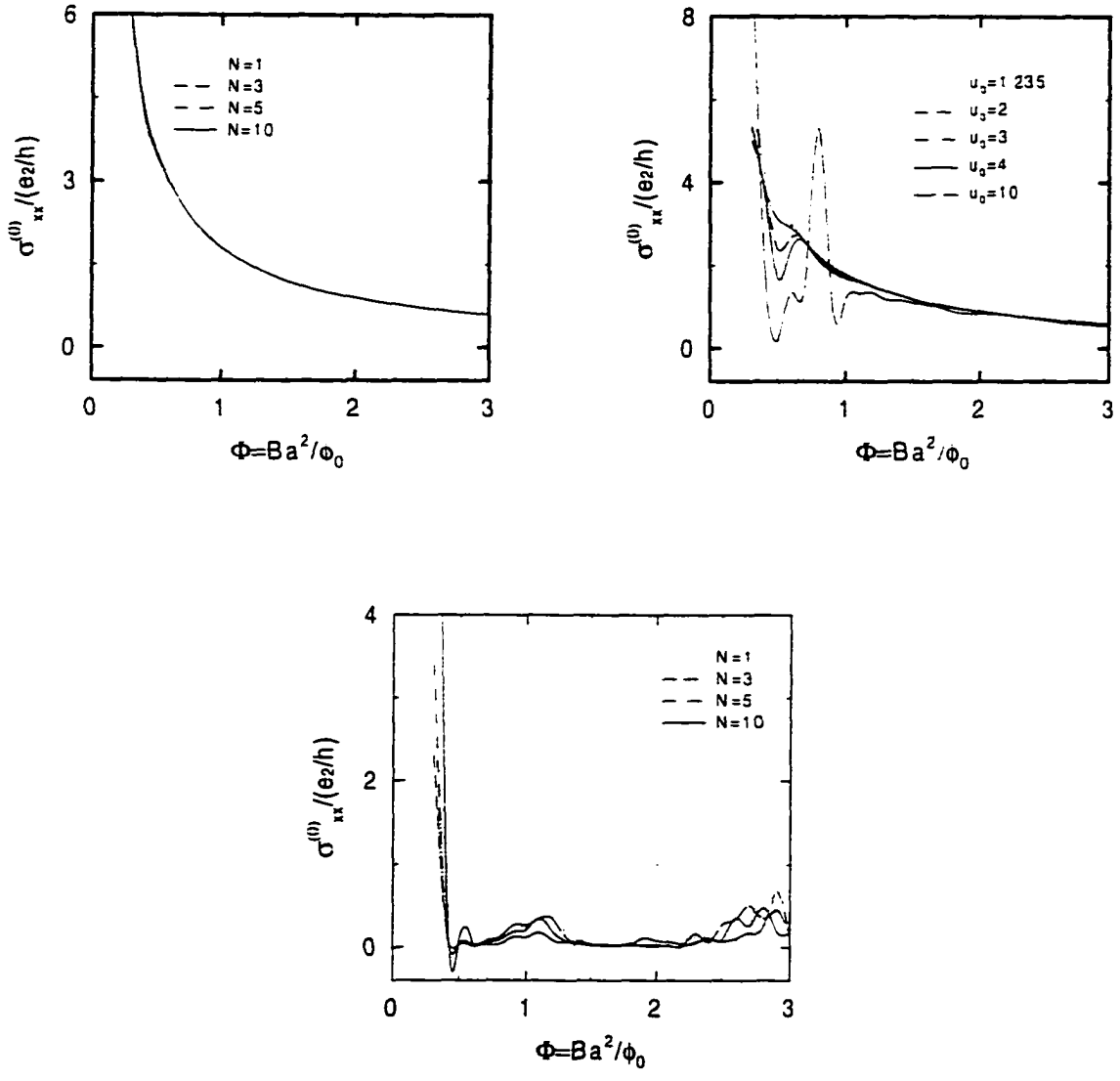

Figure 36: Transverse (along the modulation direction) conductivities $\sigma^{(0)}_{xx}/(e^2/h)$ vs. $\Phi = Ba^2/\phi_0$ for the various potential barriers in the one dimensional modulation. $N_x = N_y = 6$, $n = 10$, $n_{2D}a^2 = 0.5$, and $a = 200nm$. (a) Transverse conductivities with N for the QW potential in Eq. (15) with $U_0 = 1.235$ (b) Transverse conductivities with U_0 for the QW potential in Eq. (15) with $N = 1$. (c) Transverse conductivities with N for the QW potential in Eq. (15) with $U_0 = 100$

Shown in Figure 36 (a), (b), and (c) is the numerical results of transeverse (along the modulation direction) conductivities ($\sigma_{xx}^{(0)}$) in the x-directional modulation for the diverse potential barriers. For the weak modulation case (Fig. 36 (a). $U_0 = 1.235$. $\bar{V}_0 = 0.156$ meV). when Φ is increased. the intensity of $\sigma_{xx}^{(0)}$ is monotonically decreased. And all the features in Fig. 36 (a) are not appreciably changed by the width of the potential barrier (with N). According to the Eq.(A1). $\sigma_{xx}^{(0)}$ is contributed only by the electrons near the Fermi level energy. In our case. $\bar{V}_0 = 0.156$ meV for $U_0 = 1.235$ and a = 200 nm. All the Fermi level energies in whole range of Φ are 0.203 - 2.03 meV which are above the strength of the potential. $\bar{V}_0 = 0.156$ meV. Accordingly. electrons with those Fermi level enegies can have more capabilities of going over the potential barrier. So the electrons in these electronic states are not much affected by the potential barrier and thus more depend on the size of the electronic orbit. When Φ is increased. the size of the orbit is reduced and these electrons less conribute to the conductivities $\sigma_{xx}^{(0)}$. And also. these electrons can't feel the variation of the width of the potential barrier. The reason is that the electrons are in the Fermi level energies which are above the potential barrier. With this reason, all the features in Fig. 36 (a) are not appreciably changed by the width of the potential barrier (with N). This phenomenon is also supported by Fig. 36 (b). In these figures, it is seen how the features are modified with the variation of the strength of the potential $\bar{V}_0$. In Fig. 36 (b), for $a = 200$ nm and $U_0 = 1.235$, 2, 3, 4, 10, $\bar{V}_0 =$

0.156, 0.253, 0.380, 0.506, and 1.265 meV, repectively. On the other hand, the Fermi level energies are 0.203-0.676 for $\Phi < 1$ and 0.823-2.03 for $\Phi > 1$ in the unit of meV, respectively. So, for the range of $\Phi < 1$, the Fermi level energies are comparable with the potential height and thus there are dramatic changes of intensities of $\sigma_{xx}^{(0)}$ in the low magnetic field regions. These changes are due to the potential barrier effect. When the QW barrier height is increased, the kinks become deeper at $\Phi = 0.5$ and another resonant peak is shown at $\Phi = 0.8$ for $U_0 = 10$ case. For $\Phi > 1$ region, the features are same as in Fig. 36 (a). Because the Fermi level energies are above the barrier height. However, all these features are completely modified for the case of $U_0 = 100$ ($\tilde{V}_0 = 12.65meV$) as seen in Fig. 36 (c). In this strong modulation case, the Fermi level energies are far below the QW barrier height. So, in the whole region, the electrons are bounded between the QW barriers and thus they can see the change of the QW width. In the very low magnetic field region, the intensities are increased as N is increased i.e. QW width is decreased and the slope of QWs are steeper. This is the evidence that when the electron scatters with the steeper QW barrier, it more proceeds the forward scattering. And also, there are several differnet resonant peaks in the whole range as N varies.

6.2 Transverse Resistivities

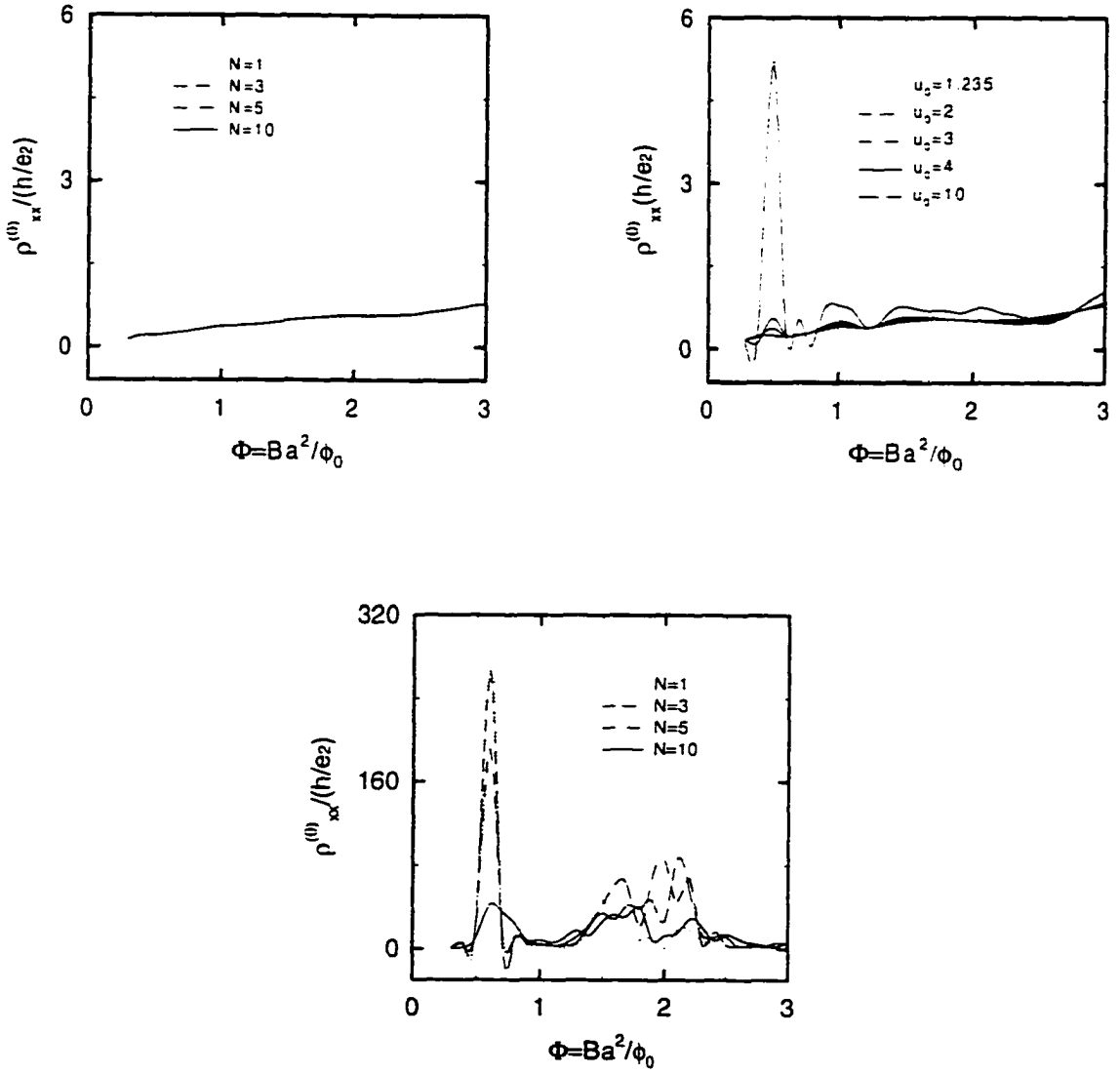

Figure 37: Transeverse resistivities $\rho^{(0)}_{xx}/(h/e^2)$ vs. $\Phi = Ba^2/\phi_0$; $N_x = N_y = 6$, $n = 10$, $n_{2D}a^2 = 0.5$, and $a = 200nm$. (a) Transverse resistivities with N for the QW potential in Eq. (15) with $U_0 = 1.235$ (b) Transverse resistivities with U_0 for the QW potential in Eq. (15) with $N = 1$. (c) Transverse resistivities with N for the QW potential in Eq. (15) with $U_0 = 100$.

The Transverse Resistivities($\rho_{xx}^{(0)}$) are shown in Fig 37 (a), (b), and (c) for diverse QW barrier cases. In Fig 37 (a), the steepness of the potential modulation is varied with the power of cosine potential for the low modulation case ($U_0 = 1.235$, $\bar{V}_0 = 0.156$ meV). All the curves are not sensitive for the change of the steepness of the potential barrier. These can be explained, as in the Transverse Conductivities case, by the fact that Fermi Level energy is higher than the QW barrier height. In the whole range, $\rho_{xx}^{(0)}$ slightly increases as Φ increases. The electron ,in this low modulation case, behaves as if it were in the normal homogeneous 2DEG. In this regime, the smaller orbit contributes to large $\rho_{xx}^{(0)}$. That is why $\rho_{xx}^{(0)}$ increases as Φ increases. This normal behaviour is modified when the QW barrier height is increased. Shown in Fig 37 (b) is the numerical results for the variation of the height of the QW barrier with the power of $N = 1$. When U_0 varies from 1.235 ($\bar{V}_0 = 0.156$ meV) to 10 ($\bar{V}_0 = 1.265$ meV), in the low magenetic field region, the peaks are modified and the peaks at $\Phi = 0.5$ are increased when U_0 is increased. When $U_0 = 10$, the giant magenetoresistance is shown there. These low-field giant magnetoresistances are also shown in the strong modulation case. (Fig 37 (c) This figure is for $U_0 = 100$ ($\bar{V}_0 = 12.65$ meV). In this case, the low-field giant peaks are decreased when N is increased. From these facts, we know that the low-field giant peaks really depends on the height and the width of the QW barrier. Experimentally, it has been, in [70], found that these giant peaks arise from the result of anisotropic k-vector space. In this

reference ([70]). the giant peak is very small and its position is shifted from the origin when the Fermi level enrgy (9.0 meV) is much higher than the height of the QW barrier (6.7 meV). If the Fermi level enrgy (8.1 meV) is compatible with the height of the QW barrier (7.8 meV). then the giant peak becomes very big. In other words. when the Fermi level enrgy is much higher than the height of the QW barrier. x directional momentum (modulation direction) is relatively increased and it increases the conductivities and accordingly. it decreases the resistivities in x-direction. That is why the giant peak becomes very small. Reversely. when the Fermi level enrgy is compatible with the height of the QW barrier. x directional momentum (modulation direction) is relatively decreased and it decreases the conductivities and increases the resistivities in x-direction. It makes the giant peak. So. these anisotropic momenta change the conductivities and these changed conductivities make the anormalous giant peaks because the resistivity tensor ρ is inversely proportional to the conductivity tensor σ. And also the peak position of the giant peak is shifted from the origin in Fig 37 (b) and (c). These are agreed with other experimental results.[70, 64]

6.3 Hall Resistivities

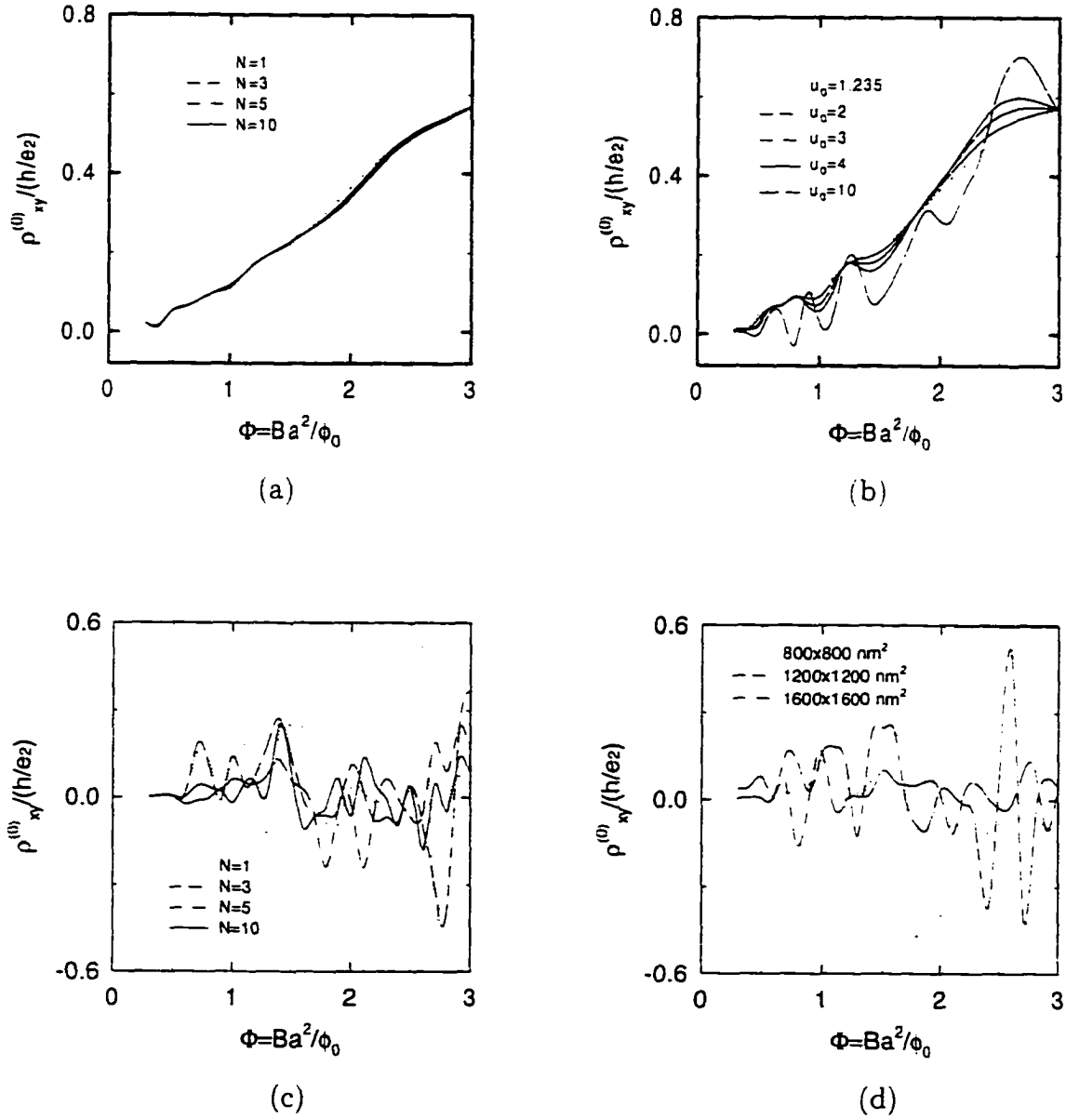

Figure 38: Hall resistivities $\rho^{(0)}_{xy}/(h/e^2)$ vs. $\Phi = Ba^2/\phi_0$ $N_x = N_y = 6$ (for a,b, and c) $n_{2D}a^2 = 0.5$ and $a = 200nm$. (a) Hall resistivities with N for the QW potential in Eq. (15) with $U_0 = 1.235$ (b) Hall resistivities U_0 for the QW potential in Eq. (15) with $N = 1$ (c) Hall resistivities with N for the QW potential in Eq. (15) with $U_0 = 100$. (d) Hall resistivities by sample sizes for the QW potential in Eq. (15) with $N = 1$ and $U_0 = 100$

Fig 38 shows the numerical results of Hall Resistivities $\rho_{xy}^{(0)}$ for the diverse QW barriers as in the case of Transverse Resistivities. In this figure, the Hall Resistivities have a quenching in the low magnetic field region. This quenching of the Hall effect in one-dimensional wire was first observed by Roukes *et al.*.[67] In their paper, quenching was observed for the wire width which is less than 200 nm and at low temperatures and low magnetic fields in which both $k_B T$ and $\hbar\omega_c$ are less than the energy splitting of the states created by transeverse confinement. In our case, we used 200 nm scale of the modulation period. However, our actual QW width is quite less than this scale because our QW barrier is modeled by the cosine potential defined in Eq. (15) with some finite width. And also we calculated at $T = 0$. So all the conditions of being done in ref. [67] are satisfied in our case. One of the possible reasons about this quenching effect, as mentioned in the introduction section, is by the collimated electrons. At low magnetic fields, the open-orbit electrons are resonantly scattered off the QW barrier and those electrons are collimated. These collimated electrons make the ratio of the longitudianal (QW direction) momentum to the transeverse (modulation direction) momentum increase and preferentially transmit through the wire. If this transmitted electrons overcome the Hall voltage, then the Hall voltage is quenched.[68] Fig. 39 well shows this ratio of the longitudinal to the transverse conductivities. Fig. 39 (a) shows the transverse conductivities $\sigma_{xx}^{(0)}/(e^2/h)$ with U_0 (along the modulation direction, in our case x-direction) as a function of the magnetic flux

ratio $\Phi = Ba^2/\phi_0$. At low magnetic fields, the intensities are reduced as U_0 is increased. It means that the transverse momentum is reduced when the QW barrier height is increased. On the other hand, the longitudinal conductivities (along the QW direction, in our case y-direction) $\sigma_{yy}^{(0)}$ is increased at low magnetic fields when U_0 is increased. (Fig. 39 (b))

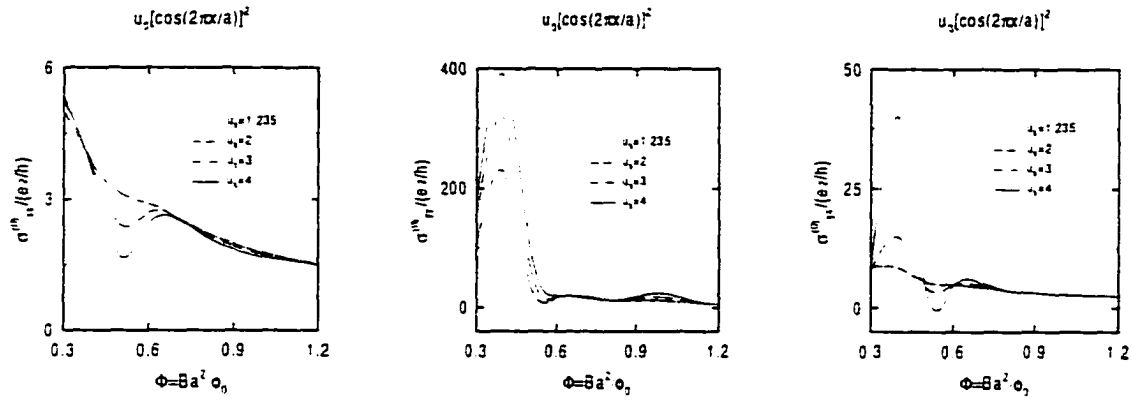

(a) (b) (c)

Figure 39: Various Conductivities as a Function of Φ: $N_x = N_y = 6$. $n = 10$. $n_{2D}a^2 = 0.5$. and $a = 200nm$. (a) Transverse conductivities $\sigma_{xx}^{(0)}/(e^2/h)$ with U_0 for the QW potential in Eq. (15) with $N = 1$. (b) Longitudinal conductivities $\sigma_{yy}^{(0)}/(e^2/h)$ with U_0 for the QW potential in Eq. (15) with $N = 1$. (c) Hall conductivities $\sigma_{yx}^{(0)}/(e^2/h)$ with U_0 for the QW potential in Eq. (15) with $N = 1$.

So, the longitudinal momentum is increased when the QW barrier height is increased. Therefore, the ratio of the transeverse momentum to the longitudinal momentum is increased when the QW barrier height is increased. The corelation between the transverse and the longitudinal momentum is also shown in Hall conductivities $\sigma_{yx}^{(0)}$ in Fig. 39 (c). When U_0 is increased, Hall conductivities are increased at the low magnetic fields. This increased logitudinal momentum

makes the collimated electrons and they scatter off the QW barrier and quench the Hall resistivities when they have enough energy to overcome the Hall voltage. Scattring off the QW barrier is more when the barrier is higher and steeper. So. we can see. in Fig. 40. that the higher and the steeper the QW barrier is. Hall resisitivities are more quenched. This quenching effect in one dimensional QW has been observed in many other papers.([68. 35])

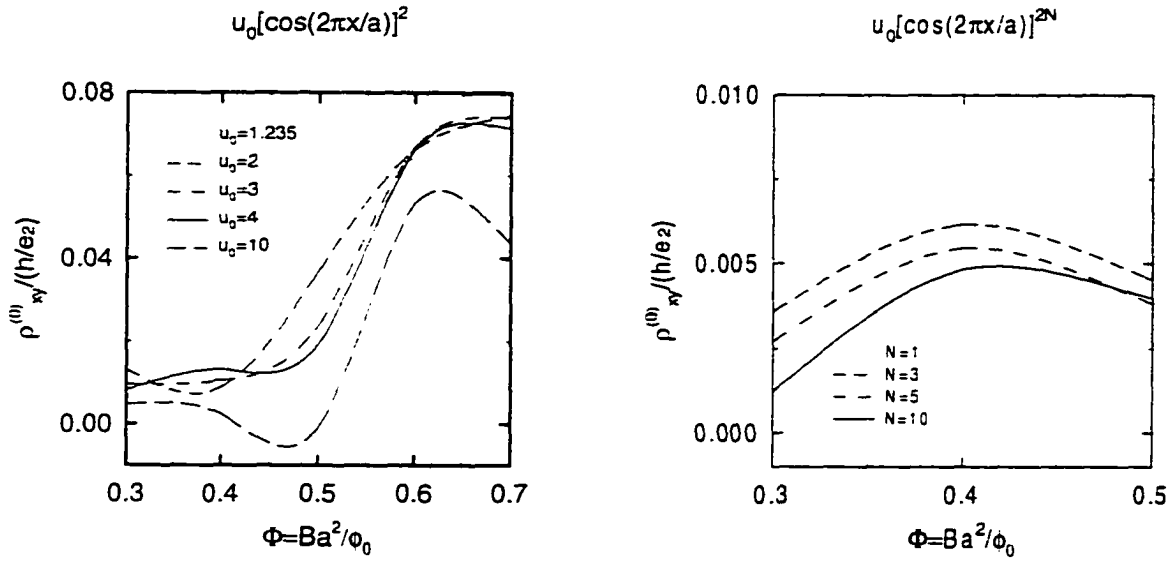

Figure 40: Quenched Hall resistivities $\rho_{xy}^{(0)}/(h/e^2)$ vs. $\Phi = Ba^2/\phi_0$: $N_x = N_y = 6$. $n = 10$. $n_{2D}a^2 = 0.5$, and $a = 200nm$. (a) Quenched Hall resistivities with U_0 for the QW potential in Eq. (15) with $N = 1$. (b) Quenched Hall resistivities with N for the QW potential in Eq. (15) with $U_0 = 100$.

Next, what we can see in Fig 38 (a) is the classical Hall effect. If we take the crystal of semiconductor doped with donors in a magnetic field perpendicular to the sample (z-direction) and in an electric field (x-direction), then the free electrons move in horizontal circular orbits by the Lorenz force and accumulate

on one side of the y-direction. As the electrons accumulate on one side, a negative charge builds up which acts to repel other electrons from entering this region. At some point, a balance is achieved when the repulsive force is equal to the magnetic force pushing the electrons into this region. This voltage difference in y-direction is called Hall voltage. With this explanation, it is straightforward to see how the strength of the magnetic field affects the Hall voltage. If the magnetic field strength is increased, then more electrons can be pushed on to the side on which the electrons accumulate before the balance is reached. Accordingly, the Hall voltage is increased. Conversely, decrease in the magnetic field strength results in a reduction in the Hall voltage. Therefore, the Hall voltage increases in direct proportional to the magnetic field strength. This is classical Hall effect which was first noticed by Edwin Hall in 1879. Fig 38 (a) is the case in which the classical Hall effect can be seen. Because the Fermi level (0.2 - 2 meV) is quite higher than the QW potential barrier (0.156 meV). Almost all of electrons, in this regime, behave as if they were in the normal homogeneous 2DEG. So, in the whole range of Φ, Hall resistivities are linearly increased as Φ is increased. These linear increase of $\rho_{xy}^{(0)}$ in the whole range of Φ is modified by the stronger potential barrier. We can see this effect in Fig 38 (b). The linear Hall effect is appreciably modified when U_0 increases. In this case, the Fermi level energy is cmpatible with the QW barrier height ($0.156 \sim 1.265 meV$). When U_0 is strongly enough (Fig 38 (c)), this linear clssical effect is completly disappeared and anomalous

Hall effect due to the unisotropic scattering with QW wall comes out. In this regime, the striking feature is the negative Hall resistivities. This negative Hall resistivities are guessed as due to the sample boudary back scattering of the short QW. As mentioned in introduction section, if the wire is infinite, then there is no smaple boundary back scattering and only the forward scattering is enhanced in QW direction after scattering with the QW barrier. However, if the wire is finite and short, then there can be a resonant back scattering off the sample boundary after scattering with the wire wall. At low magnetic fields, the forward scattering is enhanced to make quenched Hall effect. But, at high magnetic fields ($1< \Phi <2.7$), the cyclotron orbit is compatible with the width between QW barriers and resonant back scattering from the sample boundary can be experienced. When the width of the QW barrier (i.e.QW is wider) is reduced, the negative Hall resistance is reduced.(Fig 38 (c)) And also, as seen in Fig 38 (d), when the sample is expanded, this negative Hall resistance is reduced. With these results, the negative Hall resistivities are guessed as due to the sample boundary back scattering of the edge states with the compatible cyclotron orbit with the width between QW barriers before it is closed in the short QW. Beyond this point ($\Phi = 2.7$), it behaves as if it is in the normal 2DEG and its Hall resistivities are increased as Φ is increased. This threshold point is seen very well in Fig. 41.

6.4 Longitudinal Resistivities

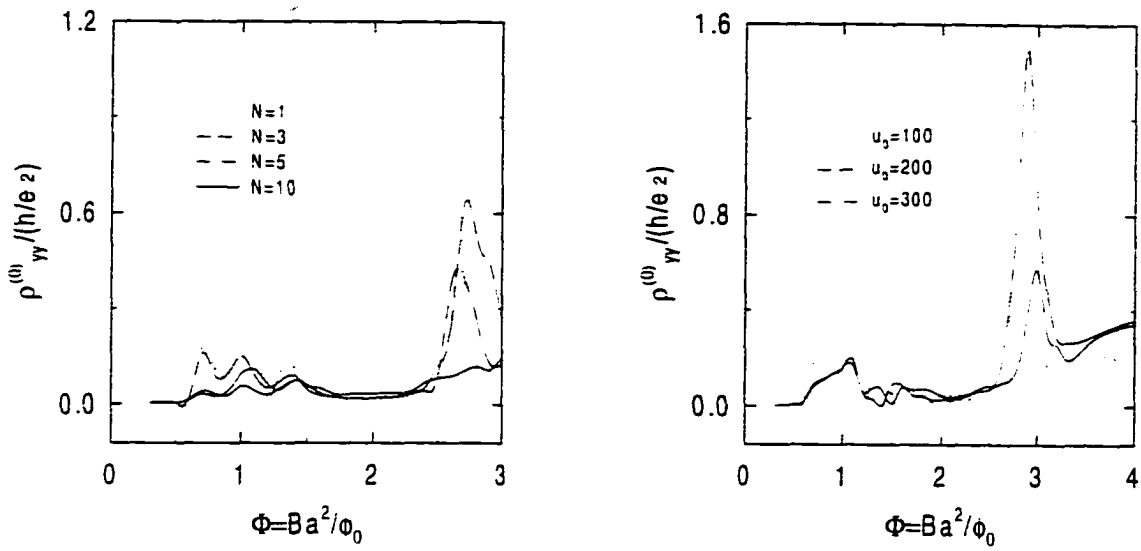

(a) (b)

Figure 41: Longitudinal resistivities $\rho^{(0)}_{yy}/(h/e^2)$ vs. $\Phi = Ba^2/\phi_0$, where $N_x = N_y = 6$ $n_{2D}a^2 = 0.5$ and $a = 200nm$. (a) Longitudinal resistivities with N for the QW potential in Eq. (15) with $U_0 = 100$ (b) Longitudinal resistivities with U_0 for the QW potential in Eq. (15) with $N = 1$

Fig. 41 shows the longitudinal resistivities $\rho^{(0)}_{yy}/(h/e^2)$ as a function of magnetic flux ratio $\Phi = Ba^2/\phi_0$. (along the QW direction) FIg. 41 (a) is the results for the change of the QW width. The threshold point is around at $\Phi = 2.7$. This is the coincident point beyond which the Hall resistivities behave in the normal 2DEG as stated in Hall resistivity section. This threshold point depends on the QW width between barriers. In our case, when N is increased (i.e. QW width between barriers is increased), the threshold point is slightly changed. This comes from the resonant scattering effect by the change of the QW width. In addition to this,

FIg. 41 (b) shows that when U_0 is increased. the threshold peaks are also shifted to the high magnetic fields. So this threshold peaks really depend on the height of the QW barrier as well as the QW width between barriers. This phenomenon very well agrees with other paper.[66]

7 Summary and Conclusions

In this thesis. I used controllable modulation potenital to calculate the eigenstates and QMT coefficients for 2D and 1D modulation and discussed about their numerical results. In 2D eigenstates. I found that the shift of the eigenvalues from LLs is reduced as Φ is increased (i.e. the magnetic field B is increased) because the LL orbit becomes smaller. Secondly when N is increased. the shift from the LLs is reduced because there is more space between the scatterers or dots to freely move. The third one is that the band width of the modulation-broadened LLs oscillates with the magnetic field B or Φ. It reflects that when the cyclotron radius is changed. the electron is periodically scattered by the periodic scatterers. The fourth one is that when the potential strength U_0 is increased. the band width of the braodened LL is increased and there is LL mixing. In 2D dispersion curves. we could see from the δ potential that LLs are split into p subbands and there are q periods in the first Brillouin zone due to the new MBZ. With these eigensystems. we could QMT coefficients using Kubo method. In longitudinal conductivities $\sigma_{xx}^{(0)}$, there are oscillations related to the DOS for the low modulation case. Hall conductivities $\sigma_{yx}^{(0)}$ is contributed by all states below Fermi level energy. So, the intensities are appreciably changed even for the low modulation case. For quantum-dot, $\sigma_{yx}^{(0)}$ has the plus-to-minus oscillations and Aharonov-Bohm oscillations for the strong potential. And also, the negative Hall conductivities were shown which later, made the negative Hall resistivities.

In longitudinal resistivities $\rho_{xx}^{(0)}$. there was a double peak structure at low magnetic fields. This double peak structure depends on the size and the strength of the modulation. In Hall resistivities $\rho_{xy}^{(0)}$. at low magnetic fields. there was a quenching effect due to the collimated electrons of overcoming the Hall voltage. For strong modulation. there was the negative Hall resistivities. These negative resistivities also depend on the size and the strength of the modulation. And also. there were Aharonov-Bohm oscillations for the strong dot case. In 1D modutioan. we could find the step-like features at low magnetic fields due to the LL crossings in $\sigma_{xx}^{(0)}$. In $\sigma_{yx}^{(0)}$. there were Aharonov-Bohm oscillations for the strong modulation case. In transeverse resistivites $\rho_{xx}^{(0)}$. there was a low-field giant peak due to the anisotropic momentum ratio. In Hall resistivites $\rho_{xy}^{(0)}$. the classical Hall effect was shown for the low modulation case. This was modified when U_0 is increased. At low magnetic fields. there was a quenching effect as observed in experiments. The special interest in this thesis is the negative Hall effect for the short QW which depends on the geometry of the sample. In longitudinal resistivities $\rho_{yy}^{(0)}$. there were threshold peaks which also depend on the size and the strength of he modulation. As seen from above facts, in this thesis, I could generate almost all the features found in experiments or in other papers by using the controllable potential. In addition to these, I could further investigate the results which depend on the size and the strength of the modulation. Unfortunately, the impurity scattering effects are not contained in this thesis.

Appendix

A. Matrix Elements for the δ Potential

In this Appendix A. we present the matrix element $B^{mm'}_{n,n'}(X_0)$ defined in Eq. (9) for the δ potential in Eq. (2)

$$U_{\rm L}(\mathbf{r}) = V_0 \sum_{i,j} \delta(\mathbf{r} - \mathbf{R}_{i,j}) \ . \tag{A1}$$

For the potential in Eq. (A1). we have the counterpart of Eq. (13)

$$\begin{aligned} B^{mm'}_{n,n'}(L) = \sum_{l=-N_x/2}^{+N_x/2} \exp\Bigg[-\pi\Phi\Bigg(\left(l - \frac{(L/N_y)+m}{\Phi}\right)^2 \\ + \left(l - \frac{(L/N_y)+m'}{\Phi}\right)^2\Bigg)\Bigg] \\ \times H_n\left[\sqrt{2\pi\Phi}\left(l - \frac{(L/N_y)+m}{\Phi}\right)\right] \\ \times H_{n'}\left[\sqrt{2\pi\Phi}\left(l - \frac{(L/N_y)+m'}{\Phi}\right)\right] \ . \end{aligned} \tag{A2}$$

Here, $L = -N_y/2, \ \ldots \ , \ ((N_y/2)-1)$ are integers, $\overline{v} = m^* V_0/\sqrt{2}\pi\hbar^2$, N_x is the number of unit cells in the x direction, $\overline{x} = x/a$, $\overline{y} = y/a$. The zero determinant of the coefficient matrix in Eq. (12) gives the energy eigenvalues $E_j(L)$.

B. Matrix Elements for the Grid Potential

In this Appendix B. we present the matrix element $B^{mm'}_{n,n'}(X_0)$ defined in Eq. (9) for the grid potential in Eq. (3)

$$U_{\rm L}(\mathbf{r}) = \overline{V}_0 \left[u_{\rm x} \cos\left(\frac{2\pi x}{a}\right) + u_{\rm y} \cos\left(\frac{2\pi y}{a}\right)\right] . \qquad (B1)$$

where $u_{\rm x}$ and $u_{\rm y}$ are dimensionless. For the potential in Eq. (B1). we have the counterpart of Eq. (13)

$$B^{mm'}_{n,n'}(L) = a\, u_{\rm x}\, \delta_{mm'} \int_{-\infty}^{\infty} d\overline{x}\, \exp\left[-\pi\Phi\left(\left((\overline{x} - \frac{(L/N_{\rm y}) + m}{\Phi}\right)^2 + \left((\overline{x} - \frac{(L/N_{\rm y}) + m'}{\Phi}\right)^2\right)\right]$$

$$\times H_n\left[\sqrt{2\pi\Phi}\left((\overline{x} - \frac{(L/N_{\rm y}) + m}{\Phi}\right)\right] H_{n'}\left[\sqrt{2\pi\Phi}\left((\overline{x} - \frac{(L/N_{\rm y}) + m'}{\Phi}\right)\right] \cos(2\pi\overline{x})$$

$$+a\, u_{\rm y}\, \frac{1}{2}\left[\delta_{m,m'+1} + \delta_{m,m'-1}\right]$$

$$\times \int_{-\infty}^{\infty} d\overline{x}\, \exp\left[-\pi\Phi\left(\left((\overline{x} - \frac{(L/N_{\rm y}) + m}{\Phi}\right)^2 + \left((\overline{x} - \frac{(L/N_{\rm y}) + m'}{\Phi}\right)^2\right)\right]$$

$$\times H_n\left[\sqrt{2\pi\Phi}\left((\overline{x} - \frac{(L/N_{\rm y}) + m}{\Phi}\right)\right] H_{n'}\left[\sqrt{2\pi\Phi}\left((\overline{x} - \frac{(L/N_{\rm y}) + m'}{\Phi}\right)\right] , \quad (B2)$$

where $\delta_{mm'}$ is a Kronecker delta and $H_n(x)$ is a Hermite polynomial. The notation used here is the same as defined in the text.

Publications

- T.Park, G. Gumbs, and M. Pepper : *Quantum Magnetotransport Properties of Short Quantum Wires*. Phys. Rev. B **56**. (1997) (*In Press*).

- T.Park, G. Gumbs : *Magnetotransport Calculations for the 1D Modulation of a 2DEG*. Bull. Am. Phys. Soc. bf 42. 429 (1997).

- T.Park, G. Gumbs : *Quantum Magnetotransport in a Modulated 2DEG : Weak Modulation and Anti-dot Limits*, Superlattices and Microstructures **22**. 1 - 19 (1977)

- T.Park, G. Gumbs : *Quantum Magnetotransport in a Modulated 2DEG*. Bull. Am. Phys. Soc. bf 41, 341 (1996).

- T.Park, G. Gumbs : *Size Effects on the Magnetotransport of a 2D Lattice of Antidots*. Bull. Am. Phys. Soc. bf 40, 168 (1995).

- T.Park, G. Gumbs, and D. Huang : *Size Effects on the Magnetotransport of a 2D Lattice of Antidots*, Bull. Am. Phys. Soc. bf 39, 352 (1994).

- D.Yan, T.Park, Fred H. Pollak, A.R. Srivatsa, T.A. Stokeheim, S.C. Kuo, A. Badzian, and R. Messier : *Temperature Dependence of the Raman Spectra of Diamond and Diamond-like Thin Films on Silicon*, Festschrift for Rogerio Leite World Scientific Publishers (1991)

References

[1] L.Esaki. R.Tsu. Superlattice and negative differential conductivity in semiconductors. IBM J. Res. Devel. **14**. 61-65 (1970)

[2] Peter Y. Yu and M. Cardona. Fundamentals of Semiconductors. Springer-Verlag Press. 1996

[3] H.L.Störmer. R.Dingle.A.C.Gossard. W.Wiegmann. R.A. Logan: Electronic properties of modulation-doped GaAs/$Al_xGa_{1-x}As$ Superlattices. in em Physics of Semiconductors 1978. ed. by B.L.H. Wison (Inst. Phys.. Bristol 1979) pp. 557-560

[4] R.Turton. The Quantum Dot. Oxford University Press.1996

[5] D. Weiss. K. von Klitzing. K. Ploog and G. Weimann. Europhys. Lett. **8**. 179 (1989): also in *High Magnetic Fields in Semiconductor Physics II. Vol. 87 of Springer Series in Solid State Sciences.* edited by G. Landwehr (Springer-Verlag. Berlin, 1989) p. 357.

[6] R. R. Gerhardts. D. Weiss and K. von Klitzing. Phys. Rev. Lett. **62**. 1173 (1989):

[7] R. W. Winkler, J. P. Kotthaus, and K. Ploog, Phys. Rev. Lett. **62**, 1177 (1989);

[8] C. G. Smith. M. Pepper. R. Newbury. H. Ahmed. D. G. Hasko. D. C. Peacock. J. E. F. Frost. D. A. Ritchie. G. A. C. Jones. and G. Hill. J. Phys. Condens. Matter **2**. 3405 (1990).

[9] K. Ensslin and P. M. Petroff. Phys. Rev. B **41**. 12 307 (1990).

[10] R. R. Gerhardts. D. Weiss and U. Wulf. Phys. Rev. B **43**. 5192 (1991):

[11] A. V. Vagov Phys. Rev. B **51**. 51 5065 (1995).

[12] A. Lorke. J. P. Kotthaus. and K. Ploog. Phys. Rev. B **44**. 3447 (1991).

[13] C. G. Smith. W. Chen. M. Pepper. H. Ahmed. D. G. Hasko. D. A. Ritchie. J. E. F. Frost. and G. A. C. Jones. J. Vac. Sci. Technol. B **10**. 2904 (1992).

[14] A. Lorke. I. Jejina. and J. Kotthaus. Phys. Rev. B **46**. 12 845 (1992).

[15] G. M. Gusev. Z. D. Kvon. L. V. Litvin. Yu. V. Nastaushev. A. K. Kalagin and A. I. Toropov. J. Phys. Cond. Matter. **4**. L269 (1992): Superlatt. Microstruct. **13**. 263. (1993): **13**. 383. (1993).

[16] G. Berthold. J. Smoliner. V. Rosskopf. E. Gornik. G. Böhm. and G. Weimann. Phys. Rev. B **45**, 11 350 (1992); **47**, 10383 (1993).

[17] R. Schuster, K. Ensslin, D. Wharam, S. Kühn, J. P. Kotthaus, G. Böhm, W. Klein, G. Tränkle, and G. Weimann, Phys. Rev. B **49**, 8510 (1994).

[18] D. Weiss, M. L. Roukes, A. Menschig, P. Grambow, K. von Klitzing and G. Weimann, Phys. Rev. Lett. **66**, 2790 (1991).

[19] R. R. Gerhardts and C. Zhang, Phys. Rev. Lett. **64**. 1473 (1990): Phys. Rev. B **41**. 12 850 (1990).

[20] D. Pfannkuche and R. R. Gerhardts. Phys. Rev. B **46**. 12606 (1992).

[21] P. Vasilopoulos and F. M. Peeters. Phys. Rev. Lett. **63**. 2120 (1989).

[22] F. M. Peeters and P. Vasilopoulos. Phys. Rev. B **47**. 1466 (1993).

[23] D. R. Hofstadter. Phys. Rev. B**14**. 2239 (1976): *Gödel. Escher. Bach: an eternal golden braid* (Basic Books. New York. 1979) p. 142.

[24] G. H. Wannier. Phys. Stat. Sol. **b100**. 163 (1980).

[25] A. Rauh. G. H. Wannier. and G. Obermair. Phys. Stat. Solidi b **63**. 215 (1974): A. Rauh. Phys. Stat. Sol. **b69**. K9 (1975): H. W. Neumann and A. Rauh. Phys. Stat. Solidi b **96**. 233 (1979).

[26] Y. Hasegawa. Y. Hatsugai. M. Kohmoto, and G. Montambaux. Phys. Rev. B **41**. 9174 (1990).

[27] Y. Hatsugai and M. Kohmoto, Phys. Rev. B **42**, 8282 (1990).

[28] O. Kühn, V. Fessatidis, H. L. Cui, P. E. Selbmann, and N. J. M. Horing, Phys. Rev. B **47**, 13019 (1993).

[29] O. Kühn, P. E. Selbmann, V. Fessatidis, and H. L. Cui, J. of Phys.: Condens. Matter **5**, 8225 (1993).

[30] G. Gumbs. D. Miessein. and D. Huang, Phys. Rev. B **52**. 14 755 (1995).

[31] D. Langbein. Phys. Rev. **180**, 633 (1969).

[32] T. Yamashiro, J. Takahara. Y. Takagaki. K. Gamo. S. Namba. S. Takaoka. and K. Murase. Solid State Commun. **79**. 885 (1991).

[33] D. Weiss. K. Richter. A. Menschig. R. Bergmann. H. Schweizer. K. von Klitzing. and G. Weimann. Phys. Rev. Lett. **70**. 4118 (1993).

[34] M. L. Roukes. A. Scherer. S. J. Allen. Jr.. H. G. Graighead. R. M. Ruthen. E. D. Beebe and J. P. Harbison. Phys. Rev. Lett. **59**. 3011 (1987): C. J. B. Ford. S. Washburn. R. Newbury. C. M. Knoedler and J. M. Hong. Phys. Rev. B **43**. 7339 (1991).

[35] A. M. Chang. G. Timp. J. E. Cunningham. P. M. Mankiewich. R. E. Behringer and R. E. Howard, Solid State Commun. **76**. 769 (1988).

[36] G. Kirczenow and E. Castaño. Phys. Rev. B **43**. 7343 (1991).

[37] M. Büttiker. Phys. Rev. B **38**, 12724 (1988);

[38] R. Fleischmann. T. Geisel and R. Ketzmerick, Phys. Rev. Lett. **68**. 1367 (1992).

[39] I. V. Zozulenko, F. A. Maa/o, and E. H. Hauge, Phys. Rev. B **51**, 7058 (1995).

[40] I. V. Zozulenko, F. A. Maaβ, and E. H. Hauge, Phys. Rev. B (submitted).

[41] H. Silberbauer and U. Rössler, Phy. Rev. B **50**. 11 911 (1994).

[42] K. Bollweg. T. Kurth. D. Heitmann. E. Vasiliadou. K. Eberl. and H. Brugger. Phys. Rev. B **50** (1995).

[43] D. Huang and G. Gumbs. Phys. Rev. B **47**. 9597 (1993).

[44] D. Huang and G. Gumbs. Phys. Rev. B **48**. 2835 (1993).

[45] D. Huang. G. Gumbs. and A. H. MacDonald. Phys. Rev. B **48**. 2843 (1993).

[46] G. Gumbs and D. Huang. Superlattices and Microstructures. **14**. (1993).

[47] T. Yamauchi. Phys. Lett. A**191**. 317 (1994).

[48] P.Rotter. M. Suhrke. and U. Rössler (preprint).

[49] R. Schuster. K. Ensslin. J. P. Kotthaus, G. Böhm and W. Klein. (submitted to Phys. Rev. B).

[50] R. Neudert. P. Rotter. U. Rössler, and M. Suhrke (submitted to Phys. Rev. B).

[51] Y. Takagaki and D. K. Ferry, Phys. Rev. B **45**, 8506 (1992).

[52] T. Park and G. Gumbs, Superlattices and Microstructures (1996).

[53] U. Sivan, Y, Imry, and C. Hartzstein, Phys. Rev. B **39**, 1242 (1989).

[54] N.A. Usov. Sov. Phys. JETP **67**, 2565 (1988)

[55] H. Baranger and A. D. Stone. Phys. Rev. B **40**. 8169 (1989).

[56] R. Kubo. J. Phys. Soc. Jpn. **12**. 570 (1957): D. A. Greenwood. Proc. Phys. Soc. London. **71**. 585 (1958).

[57] A. Bastin. C. Lewiner. O. Betbeder-Matibet and P. Nozieres. J. Phys. Chem. Solids **32**. 1811 (1971).

[58] C.Weisbuch and B.Vinter. "Quantum Semiconductor Sructures". 1991 pp.190-199. Academic Press 1991.

[59] H. Heinrich. G. Bauer. and F. Kuchar. " Physics and Technology of Submicron Structures" . pp.108, Springer, Berlin 1988.

[60] C. J. B. Ford et. al. Phys. Rev. Lett. **62** 2724(1989)

[61] C. J. B. Ford et. al. Phys. Rev. B **43** 7339(1988)

[62] C. J. B. Ford et. al. Surf. Sci. 299 (1990) 298-302

[63] G. Kirczenow and E. Castano, Phys. Rev. B **43** 7343 (1991)

[64] J. E. F. Frost, et. al. Phys. rev. B **53** 9602 (1996)

[65] G. Timp et. al. " Physics and Technology of Submicron Structures" , pp.128, Springer, Berlin 1988.

[66] D. Huang and G. Gumbs, Phys. Rev. B **51**, 5558 (1995).

[67] M. L. Roukes et. al., Phys. Rev. Lett. **59**, 3011(1987).

[68] C. J. B. Ford et. al. Phys. Rev. B **38** 8518(1988) Phys. Rev. Lett. **63**. 996(1989)

[69] A. M. Chang, T. Y. Chang and H. U. Baranger.

[70] G. Muller, P. Streda, D. Weiss, K. von Klitzing, and G. Weinman, Phs. Rev. B **50**, 8938(1994)

Biography

Tae-ik Park was born in Seoul, Republic of Korea. He received B.S. degree in Cheonbuk National University(CNU) in 1981. When he was in undergradute school, he received the 5·16 fellowship for 4 years given by the largest fellowship foundation in Korea and when he graduated university, he received the Graduate Awardship given to the best student from Educational Association of Cheonju City. He obtained M.S. degree in Graduate school of CNU with the title of "Study for the Energy of the Adsorbate on Crystal Surfaces" in 1986 under professor Kee-bang Lee in physics department at CNU. Just before coming to U.S.A., he was recommended by the CNU president to the Korean Government Educational Ministry to take the Government test for the oversea study. He passed the examination and received Korean Govenment Fellowship $40.000 for 3 years. After entering the City University of New York Graduate School, he passed the 1st qualifying exam in 1988. After that, he started his Ph.D. thesis with professor Godfrey Gumbs at Hunter College and passed 2nd exam in 1996. And finally, he finished his Ph.D. thesis with the title of " Modulation Potential Effects on the Quantum Magnetotransport in 2 Dimensional Electron Gas" in 1997. In the mean time, he has worked as an adjunt faculty in physics department at Hunter College and received the Teaching Awardship given to the excellent instructor from Hunter College president in 1997.

IMAGE EVALUATION TEST TARGET (QA-3)

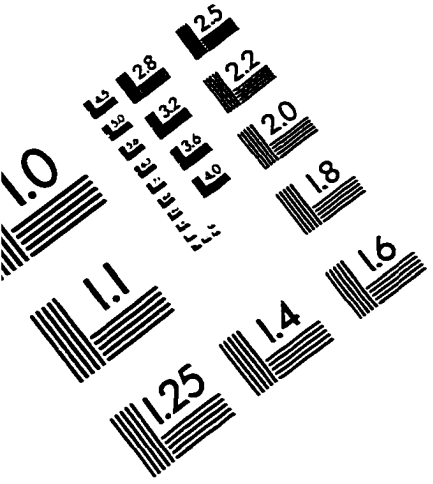

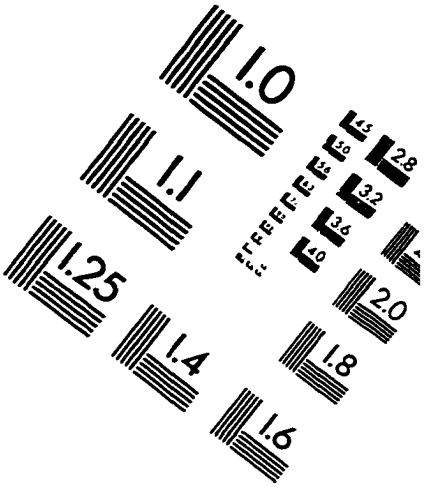

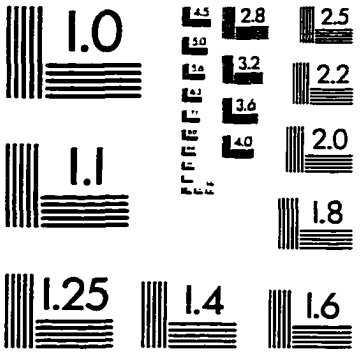

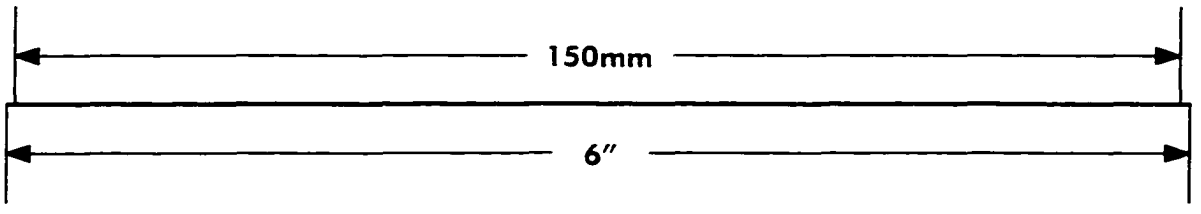

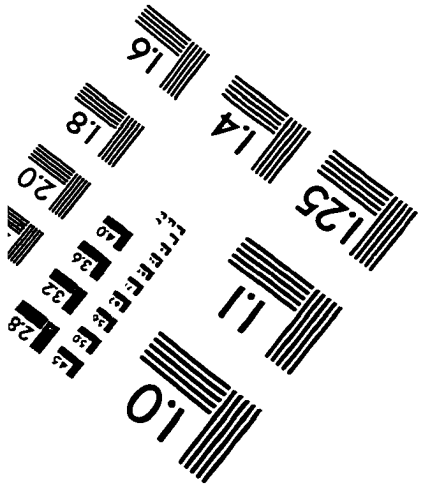

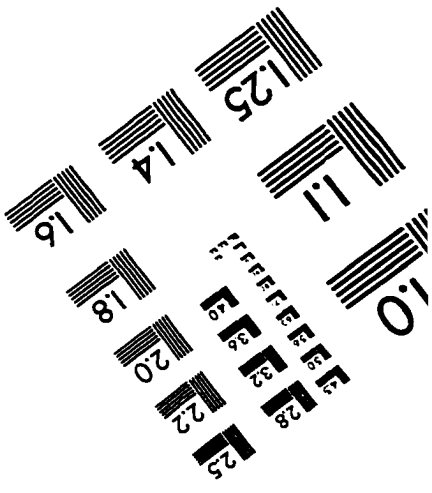

APPLIED IMAGE, Inc
1653 East Main Street
Rochester, NY 14609 USA
Phone: 716/482-0300
Fax: 716/288-5989